PVDF AS A BIOCOMPATIBLE SUBSTRATE FOR MICROFLUIDIC FUEL CELLS

A Thesis Submitted to the

College of Graduate and Postdoctoral Studies

in Partial Fulfillment of the Requirements

for the degree of Master of Science

in the Division of Biomedical Engineering

University of Saskatchewan

Saskatoon

By

Farzad Dehghan

PERMISSION TO USE

In presenting this thesis in partial fulfilment of the requirements for a Postgraduate degree from the University of Saskatchewan, I agree that the Libraries of this University may make it freely available for inspection. I further agree that permission for copying of this thesis in any manner, in whole or in part, for scholarly purposes may be granted by the professor or professors who supervised my thesis work or, in their absence, by the Head of the Department or the Dean of the College in which my thesis work was done. It is understood that any copying or publication or use of this thesis or parts thereof for financial gain shall not be allowed without my written permission. It is also understood that due recognition shall be given to me and to the University of Saskatchewan in any scholarly use which may be made of any material in my thesis.

Requests for permission to copy or to make other use of material in this thesis in whole or part should be addressed to:

Dean

College of Graduate and Postdoctoral Studies

University of Saskatchewan

116 Thorvaldson Building, 110 Science Place

Saskatoon, Saskatchewan S7N 5C9 Canada

OR

Head of the Division of Biomedical Engineering

57 Campus Drive

University of Saskatchewan

Saskatoon, Saskatchewan S7N 5A9 Canada

ABSTRACT

A reliable, flexible, and biocompatible power source for implantable and wearable devices has always been one of the biggest challenges for medical device design engineers. Microfluidic fuel cells (MFCs) are one of the candidates to generate a constant and reliable energy. However, the aspects of this approach, such as use of expensive materials, limitation of achievable power density and biocompatibility, have not yet been fully addressed. These challenges have restricted the application of MFCs to lab-on-chip systems that are deemed to be promising for implantable medical devices.

Recently, porous materials such as natural papers and synthetic polymers (in the form of either nanofibers or porous membranes), when used as the MFC substrate, have shown that they can address the above-mentioned challenges. More importantly, these porous materials induce an inherent capillary flow in the fuel, eliminating the need of a pump. This may lead to an increased fuel efficiency and miniaturization of MFCs. However, the search for a porous biomaterial that displays high mechanical strength but remains flexible without degrading in a biological environment is not straightforward.

In this research, Polyvinylidene Fluoride (PVDF), a non-biodegradable, biocompatible, flexible, and inexpensive material, was investigated for the first time as a channel substrate in a dynamic state MFC. To achieve the desired porosity, flexibility, and material strength of the substrate, PVDF nanofibers were fabricated using the electrospinning technique. Furthermore, hydrophilic PVDF nanofibers were successfully achieved by oxygen plasma surface treatment.

The desired PVDF-based MFC was conceptualized using Axiomatic Design Theory (ADT) and FCBPSS (F: function, C: context, B: behavior, P: principle, SS: structure-state) methods. To investigate the electrochemical output of the designed PVDF-based MFC, a hydrophilic porous PVDF membrane was used as the substrate to induce a capillary action in the fuel (hydrogen peroxide). The PVDF-based MFC studied here successfully produced a power density of 0.158 mW/cm^2 at 0.08 V that is ~60% higher compared to the previous dynamic state paper-based biofuel cell reported in the literature. Moreover, the power density of MFC studied here is comparable to previous studies of static state single compartment MFCs using the same fuel type and

concentration. Therefore, the results from this work demonstrate, for the first time, that the porous PVDF is a suitable material for the channel substrate in a dynamic state MFC.

The potential application of this cell, in medicine, is utilizing the hydrophilic porous PVDF in electrochemical, implantable, and wearable medical devices. This approach can also be applied to any self-powered point-of-care diagnostic system.

ACKNOWLEDGEMENTS

CONTENTS

LIST OF TABLES

LIST OF FIGURES

LIST OF ABBREVIATIONS

ADT   Axiomatic Design Theory

AFC   Alkali Fuel Cell

BioMEMS   Biomicroelectromechanical system

CAD   Computer-aided Design

CR   Constraint

DMA   Dimethylacetamide

DMF   Dimethylformamide

DP   Design Parameters

FBS   Function-Behavior-Structure

FCBPSS   Function-Context-Behavior-Principle-State-Structure

FEBPSS   Function-Effect-Behavior-Principle-State-Structure

FEP   Fluorinated ethylene propylene

FR   Functional Requirement

IC   Integrated Circuit

LOC   Lab-On-Chip

MBR   Membrane bioreactor

MCFC   Molten Carbonate Fuel Cell

MEMS   Microelectromechanical Systems

MF	Micro Filtration
MFC	Microfluidic Fuel Cell
NMP	N-Methyl-2-pyrrolidone
OCP	Open Circuit Potential
PAFC	Phosphoric Acid Fuel Cell
PB	Prussian Blue
PEG	Polyethylene glycol
PEMFC	Proton Exchange Membrane Fuel Cell
PLA	Polylactic Acid
PMMA	Poly (methyl methacrylate)
PTFE	Polytetrafluoroethylene
PVDF	Polyvinylidene fluoride
Redox	Reduction-oxidation
RIE	Reactive Ion Etcher
SD	Systematic Design
SEM	Scanning Electron Microscope
SOFC	Solid Oxide Fuel Cell
UF	Ultra Filtration
UTET	Ultrasonic transcutaneous energy transfer

1   INTRODUCTION

1.1   Background and Motivation

During the past 1-2 decades, energy harvester systems for wearable and implantable devices have been intensively studied. Despite the fascinating advancements in this area, the challenge of providing an inexpensive, flexible, and biocompatible power source has not yet been fully addressed.

Batteries, as a conventional power source, are generally considered impractical and unreliable candidates for wearable and implantable devices because of being bulky, containing hazardous materials [1]. More importantly, the requirement to be replaced periodically adds additional medical expenses and discomfort to patients.

Along with the conventional batteries, researchers have broadly explored wireless power transmission to the implantable device placed inside the patient's body. Transmission of power by resonant frequency electromagnetic fields [2][3] and ultrasonic transcutaneous energy transfer (UTET) systems [4] are a few examples of wireless power transmission techniques. However, wireless power sources bring new challenges, such as higher design complexity and manufacturing cost.

Besides the approaches mentioned above, harvesting energy from the human body has always been attractive for the research studies [5] leading them to introduce a variety of methods such as airflow energy harvesters from the respiratory system [6], thermal energy harvesters [7], kinetic energy harvesters based on the conversion of electromagnetic [8], electrostatic [9], and piezoelectric energy [10]. However, human body energy harvesters have drawbacks such as unreliability, cost, and complexity, that make them unsuitable for commercial use.

Similarly, many studies have focused on fuel cells [11], specifically a miniaturized fuel cell system known as Microfluidic Fuel Cell (MFC) [12]. In MFCs, the fuel delivery and electrochemical reactions are conducted in a microchannel. The microchannel minimizes the quantity of the unreacted fuel by reducing the size of the boundary layer. Simultaneously, the

microchannel characteristic brings a laminar flow feature to the MFC system that avoids a mixture of the fuel and the oxidant. This phenomenon eliminates the requirement of a physical membrane. Therefore, MFCs, compared to conventional fuel cells, may be a highly efficient technology to generate electricity [13]. However, the requirement of an external pump to manipulate the fuel in the microchannel has limited MFCs' efficiency. Furthermore, finding an inexpensive and biocompatible material that can also provide sufficient power for wearable and implantable devices is still under investigation.

In recent years, paper-based MFCs have been introduced as a successful effort to eliminate the external pump in MFCs [14]. Paper materials are flexible, biocompatible, and inexpensive that their porous structure provides a capillary action that eliminates the requirement of an external pump to manipulate the fuel. However, the high biodegradability of paper materials has limited the paper-based MFCs to the lateral flow devices applications [15].

Recently, Polyvinylidene fluoride (PVDF) nanofibers were utilized in a static state single compartment fuel cell. The fuel cell consisted of a cell with dimensions of about 2 mm by 10 mm (M. Jahromi, Private Communication, March 12, 2019) that was covered with the hydrogen peroxide solution as the fuel. PVDF, as the fuel cell substrate, demonstrated a power density of ~ 1 mW/cm^2 at 0.32 V and a current density of ~ 3.2 mA/cm^2 at 0.7 V, which is favorably higher than other biopower generators reported in the literature [16]. However, the study mentioned above has not investigated PVDF in a dynamic state MFC system, where rather than covering electrodes with a fuel solution, the fuel is manipulated in a microchannel by an external pump or capillary action of the channel substrate.

In a nutshell, PVDF is a synthetic, none-degradable, biocompatible, flexible, and inexpensive material that has a promising feature to be used in energy harvester systems for wearable/implantable devices. However, the potential of PVDF in a dynamic state to induce a high capillary action of fuel to eliminate the requirement of an external pump in MFCs has not been investigated yet.

1.2 Research Question

Similar to how the paper-based MFCs successfully eliminates the requirement of a pump, can we develop an MFC using PVDF as its channel substrate to induce capillary flow of fuel so that

an external pump may not be needed? Moreover, if yes, what will be the fuel efficiency of the system to be developed in comparison with the paper-based MFCs?

1.3   Research Objectives and Scope

The overall objective of this research was to develop an MFC system using PVDF as its channel substrate. The following objectives were defined to achieve this overall objective:

Objective 1: qualitatively analyzing the PVDF channel system as an MFC sub-system, to find a suitable channel structure that performs the overall system function.

Objective 2: developing a suitable technique to fabricate a porous PVDF substrate.

Objective 3: analyzing the porous structure and capillary action of the fabricated PVDF substrate out of the research for Objective 2.

Objective 4: testing and characterizing the electrochemical efficiency of a porous PVDF substrate out of the research for Objective 2 in an MFC system.

1.4   Organization of Thesis

In Chapter 2 (Literature Review), a brief introduction of Microelectromechanical Systems (MEMS) and BioMEMS is outlined in Section 2.1. Then, by using the explanation of Microfluidics systems (Section 2.3) and fuel cell systems (Section 2.4), the state of the art of Microfluidic Fuel Cells (MFCs) and their features have been outlined in Section2.5. A review of the recent approaches on fiber-based MFCs is presented in Section 2.6 to illustrate the research gap in PVDF-based MFC. A critical review of PVDF and PVDF nanofibers' features, applications and methods of fabrications are explained in Section 2.7 and Section 2.8. Electrospinning, as a powerful method of fabrication for nanofibers along with PVDF surface hydrophilic modification methods are reviewed in Section 2.9 and Section 2.10, respectively. Finally, FCBPSS framework, Systematic Design Theory (SD), and Axiomatic Design Theory (ADT), which are three powerful tools in advanced conceptual design, are described in Section 2.11, Section 2.12, and Section 2.12.

In Chapter 3 (Design), the following contents are presented. FCBPSS framework was used to find the most suitable channel structure for PVDF-based MFC system, and ADT was utilized to verify the selected structure. Also detailed design of PVDF-based MFC was illustrated.

3

In Chapter 4 (Fabrication), the steps to design and fabricate an electrospinning machine from scratch are explained in Section 4.1. Also, the fabrication steps for the PVDF-based MFC system are described in Section 4.3.

Chapter 5 (Experiment) will discuss the experimental parameters used to fabricate PVDF nanofibers (Section 4.2) along with the fibers inspection method (Section 5.1). The PVDF nanofibers surface treatment method and parameters are explained in Section 5.2. Finally, the experimental steps taken to test the PVDF-based MFC are described in Section 5.3.

Chapter 6 (Results and Discussion) presents the research results. Specifically, Section 6.1 presents the SEM images and fibers characterization for different electrospinning parameters. Section 6.2 presents hydrophilicity and hydrophobicity characterization of PVDF nanofibers before and after surface plasma treatment. Finally, Section 6.3 reports the power and current outputs of the PVDF-based MFC.

This thesis concludes with Chapter 7 and discusses the future works.

2   LITERATURE REVIEW

2.1   Microelectromechanical Systems (MEMS)

Since 1960s, the advent of the Integrated Circuit (IC) has provided a growing and rapid interest in the miniaturization of electronic devices [17]. The achievement in miniaturization of ICs has encouraged the Microelectromechanical Systems (MEMS) technology to make use of the same microfabrication methods to reduce the power, cost, and size (from millimeter to below 100 nanometer) of these complex systems along with improving their functional performance [18].

MEMS components include, but not limited to, cantilevers, sensors, channels, micropumps, rotors, and valves. MEMS technology has been of significant interest, among researchers, owing to features such as quick response time, small size scale, and high volume per area ratio. Despite the vast MEMS employment in in-vitro diagnostic systems, the biocompatibility issues of materials in MEMS technology have limited their scope for in-vivo applications in commercial biomedical devices [18].

2.2   BioMEMS

Biomicroelectromechanical systems (BioMEMS) are a class of MEMS focusing on biomedical applications such as drug delivery, in-vivo sensing, tissue scaffolding, minimally invasive medical procedures, implantable devices, Lab-On-Chip (LOC) devices, etc. [19]. Despite progress in the biocompatibility of BioMEMS, there are many technical challenges yet to be addressed. Microchannel clogging, contamination, fluids mixing, and degradation of implanted micro-devices are some examples of these challenges. Along with biocompatibility and biofouling aspects, in order to practically use BioMEMS in implantable devices, other factors such as the range of communication, environment, size, cost, and required power source need to be addressed [20]. One of the new power sources with the potential to be used in BioMEMS implantable devices is Microfluidic Fuel Cell (MFC). In the following sections (Section 2.3 and Section 2.4), before discussing the state-of-art of MFCs, microfluidics, and fuel cell systems are separately discussed.

2.3 Microfluidics

Microfluidic systems utilize microliters of fluid which flow in one or more micro-sized (at least one dimension is less than 100μm) channels. This micro-level dimension in microfluidics provides the capability to analyze a minimal amount of a sample with high resolution and high sensitivity in a short span of time at a low cost. In addition to microfluidics' micro-size characterization, the laminar flow feature in a microchannel provides the ability to control the flow in space and time [21]. Laminar flow is characterized by the widely used dimensionless Reynolds Number (Re) equation:

$$Re = \frac{\vartheta . l . \rho}{\mu} \tag{2-1}$$

In Equation 2-1, ϑ is fluid velocity, l is channel diameter, ρ is fluid density, and μ is fluid viscosity. In fluid mechanics, conventionally, $Re < 2320$ is considered as laminar flow and $Re > 2320$ is considered as transition state between laminar flow and turbulent flow [22]. In a microfluidic system, due to the micro-sized channel diameter (l in Equation 2-1), the Re number is much less than 2000. Hence, all fluids, irrespective of their fluid-flow parameters, experience laminar flow in a microfluidic system [23].

2.4 Fuel Cell Systems

Fuel cells generate electricity by a reduction-oxidation (redox) reaction that directly converts chemical energy to electrical energy. This one-step process is more efficient than what multi-step combustion engines do [24]. In addition to high efficiency, fuel cells have unique features such as absence of harmful emissions, high power density, environmental friendliness, fuel flexibility and reduced noise and vibration [25]. A simple fuel cell consists of four main parts: anode electrode (where the fuel is oxidized and emits electrons), cathode electrode (where the oxidant is reduced and receives electrons), electrolyte (where ions transfer from anode to cathode), and the fuel cross over avoidance or membrane. Additionally, catalyst materials on anode and cathode electrodes are necessary to facilitate the redox reactions.

Fuel cells are categorized into five different types based on their operating temperature and electrolyte type: 1. Alkali Fuel Cell (AFC), 2. Phosphoric Acid Fuel Cell (PAFC), 3. Molten Carbonate Fuel Cell (MCFC), 4. Solid Oxide Fuel Cell (SOFC), and 5. Proton Exchange Membrane Fuel Cell (PEMFC)[26]. Among these five types of fuel cells, PEMFC (also known as

Polymer Electrolyte Membrane Fuel Cell) has the lowest operating temperature range that is suitable for portable devices.

2.4.1 Proton Exchange Membrane Fuel Cell (PEMFC)

PEMFC is a type of low operating temperature fuel cell utilizing a polymeric barrier (known as membrane) to separate the anode and cathode sections. Figure 2-1 illustrates a schematic of a PEMFC operating with hydrogen gas as fuel and oxygen gas as oxidant.

$$H_2 \xrightarrow{Oxidation} 2H^+ + 2e^-$$

$$O_2 + 4H^+ + 4e^- \xrightarrow{Reduction} 2H_2O$$
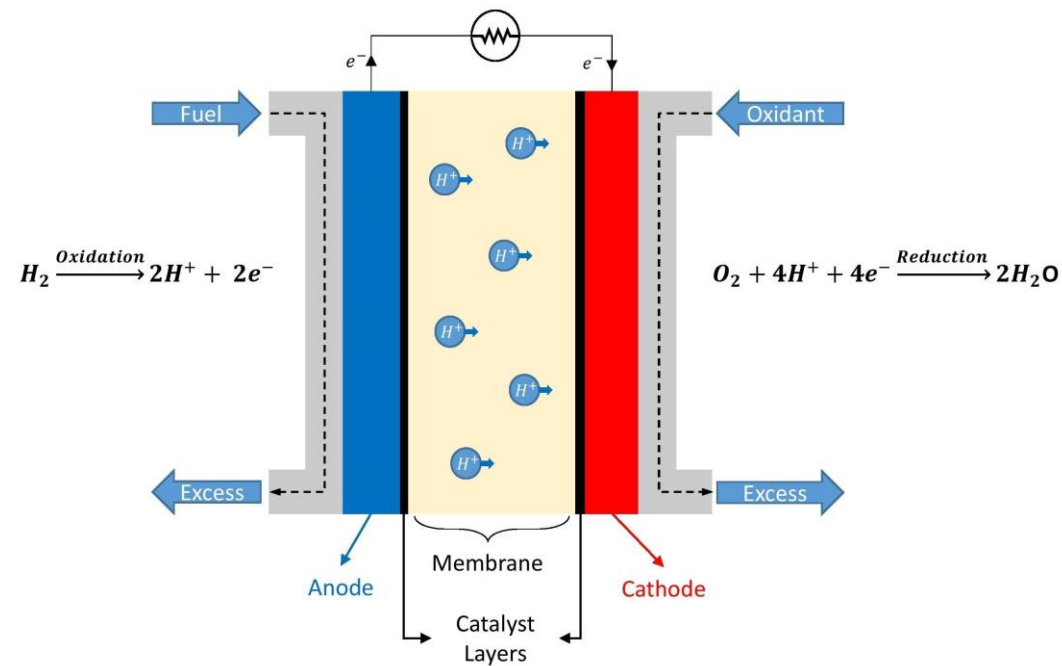
Figure 2-1: Schematic of a PEMFC.

The membrane performs three main roles in PEMFCs; the porous structure of the polymer avoids crossover of electrolyte, provides an electronic insulation to stop electrons from passing through the membrane and finally facilitate the transportation of protons (H^+ ions) [27].

Despite the recent advances in membrane technology [28], there are still technical and economic challenges regarding PEMFCs; e.g. to keep proton exchange efficiency, humidification is required to avoid membrane dry out. In addition to humidification challenge, membrane degradation, maintaining the operating temperature, high fabrication cost and crossover of fuel through membrane are other major problems associated with this type of fuel cell [27]. The challenges hold back PEMFC to be used commercially as a power source for wearable and implantable devices.

2.5   **Microfluidic Fuel Cell (MFC)**

An MFC (also known as membraneless fuel cell or laminar flow-based fuel cell) is a miniaturized fuel cell in which the redox reaction is confined within a microchannel where the fuel and the oxidant flow side-by-side and the electrodes are positioned on opposite sides of the channel. Since the introduction of MFCs in 2002 [29], MFCs have been investigated with different types of fuels such as: hydrogen gas, methanol, formic acid, hydrogen peroxide, vanadium redox species and glucose. MFCs can be categorized based on their channel shapes. Majority of the MFCs have employed a T-shaped or a Y-shaped channel, however, other shapes such as F, O, H and I have also been employed [30]. Figure 2-2 demonstrates the schematics of a Y-shaped MFC. The laminar flow feature of microfluidic systems facilitates the flow of both the fuel and the oxidant through the channel with an inter facial mixing area at the center. This configuration is known as the co-laminar feature of MFCs [30]. Since mixing of the streams is limited to transverse diffusion in the inter facial width and laminar flow feature does not allow crossover of fuel, no physical membrane is required to separate the two solutions leading to elimination of the problems generally associated with PEMFCs mentioned in Section 2.4.1.
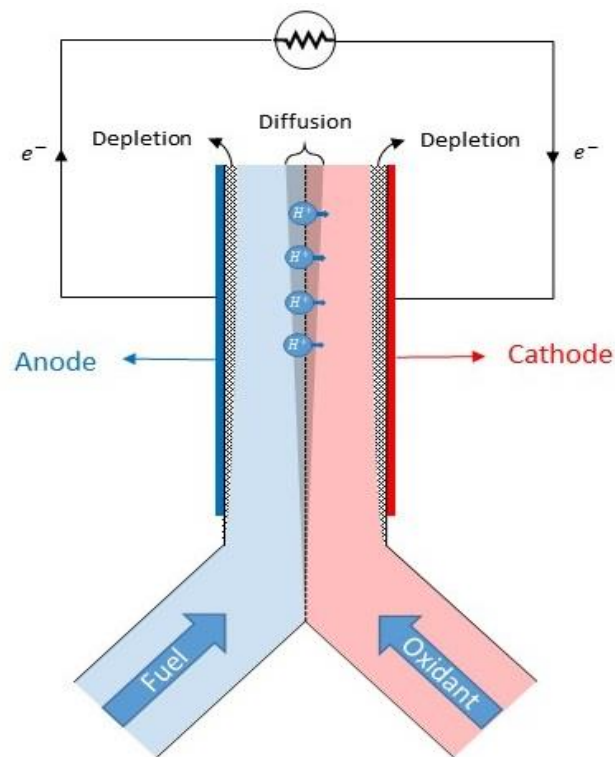
Figure 2-2: Schematic of a Y-shaped MFC and demonstration of co-laminar flow.

The co-laminar flow feature provides a great opportunity to select the fuel and the oxidant, independently, regardless of their electrolyte type. In addition to elimination of membrane, the high surface per volume ratio (due to miniaturization) improves power generation [31].

Despite the advantages, one issue with MFCs is the requirement of a pump to control and maintain the co-laminar flow of the oxidant and the fuel. During operation, the pump is powered by the MFC leading to a great efficiency decrement [32]. Additionally, design and fabrication of pumps increase the cost and size of the MFC.

Since the invention of MFC in 2002, for a period of twelve years, many studies had been conducted on MFCs, however; the requirement of an external pump had been a drawback for this novel system. Finally, in 2014, J.P. Esquivel et al. demonstrated the first paper-based MFC using capillary flow feature in an attempt to eliminate external pump from MFCs [14].

2.6 Fiber-based MFC

Fiber-based materials for wearable or implantable purposes are categorized into two groups: semi natural/synthetic materials (e.g. papers), and biocompatible synthetic materials (e.g. synthetic polymers) [33].

2.6.1 Paper-based MFC

In the recent years, several MFC-based studies have demonstrated more interest in fiber-based materials than conventional ones such as glass or silicon because of their unique features like: high porosity, flexible structure, material strength, low price, biodegradability, biocompatibility and elimination of external pump by inducing a capillary flow.

In 2013, J.P. Esquivel and his co-workers demonstrated the first paper-based MFC with Whatman filter paper as channel, methanol (CH_3OH) as fuel in anolyte and potassium hydroxide (KOH) as oxidant in catholyte (see Figure 2-3) [34][14]. The highly porous structure of paper induces a capillary flow. The combination of this capillary flow and the microfluidics features of the device guarantee a co-laminar flow eliminating the need of external pumps. The highest power density achieved by Esquivel's MFC was 3.2 mW/cm^2 at a current density of 15.5 mA/cm^2 with methanol concentration of 4.0 M [14].
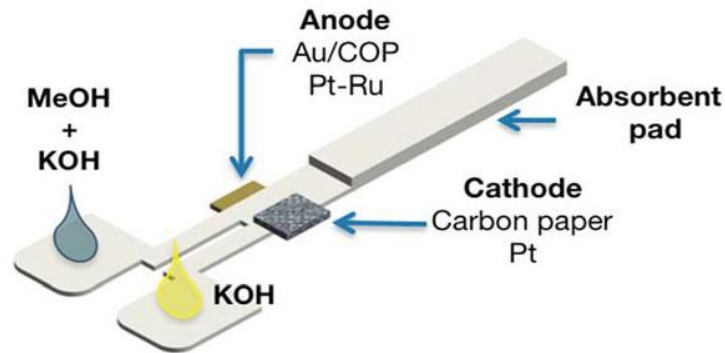
Figure 2-3: The first paper-based MFC (Reproduced from Ref. [14] *with permission from the Royal Society of Chemistry).*

Similar studies have also been conducted: in 2017, Maria Jos´e Gonza´lez-Guerrero et al. used Whatman paper as channel in an I-shaped enzymatic biofuel cell with an induced capillary flow of glucose solution (as fuel) to achieve the power density range of 20 to 90 μW/cm^2 with a glucose concentration of 2.5 to 30 mM [35]. Other similar approaches with a paper-based channel have been conducted by R. K. Arun et al. [36] and X. Yan et al. [37]. However, since the presented MFCs were designed for lab-on-chip purposes, they did not consider the biocompatibility of the channel. Additionally, paper-based materials are highly biodegradable materials decomposing in patients' bodies. This makes the paper-based materials an unsuitable channel candidate for generating power for implantable/wearable devices.

2.6.2 Synthetic Polymer-Based MFC

In 2017, M. Asadnia, et al. introduced an MFC using PVDF as channel substrate for the first time [16]. They evaluated the system with different combinations and concentrations of: hydrogen peroxide as fuel, aluminum or nickel as anode catalyst and Prussian Blue (PB) as cathode catalyst. For the cell operating on 1 M hydrogen peroxide, the highest power densities achieved by Al and Ni were 1 mW/cm^2 and 0.33 mW/cm^2 at the cell potentials of 0.32 V and 0.2 V, respectively. The schematic of the aforementioned MFC is demonstrated in Figure 2-4.

10
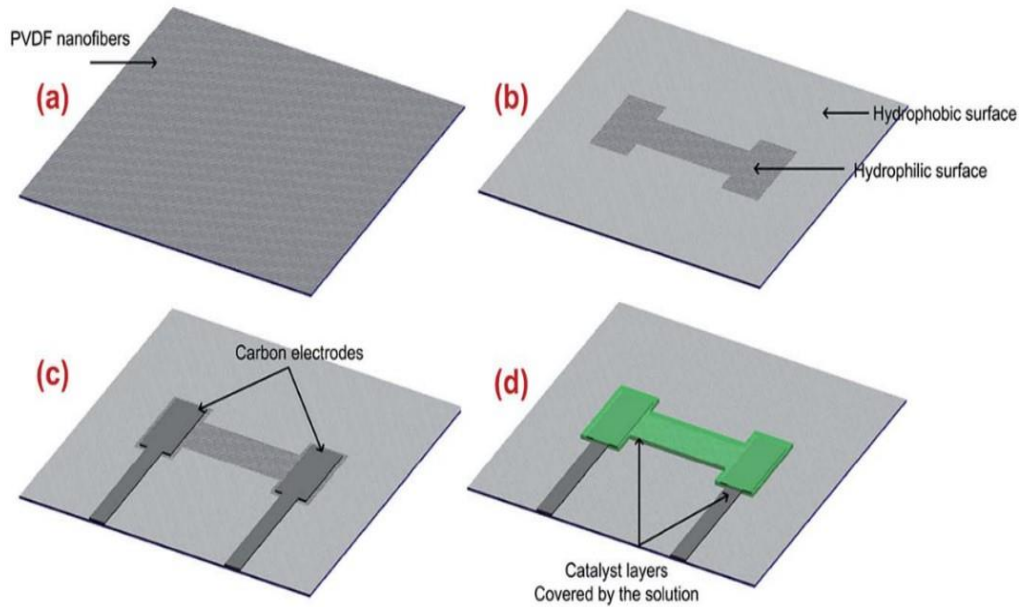
Figure 2-4: Schematic of a PVDF-based MFC. (a) PVDF nanofibers. (b) Patterning of the cell by surface treatment. (c) Installing the carbon electrodes and catalyst layers (Al/Ni and Prussian Blue). (d) Test the cell with hydrogen peroxide solution (Reproduced from Ref. [16] with permission from the Royal Society of Chemistry).

The power density achieved by this single compartment MFC is favorable over other bio purpose MFCs reported in literature [16]; however, since this PVDF-based MFC was designed and investigated in a static state, the unique features of the fiber-based MFC, that is co-laminar flow induced by capillary forces, were not investigated.

2.7 **PVDF**

Polyvinylidene Fluoride or Polyvinylidene difluoride (PVDF) is a synthetic semi-crystalline polymer made by polymerization of $-(CH_2CF_2)_n-$. The monomer of PVDF (vinylidene fluoride) is obtained by dehydrochlorination of chlorodifluoromethane (i.e. removing the hydrogen chloride [H-Cl] from CH_3-CClF_2 [known in industry as refrigerant gas Freon 142b])[38] [39].

2.7.1 **Crystal Structure and Methods of Processing**

PVDF has the ability to take on many forms that can be characterized by the arrangement of $-CH_2-$ and $-CF_2-$ in the carbon backbone of PVDF chain [40]. So far, five different forms or phases of PVDF have been obtained and investigated experimentally:

1. α phase (form II) [41],

2. β phase (form I) [42],

3. γ phase (form III) [43],

4. δ phase [44],

5. ϵ phase [45].

Among the five crystal forms of PVDF, α, β, and γ-PVDF phases are intensively investigated in the literature while α-PVDF phase is the most used polymorph of PVDF. A detailed atomic configurations of α-PVDF phase, β-PVDF phase and γ-PVDF phase (i.e. TGTG', TTTT and T_3GT_3G' respectively) are illustrated in Figure 2-5.

a) PVDF monomer
(Vinylidene fluoride)

b) α-PVDF phase
(TGTG' Configuration)

c) β-PVDF phase
(TTTT Configuration)

d) γ-PVDF phase
(TTTGTTTG' Configuration)
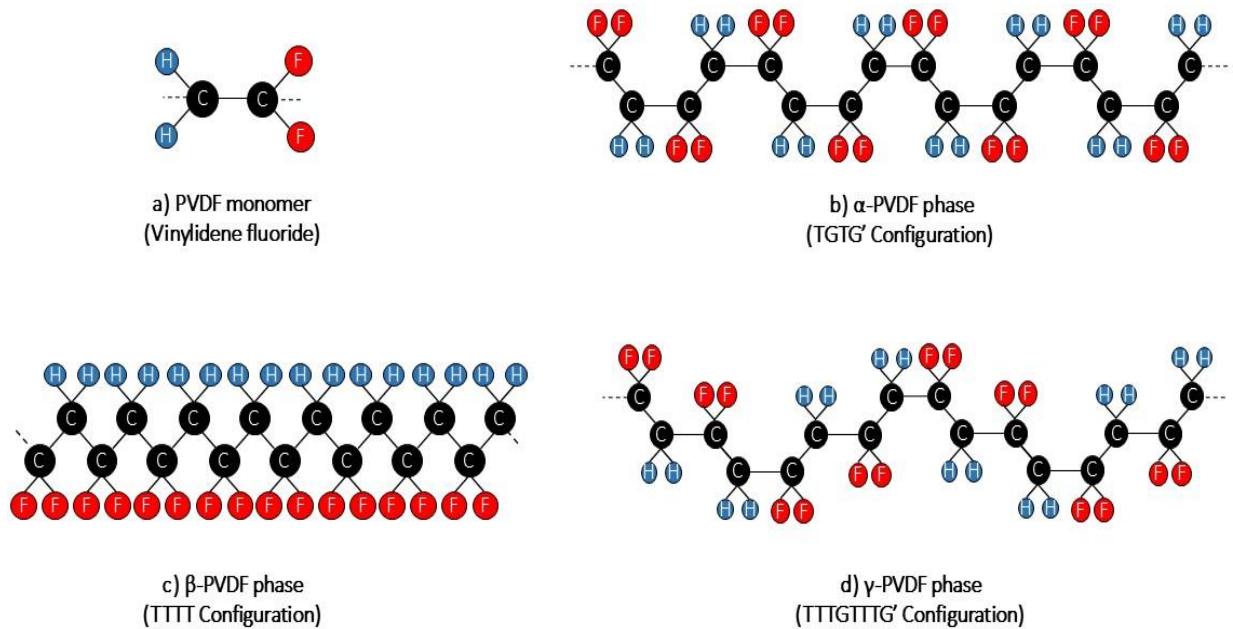
Figure 2-5: PVDF crystal phases. a) PVDF monomer (Vinylidene fluoride). b) α-PVDF phase (TGTG' configuration). c) β-PVDF phase (TTTT configuration). d) γ-PVDF phase (TTTGTTTG' configuration) (adapted from [46]*).*

The chain configurations, polarity and processing methods of these five phases are summarized in Table 2-1.

Regarding manufacturing feasibility, the exceptional chemical and physical properties of PVDF and the availability of various manufacturing procedures for thermoplastic polymers, have made the PVDF to have the lowest cost among the melt-processable fluoropolymers [38].

Table 2-1: PVDF phases and processing methods [47-52].

Phase	Configuration*	Polarity	Methods of Processing
α	TGTG' Monoclinic	non-polar	crystallized readily from the melt in temperatures below 160°C
β	TTTT Orthorhombic	polar	From the α phase: - mechanical drawing at temperatures between 70°C and 100°C - crystallization from dimethylformamide (DMF) or dimethylacetamide (DMA) solutions at temperatures below 70°C. - annealing treatment at high pressure - electrical poling - copolymerization with TrFE i.e. CHF-CF2 from the δ phase: - applying an electric field of 500 MV/m
γ	TTTGTTTG' (T$_3$GT$_3$G') monoclinic	polar	- high-temperature drawing of ultrahigh molecular weight PVDF - annealing α phase samples between 175°C and 185°C
δ	TG'TG	polar	applying an electric field of 100-150 MV/m at α phase leading to flipping the hydrogen and fluorine atoms with respect to the carbon backbone
ϵ	TTTGTTTG'	non-polar	high temperature annealing of δ phase

* T: trans, G: gauche$^+$, G': gauche$^-$

2.7.2 Chemical and Physical Properties

PVDF is well-known for its high purity as well as high chemical resistance to chlorine, oxidants, organic compounds, solvents, corrosive materials (acids and bases), and heat [53].

Due to its crystalline feature, PVDF exhibits excellent physical properties such as high mechanical strength (tensile strength of about 50 MPa), high toughness and stiffness, high stretch ratio (elongation of 250%) while the amorphous phase of PVDF provides flexibility feature [54][55].

In addition to the aforementioned physical and chemical properties, PVDF has a low water absorption (0.02%), low-flammability, low thermal conductivity (about 0.19 W/m-K), high

hydrophobicity, and low melting point of about 150°C which is the lowest melting point among the other commercial fluoropolymers such as Fluorinated ethylene propylene (FEP) and Polytetrafluoroethylene (PTFE or Teflon)[55][38]. In spite of its low melting point, PVDF maintains its high stiffness in temperatures below 150°C while it still offers excellent chemical resistance in harsh environments [38].

In terms of compactness, PVDF has density of 1.78 g/cm^3 that is about 20% less dense than PTFE (Teflon). PVDF is also soluble in common organic solvents such as Dimethylacetamide (DMA), Dimethylformamide (DMF) and N-Methyl-2-pyrrolidone (NMP) [54].

2.7.3 **Electrical Properties**

As shown in Figure 2-5, in α-PVDF configuration, the fluorine and hydrogen dipoles are parallel but oriented in opposite directions (anti-parallel orientation). This anti-parallel orientation of dipoles in the unit cell of α-PVDF provides a neutral electroactivity for this phase. On the other hand, in the β-PVDF and γ-PVDF phases, the dipoles orientation has a non-zero dipole moment providing a polar nature to these two phases. β-PVDF, because of the highest dipole moment in comparison with other PVDF phases has the highest electroactivity [46]. Therefore β-PVDF is mostly well known for its high piezo-electric, ferro-electric and pyro-electric properties [47].

2.7.4 **Applications**

Thanks to its chemical resistance and anti-corrosive properties, PVDF is widely used in a variety of industries. Military aircraft, automotive, and petrochemical industries are some examples where PVDF is utilized specifically for seals, gaskets, and lining purposes. Moreover, due to its low thermal conductivity, PVDF is extensively used in electrical and electronic devices for the purpose of insulation/jacketing of wires and cables, high temperature wiring and industrial power control systems. In a larger scale, because of low cost, flexibility and high purity, PVDF is a popular polymer in chemical processing equipment industries such as chemical pipes, automotive fuel lines and high purity water systems [56].

Due to its high purity, super hydrophobicity, thermal stability, and chemical resistivity, PVDF is also used in membrane and filtration technology in areas such as: water treatment, micro filtration (MF), ultra-filtration (UF), membrane bioreactor (MBR), distillation, gas separation, recovery of biofuels, support for preparing composite membranes, separator for lithium ion

battery, etc. [57].In addition to offering the highest piezoelectric coefficient among the commercial polymers, as it is described in Subsection 2.7.3, low density, workability and mechanical flexibility have made PVDF the principal polymers of interest in sonar hydrophones, ultrasonic transducers, audio-frequency transducers, pyroelectric sensors, and electromechanical devices. Furthermore, because of having an acoustic impedance close to water, PVDF is a favorable material to be used in underwater pressure sensors [38]. MEMS industry also utilizes PVDF piezoelectric properties for energy harvesting purposes [58][59].Finally, because of its high biocompatibility, bioneutrality, non-degradability, odorless, and non-toxic properties, PVDF has found its place in biomedical and pharmaceutical industries and is being used in areas such as: medical textiles and tissue engineering (in form of mono-filaments, hollow fibers, melt-blown non-woven and nanofibers scaffolds) [40][60][61], surgical sutures, surgical meshes [62], drug delivery [63], implantable devices [64] and BioMEMS [65]. PVDF can be produced as a flat sheet, tubular, hollow fiber, and nanofibers [66].

2.8 PVDF Nanofibers

2.8.1 Properties and Applications

Polymer materials synthesized in the form of fibers are characterized by their fiber diameters. By shrinking the polymer fiber diameter below micro-scale or in the range of nanometers, several notable characteristics appear; for instance, extremely large surface area to volume ratio, better surface flexibility, higher mechanical performance (stiffness and tensile strength), and high porosity [67].

The combination of significant mechanical, thermal, chemical, and electrical properties of PVDF described in Section 2.7 with nanofibers characteristics, has made PVDF nanofibers a promising material for both micro and macro scale applications such as tissue engineering [61], protective clothing [68], nanocatalysts [69], membrane technology [70], filtration [71], and composite materials [72].

2.8.2 Nanofibers Fabrication Techniques

Recently, Almetwally, Alsaid Ahmed, et al. [73] has critically reviewed the recent production techniques for nanofibers that are summarized as follows:

- **Bicomponent extrusion (Island-in-the-sea):** spinning nanofibers using two polymers together while one polymer extrudes into another polymer. This method is also known as matrix-filament because the cross-section of fibers looks as if one of the polymers is inserted into matrix of the other polymer. In this approach, after spinning the nanofibers, one of the polymers can be removed by using heat, solvent, chemical or mechanical devices.

- **Phase separation:** this method consists of five main steps: dissolving polymer into a solvent, gelation of the obtained solution, extraction of solvent, freezing, and finally freeze-drying. The phase separation occurs due to physical inconsistency between the polymer and the solvent that forms porous nanofibrous structure after extraction of the solvent.

- **Template synthesis:** this is a common approach used to fabricate inorganic nanofibers such as carbon nanotubes. In this method, a template or mold with a nanoscale porous membrane is used to generate nanofibers with the diameters determined by the mold pores.

- **Drawing:** viscoelastic polymers are the only polymers that can be fabricated by drawing or dry spinning. In this approach, a micropipette that is controlled by a micromanipulator dips into the contact surface of a polymer droplet. By pulling back the pipette tip, a nanofiber is formed, dried, and dumped. This procedure repeats frequently on the polymer droplet to form nanofibers. The disadvantage of this method is that one nanofiber is produced in every back and forth action hindering the scaling up from laboratory-scale to industrial level.

- **Melt-blowing:** In this technology, a melt-blown die is used to convert the molten polymer to nanofibers; the molten polymer is extruded into the die while hot air (at the polymer melting point) applies a drag force to shrink the fiber thickness into nanoscale. The nanofibers coming out of the die tip are ultimately collected in a form of a non-woven mat. This technique is known as an economic spinning process of thermoplastic polymers.

- **Electrospinning:** fabrication of nanofibers using electrostatic method. This approach is the most famous, preferred, and feasible procedure to fabricate nanofibers. Therefore, this technology is explained in details in Section 2.9.

- **Centrifugal Spinning:** the most recent technology to fabricate nanofibers (although it was initially used in 1924). The advantage of this method is mass producing of nanofibers 500 times faster than traditional electrospinning. Briefly, this method utilizes electrostatic force to form nanofibers as well as centrifugal force to provide the high production rate. This approach consists of three main steps: streaming out the polymer solution by using a spinning

head, jet extension of the polymer stream to enhance the polymer surface area, and finally evaporation of solvent leading to fabrication of nanofibers.

2.9　Electrospinning

The term "electrospinning", i.e. the combination of "electrostatic" and "spinning" terms, was used for the first time in 1994 [67]; while the history of electrospinning goes back as early as 1934, when Formhals patented his invention that used electric charges to produce artificial threads [74]. Thandavamoorthy Subbiah and his co-workers did a comprehensive systematic review on the history of electrospinning from 1930s until early 2000s [75]. Recently, interest in electrospinning method has increased because of its feasibility to mass produce continuous nanofibers of various synthetic or natural polymers while the fiber dimensions can be controlled as required (from 2 nm to several μm) [76].

Electrospinning machine consists of three main components: a high voltage source, a capillary tube (pipette or needle) and a conductive (electrical) collecting surface. An illustration of electrospinning apparatus is shown in Figure 2-6.
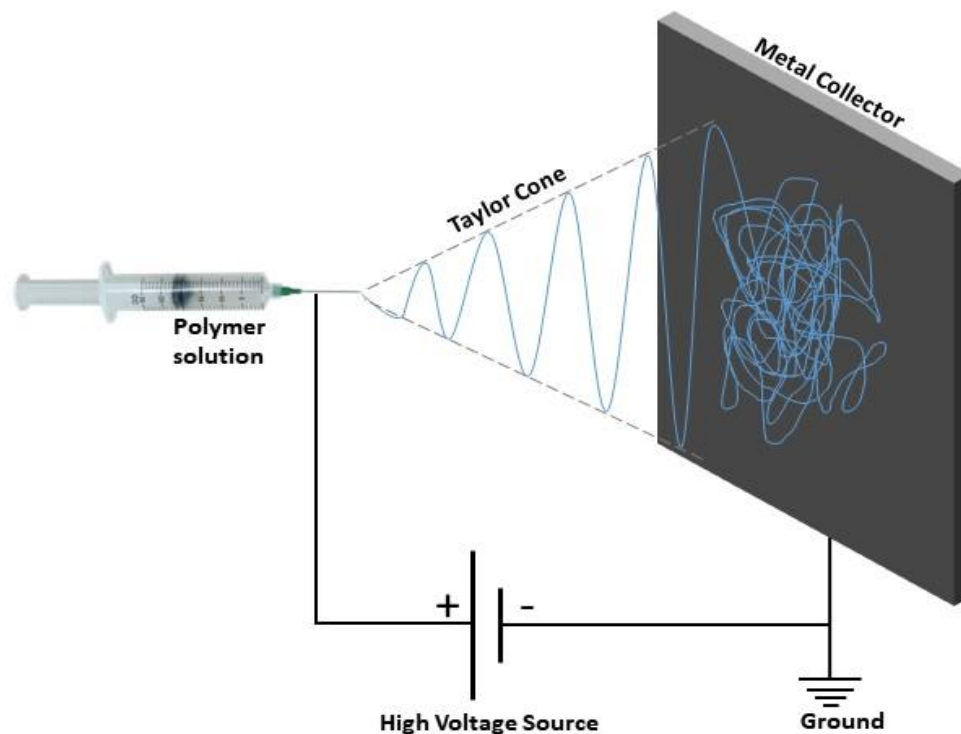
Figure 2-6: Electrospinning apparatus.

As shown in Figure 2-6, one of the high voltage source electrodes is attached to the collector surface while the other electrode is connected to polymer solution/melt (generally by attaching to the tube needle). This high voltage source generates a strong electric field that charges the polymer solution coming out of the needle [67]. Simultaneously, the corresponding repulsion of charges in polymer solution provides a force opposing its surface tension. This repulsive force, ultimately, overcomes the surface tension of the polymer droplet at the tip of the needle. Therefore, the solution flows along the direction of the electric field (i.e. from needle to collector surface). The high voltage electric field deforms the droplet into a conical shape leading to stretching of the polymer droplet and thus form an extremely fine fibers [77]. This phenomenon is known as Taylor cone after Geoffrey Taylor who formulated and described this conical shape in 1962 [78].

2.9.1 Parameters Affecting Electrospun Nanofibers

Finding the setup that leads to fabrication of smooth and bead-free electrospun nanofibers is the most challenging part of electrospinning technique. There are three types of parameters that affect the quality of the nanofibers: ambient, solution and electrospinning parameters. Haider, Adnan, Sajjad Haider, and Inn-Kyu Kang [77] and Islam, Md Shariful, et al. [76] critically reviewed the parameters and their corresponding effects on electrospun nanofibers that are summarized as follows:

Effects of Ambient Parameters

- **Temperature:** high temperature leads to a higher evaporation rate of the solvent and lower solution viscosity. Although both effects seem to follow opposite mechanisms, studies show that the effects together lead to decrease in fiber diameter.
- **Humidity:** high humidity decreases the evaporation rate that leads to formation of the non-uniform structure of fibers. This is because fibers are not solidified before reaching the collector. On the other hand, low humidity makes the solvent evaporation rate to be higher than the solution flow rate from the needle causing needle clogging.
- **Gravitational Force**: gravitational force affects the shape of the Taylor cone as well as the polymer droplet. Studies have shown that a horizontal electrospinning arrangement will require a higher flow rate (in comparison to that of a vertical arrangement) to achieve beadless fibers.

Effects of Solution Parameters

18

- **Dielectric:** higher dielectric co-efficient of the solution leads to a higher net charge density that decreases the formation of beads and fiber diameters.

- **Surface Charge Density:** higher surface charge density leads to increase in the mobility of the solution under the applied voltage. This leads to reduced fiber diameter. Low surface charge density leads to formation of beads. Fibers cannot be produced by the solutions with zero charge density due to lack of dipole moment.

- **Surface Tension:** decrease in surface tension leads to reduced fiber diameter as well as beads formation. On the other hand, an increase in surface tension causes the solution to assume a spherical shape that forms beads.

- **Molecular Weight:** sufficient molecular weight is a key parameter. Decreasing molecular weight (while solution concentration is constant) leads to formation of beads while increasing molecular weight leads to formation of smooth fibers. Excessive increase of molecular weight forms micro-ribbon fibers.

- **Polymer Concentration:** low polymer concentration leads to reduced viscosity and increased surface tension of the solution. Therefore, a discrete stream of solution forms the Taylor cone. High concentration, on the other hand, forms a mixture of beads and fibers.

- **Viscosity:** high viscose solutions form spindle like beads and cause needle tip clogging. On the other hand, low viscous solutions form a discrete Taylor cone. Thus, a threshold value of solution viscosity is required to achieve continuous and bead free fibers.

- **Solution Conductivity:** Solution conductivity plays a crucial role in electrospinning. High conductivity of solution increases the charge on the surface that leads to reduced fiber diameters. However, increasing conductivity beyond a threshold value stops the formation of Taylor cone and hinders electrospinning process.

- **Solvent Boiling Point:** solvents should have a moderate boiling point. Highly volatile solvents dry out the solution at the tip of needle that clogs the needle tip. On the other hand, a less volatile solvent leads to formation of beads since the solution reaches the collector before it gets solidified.

Effects of Electrospinning Parameters

- **Applied Voltage:** higher voltage leads to increase in the electrostatic force that reduces fibers diameters. Also, a higher voltage improves degree of crystallinity that increases density and

hardness of the collected fibers. However, by increasing voltage more than a threshold value, crystallinity of jet gets decreased due to a shorter flying time.

- **Needle Diameter:** increasing the needle diameter leads to larger fibers size.
- **Needle to Collector Distance:** this parameter affects the morphology and diameter of fibers; however, the distance between the needle and collector is one of the least effective parameters. Short distance leads to formation of beads because the solution may not be solidified before reaching the collector (the solvent has a shorter time to evaporate). On the other hand, increasing distance leads to a reduction in average fibers size.
- **Collector Type:** Based on the application, there are variety of collectors to be used: pin type, wire mesh, plate, parallel ridges series, grids, parallel bars, rotating wheel, liquid non solvent, etc. Rotating collector helps achieve aligned fibers. The rotating motion of the collector also favors the drying-up of fibers. Collector speed is a critical parameter in rotating collector. The collecting speed that leads to obtaining aligned fibers is known as alignment speed. If the collector rotates lower than its alignment speed, less-oriented fibers may be achieved.
- **Flow Rate:** flow rate is one the key parameters to determine the diameter, porosity, and geometry of fibers. Increasing the flow rate leads to an increase in the diameter, pore size as well as formation of beads.

2.10   Surface Hydrophilic Modification of PVDF

Hydrophilicity and hydrophobicity are two of the most noticeable surface characteristics in material science that are defined by contact angle θ, i.e. the angle between the liquid surface and the outline of the solid material that is in contact with it. Conventionally, a material in solid phase is considered hydrophilic if a static water droplet exhibits a contact angle $\theta < 90°$ and it is considered hydrophobic if contact angle $\theta > 90°$. In a similar way, super hydrophilicity and super hydrophobicity are also defined by contact angle of $\theta = 0°$ and $\theta \geq 145°$ respectively [79].

The hydrophobic nature of PVDF surface is one of the issues that hinders PVDF from being used in biotechnology, pharmacy and biomedical related applications where hydrophilic materials are required [80]. To enhance the hydrophilicity of PVDF, variety of modifications have been investigated: mixing with polyethylene glycol (PEG), casting a chitosan thin layer on the PVDF surface, introducing polyaniline nanofibers, cross-linking with polyethylenimine, plasma

treatment and polymerization with hydroxyethylmethacrylate are some the approaches that have been used [81].

PVDF surface modification approaches are classified into two main categories:

- **Physical modification:** introducing a hydrophilic modifier that has a physical interaction with PVDF surface. This approach is achieved either by coating/depositing a hydrophilic polymer on the PVDF surface, or immobilizing/cross-linking of a hydrophilic modifier after immersing PVDF into a solution that contains the active monomers.

- **Chemical modification**: modification of PVDF surface by using covalent bonding interaction. In this approach, a chemical reaction or a high-energy radiation is used to excite PVDF chains to graft with a hydrophilic modifier. Defluorination-sulfonation, O_3/O_2 preactivation, electron beam radiation, and plasma treatment are some examples of chemical surface modification of PVDF to enhance hydrophilicity [57].

2.11   FCBPSS Framework

In advanced design methodology, to design, develop or optimize any system (whether it is a mechanical, electrical or a biological system), the full understanding of the system concepts is the first step which any designer is recommended to take. FCBPSS (Function-Context-Behavior-Principle-State-Structure) architecture is one of the complete approaches for identification of the system concepts and its details.

2.11.1 Definition

Since 1960s and 1970s, many researchers have proposed a variety of terminologies that describes a comprehensive system architecture in order to assist designers in conceptual design [82]. A number of proposed approaches had a solidarity to divide the design into the terms: Function (F), Behavior (B) and Structure (S); however, they failed to map the terms successfully [82]. From mid 1980s to the mid-1990s, FBS (Function-Behavior-Structure) ontology was first developed in the area of Artificial Intelligence and then became dramatically popular in constructing conceptual models [82][83].

In 2000, the FBS framework was extended by introducing sFBS (Situated Function-Behaviour-Structure). sFBS architecture makes use of three terms to map Function, Behavior and Structure:

the external world, the interpreted world, and the expected world and interactions between them [84].

In 2004, the concepts of Effect (E) was introduced for the first time into the FBS framework to map between the Behavior (B) and the Function (F) of the system [85].

Finally, in 2005, further elaboration led to introduction of an applicable framework known as FEBPSS (Function-Effect-Behavior-Principle-State-Structure) [86]. The concept of Effect (E) can be substituted with the term Context, Constraint or Condition (C) leading to a general conceptual design architecture known as FCBPSS (Function-Context-Behavior-Principle-State-Structure). Figure 2-7 illustrates the FCBPSS framework and the relations between each concept.
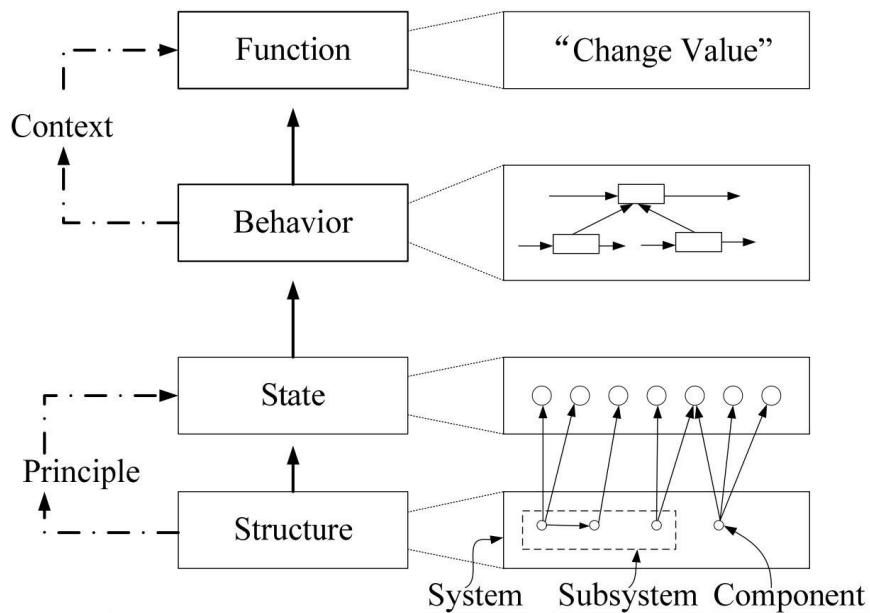
Figure 2-7: FCBPSS framework (Reproduced from [87]*).*

The terms of this approach are explained as follows [88];

F: Function (the task which the system is supposed to do)

C: Context (the condition and environment in which system is located)

B: Behavior (the relationship between system variables such as input and output)

P: Principle (the rule or fundamental that the system obeys)

S: State (the characteristics of each subsystems)

S: Structure (the connections between sub-systems)

2.11.2 FCBPSS-based Design Process

FCBPSS-based design is an application of FCBPSS architecture in a process (e.g. engine process) which requires four steps to be taken: first, developing the context and function of the desired system (e.g. compress the gas); second, finding the states (e.g. displacement and rotation) and behavior of the system (e.g. change the volume of the chamber); third, finding the related principle to produce system behavior (e.g. relation between rotation and displacement); and fourth, proposing the structure of desired system (e.g. crank-slider mechanism) [88]. Figure 2-8 illustrates the concepts of FCBPSS-based design process.
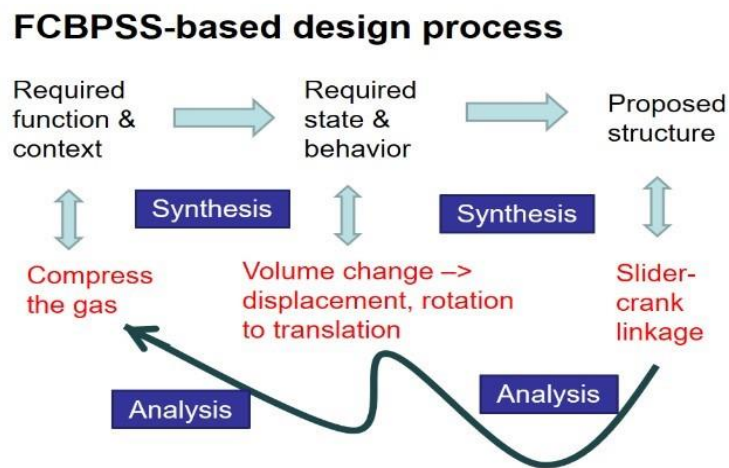
Figure 2-8: FCBPSS-based design process (Reproduced from [88] *by permission from Taylor & Francis)*

2.12 Systematic Design Theory

Systematic Design (SD) theory (also known as German approach) is explained in details in the book titled, "Engineering Design - A systematic Approach" [89]. Briefly, to solve technical problems, the SD theory introduces function of a system as the relation between input and output of the system. Each system function can be divided into sub-functions. By determining the relationships between the system sub-functions, a function structure can be represented. It is worth noting that Function structure of a system is not a unique structure so that different function structures can represent the functional interrelationships of a system; however, the overall function is required to be satisfied by each function structure [89]. A general function structure and interrelationships between the sub-functions are shown in Figure 2-9.
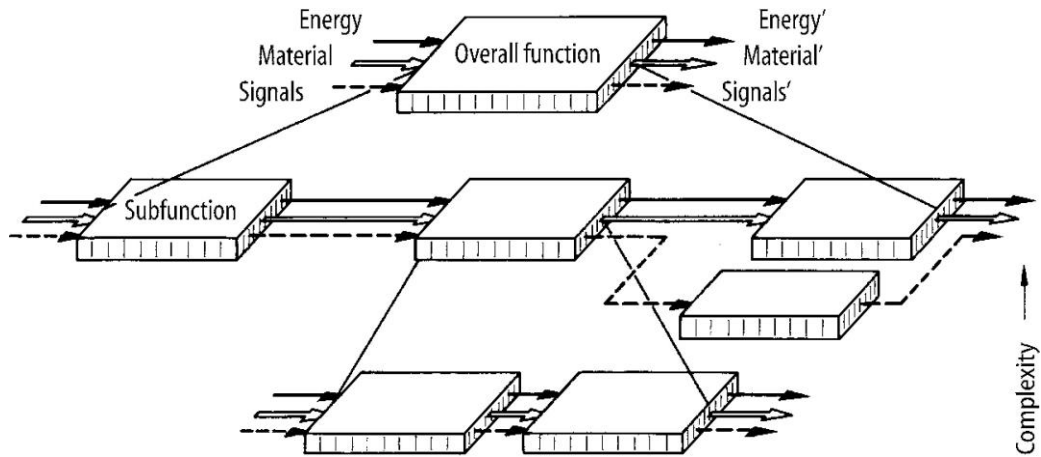
Figure 2-9: A general function structure made by breaking down an overall function to sub-functions (Reprinted by permission from Springer Nature: Springer eBook Engineering Design by Gerhard Pahl and Wolfgang Beitz ©Springer-Verlag London 1996 [89]).

In general function structure, the main function is defined as the functions which directly contribute to satisfaction of overall function, and auxiliary function is defined as the functions which indirectly contribute for overall function satisfaction.

Theoretically, to represent function structure in a generally valid description, functions can be subdivided and classified so that the lowest level of the function structure consists of simplified sub-functions that cannot be subdivided further [89]. Figure 2-10 indicates the generally valid functions introduced by Krumhauer that can be used to represent function structure of a system with a higher level of abstraction.

2.13   Axiomatic Design Theory

The main challenge of any designer is to choose a design approach that ensures the design performs the required tasks with the highest probability of success. This can be even more challenging when the system has many Function Requirements (FRs) and Design Parameters (DPs). Conceptual design is one of the early stages of a design process. A general conceptual design theory to reduce the complexity of system is presented by Nam. P. Suh and known as Axiomatic Design Theory (ADT) [90]. Briefly, ADT consists of two axioms: Axiom 1 and Axiom 2. The first axiom known as independence axiom states that FRs are always supposed to maintain their independence. The second axiom known as information axiom states that the best design is the one which has the highest probability of functional success while also satisfying Axiom 1 [90].
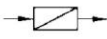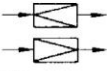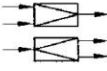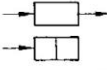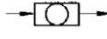
Characteristic Input (I)/Output (O)	Generally valid functions	Symbols	Explanations
Type	Change		Type and outward form of I and O differ
Magnitude	Vary		$I < O$ $I > O$
Number	Connect		Number of $I > O$ Number of $I < O$
Place	Channel		Place of $I \neq O$ Place of $I = O$
Time	Store		Time of $I \neq O$

Figure 2-10: Generally valid functions derived from the characteristics type, magnitude, number, place and time for the conversion of energy, materials and signals (Reprinted by permission from Springer Nature: Springer eBook Engineering Design by Gerhard Pahl and Wolfgang Beitz ©Springer-Verlag London 1996 [89]).

For fixed systems whose system components do not change as a function of time, 3 steps are required to maintain Axiom 1 [91]:

2.13.1 Step1: Determination of FRs and Constraints (CRs)

FRs are a set of minimum independent requirements that satisfy the design goal. It is noted that to increase the creativity, the FRs are supposed to be defined without considering the solution. CRs are the constraints of the system that are supposed stay unaltered.

2.13.2 Step2: Mapping FRs to DPs

Design parameters (DPs) are set of parameters that are "hows" for the FRs. DPs are defined in a way that there is no conflict between DPs and CRs. This step consists of mapping the functional domain to the physical domain (i.e. mapping FRs to DPs). The mapping process can be mathematically expressed by:

$$[FR] = [A][DP] \tag{2-2}$$

where [FR] is the functional domain vector, [DP] is the physical domain vector and [A] is the design matrix [91].

25

2.13.3 **Step3: The Independence of System Functions**

In order to maintain the Axiom 1, the designer is supposed to keep the FRs independent during the mapping process that is when one of the DPs is changed, it changes only one FR. Mathematically, the design matrix [A] can be either diagonal, triangular or none.

If the design matrix is diagonal that means each of the FRs is satisfied only by one of the

DPs. This design is called uncoupled design and can be mathematically expressed by:

$$\begin{bmatrix} FR_1 \\ FR_2 \\ FR_3 \end{bmatrix} = \begin{bmatrix} A_{11} & 0 & 0 \\ 0 & A_{22} & 0 \\ 0 & 0 & A_{33} \end{bmatrix} \begin{bmatrix} DP_1 \\ DP_2 \\ DP_3 \end{bmatrix} \tag{2-3}$$

If the design matrix is triangular, that means the independence of FRs can be guaranteed if the change of DPs happens in a specific sequence. This design is called decoupled design and can be mathematically expressed by:

$$\begin{bmatrix} FR_1 \\ FR_2 \\ FR_3 \end{bmatrix} = \begin{bmatrix} A_{11} & 0 & 0 \\ A_{21} & A_{22} & 0 \\ A_{31} & A_{32} & A_{33} \end{bmatrix} \begin{bmatrix} DP_1 \\ DP_2 \\ DP_3 \end{bmatrix} \tag{2-4}$$

Finally, any other forms of design matrix are called coupled and violates Axiom 1. Therefore, any designer must determine FRs and DPs such that the resulting design matrix is either diagonal or triangular [91].

3   DESIGN

In this chapter, the design process of PVDF as a porous channel substrate in an MFC system is described. First, the FCBPSS framework theory introduced in Section 2.11 is used to describe the PVDF-based channel system. After finding the most suitable channel structure, Axiomatic Design Theory (ADT) introduced in Section 2.13 is used to verify if the DPs of PVDF channel satisfy the FRs independently. Finally, a detailed design of the MFC system is described at the end of this chapter.

3.1   Conceptual Design: FCBPSS Framework

Before explaining the PVDF channel system in the concept of FCBPSS framework, the exact location of the channel system and its relations with its surrounding systems such as other MFC sub-systems, implantable/wearable device and patient's biological organs are clarified. A schematic example of the patient's body system and its sub-systems are illustrated in Figure 3-1. As shown in Figure 3-1, the channel system, as a sub-system of the MFC, is only in relation with the MFC sub-systems: the electrodes system, the absorbent pad system, the fuel system, and the fuel reservoir system. Simultaneously, the MFC system, as a sub-system of an implantable/wearable devices, has in relation with the device's sub-systems. Also, the implantable/wearable device, in respect with its function and its location in a patient's body and, has relation with the respective biological organs.

It is worth mentioning that the illustration in Figure 3-1 is only one example of the relations among many possible biological systems dealing with an implantable/wearable device, and based on the location and the function of an implantable/wearable device, the relations can be changed. However, regardless of the function of the implantable/wearable device and its location in the patient's body, the MFC channel system relations remain unchanged (i.e. the channel system is only in relation with the electrodes system, the fuel system, the absorbent pad system, and the fuel reservoir system).

In order to identify and introduce the PVDF channel system in the concept of FCBPSS architecture, the steps explained in Subsection 2.11.2 are as follows.

3.1.1 **Function**

Function is defined based on our expectation from the system. PVDF channel system for MFC application is expected to deliver fuel from fuel reservoir to the absorbent pad by providing a constant capillary flow of fuel. Also, the system is expected to facilitate moving of hydrogen ions (protons) from anode to cathode by providing laminar flow of fuel. As a summary, function of the channel system is categorized into two parts: 1. Providing a constant capillary flow of fuel, and 2. Facilitating hydrogen ions flow.
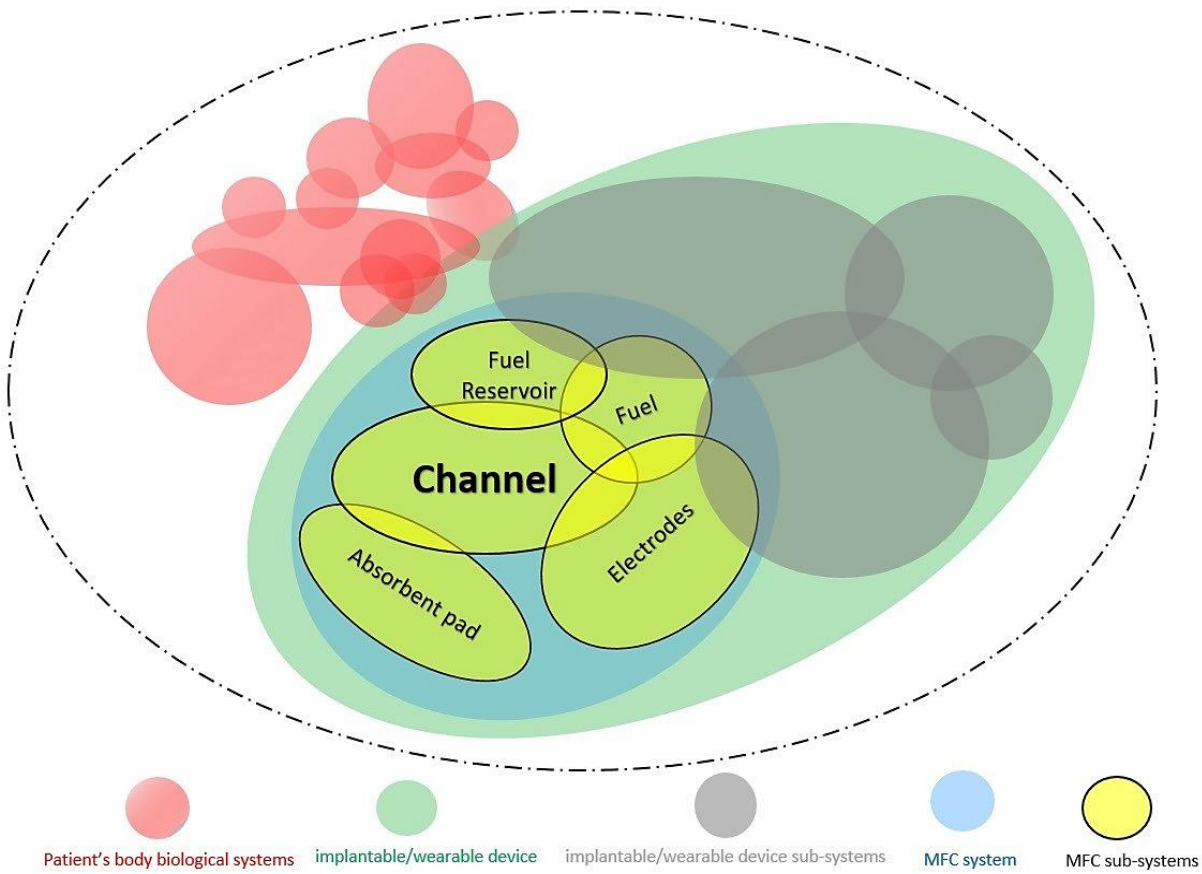
Figure 3-1: A schematic example of the patient's body system and the relations of its subsystems

3.1.2 **Context**

System context is defined by three parameters:

- **Pre-condition:** pre-condition is supposed to be always true before any other conditions and parameters act. In the concept of PVDF channel system for MFC application, fuel is the pre-condition; without presence of fuel, other conditions cannot be fulfilled.

- **Post-conditions:** to facilitate capillary action of fuel into the PVDF channel, after fulfilling the pre-condition, which is the presence of fuel, two post-conditions are required to be fulfilled; porosity and hydrophilicity. It is noted that low-viscosity of fuel plays a key role for capillary flow of fuel into the channel; however, low-viscosity of fuel cannot be considered as a post-condition for PVDF channel system. It can be considered as post-condition for fuel system.

- **Environment:** recognizing the channel system environment can be confusing. It is known that the goal of PVDF channel for MFC application is to be used as a biocompatible and flexible substrate. Therefore, one may recognize the environment of channel system as the patient's body; however, based on Figure 3-1, the environment of the channel system is MFC system.

It must be noted that the patient's body cannot be considered as the environment of MFC system. The human body is a complex system containing vessels, muscles, and variety of organs with different characteristics and based on location of implantable device inside the patient's body, the environment changes dynamically. For an example of a device implanted in a blood vessel; blood pressure, blood components such as RBC (red blood cells), white blood cells etc. present in blood and their interactions such as chemical reactions, mechanical reactions (pressure, velocity, collisions, etc.) are required to be considered as environment features of the implantable device system.

3.1.3 **State**

State is related to the characteristics and variables of subsystems and depends on the purpose of the system. The state variables of PVDF channel system for MFC application based on the system function described in Subsection 3.1.1 are listed as follows:

- fuel flow

- diffusion flux

3.1.4 **Behavior**

PVDF channel system deals with fuel flow entering the channel inlet and mixture of excessive fuel and redox by products coming out of the channel outlet. Therefore, behavior of the channel system which is the relation between the input and output is simplified in Figure 3-2.

Figure 3-2: Simplified behavior of PVDF channel system

In order to illustrate details of channel system behavior, systematic design approach explained in Section 2.12 is utilized. Figure 3-3 illustrates the more detailed behavior of the PVDF channel system.
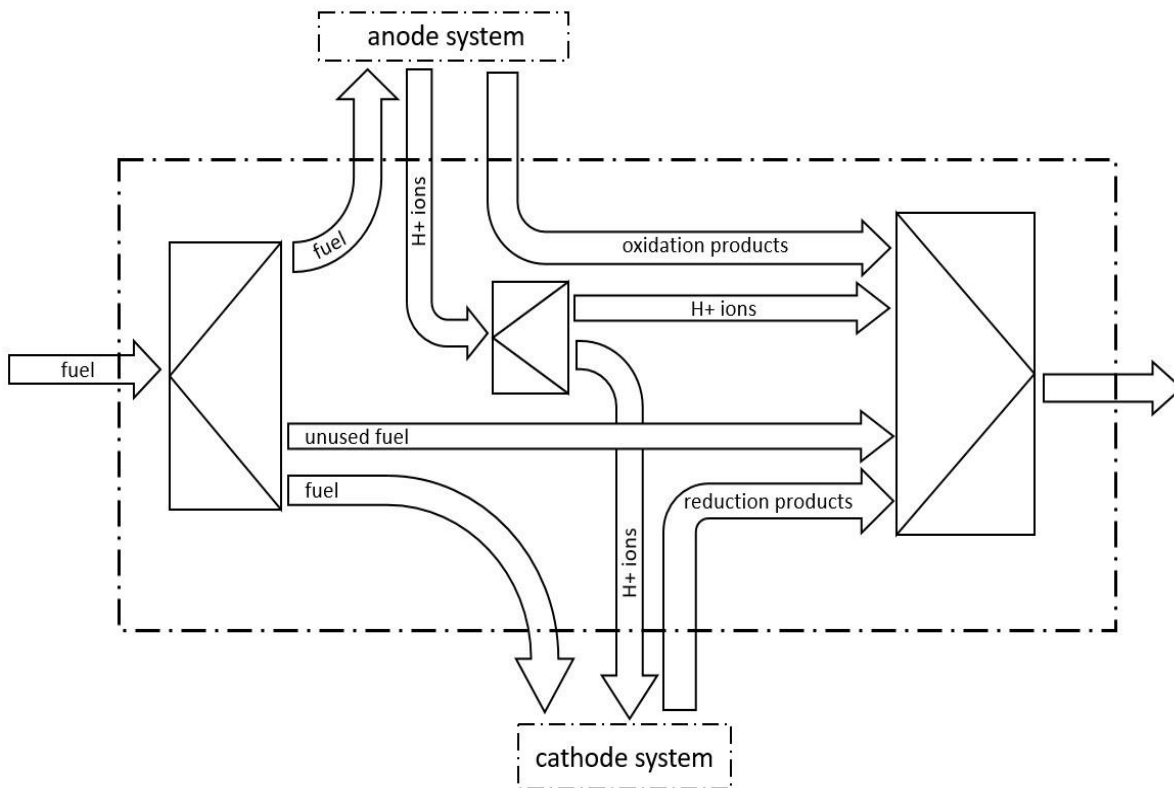
Figure 3-3: Generalized systematic design diagram of the behavior of PVDF channel system for MFC application.

3.1.5 Principle

Principle is the laws governing the behavior (i.e. relationship between inputs and outputs) of the system and can be determined by finding how and why the system exhibits that behavior. In the concept of PVDF channel system, one can answer the questions like how does the channel transfer fluid from inlet to outlet and? how does the channel transfer hydrogen ions from anode to cathode? The answers to these questions (i.e., principles) are shown in Table 3-1.

Table 3-1: Principles governing the behavior of PVDF channel system

Behavior	Input	Output	Reason	Principle
Transfer fuel	Fuel	Unused fuel and redox by-products	Capillary action	Capillary penetration in porous materials (Lucas Washburn)
Mix fuel and redox by-products	Fuel	Mixture of unused fuel and redox by-products	Different concentration	Dispersion equation in porous materials
	Oxidation products			
	Reduction products			
	H+ ions			
Transfer hydrogen ions between cathode and anode systems	H+ ions	H+ ions	Different concentration	Molecular diffusion in co-laminar flow (Fick's law)

Capillary Penetration in Porous Materials (Lucas-Washburn's Equation)

Fluid flow in narrow spaces such as plant vessels and fine tubes without exterior assistance is known as capillary action or capillary flow. Capillary flow of a liquid in a tube happens when the adhesive force between liquid and tube surface overcomes the cohesion force within liquid molecules. This net force of cohesion and adhesive forces is known as capillary force.

The phenomenon of penetrating liquid into the porous materials such as paper is known as capillary penetration and it is proved that capillary penetration shares a similar dynamic mechanism with capillary flow in tubes [92]. Richard Lucas in 1918 and Edward W. Washburn in 1921 illustrated and formulated dynamic mechanism of capillary penetration in porous materials under its own capillary pressure which is known as Lucas-Washburn's equation [93][94]. The modified Lucas-Washburn's equation for horizontal capillary penetration in porous media under its own capillary pressure is:

$$L^2 = \left(\frac{\gamma}{\eta}\frac{cos\theta}{2}\right)rt \tag{3-1}$$

In Equation 3-1, L is the distance which the liquid will penetrate, γ is the surface tension of the liquid, θ is contact angle of liquid, η is the viscosity of the liquid, r is the radius of capillary or pore radius and t is time.

The term $\left(\frac{\gamma}{\eta}\frac{cos\theta}{2}\right)$ shows the penetration ability of a liquid and is called the coefficient of penetrance or penetrativity. Based on Equation 3-1, the penetrativity can be described as "the distance which the liquid will penetrate a capillary tube of unit radius in unit time" and its dimension is equal to liquid penetration rate [94].

Additionally, the rate of penetration can be derived from by Equation 3-1 neglecting air resistance and taking a derivation with respect to time [94]. The result is penetration rate of liquid into the porous material under its own horizontal capillary pressure:

$$\frac{dl}{dt} = \left(\frac{\gamma}{\eta}\frac{cos\theta}{2}\right)\frac{r}{2l} \tag{3-2}$$

Dispersion Equation in Porous Materials

The interaction of solid phase and fluid phase in porous media (e.g. PVDF nanofibers) is complex. This complexity makes boundary conditions required to define mathematical description of fluid flow too complex to be modeled. By using a continuum approach based on principle of mass conservation in macroscopic scale and Fick's first law of diffusion, Equation 3-3 which is known as convection-dispersion equation is derived [95].

$$\frac{\partial C_i}{\partial t} + \nabla.C_i\bar{u} = \nabla.\rho D_o x_i + r_i \tag{3-3}$$

In Equation 3-3,

C_i = concentration of species i (mass per unit volume),

t = time

u^- = mass average velocity vector (length per unit time),

ρ = fluid (mixture) mass density (mass per unit volume),

D_o = molecular diffusion coefficient (length squared per unit time),

x_i = mass fraction of species i ($x_i = c_i/\rho$),

and r_i = source or sink term (mass of i per unit volume per unit time).

In different directions of a porous material, due to the complexity of pore structure, mechanical mixing of fluids is different. Therefore, a measure of mixing during flow is defined as a tensor

quantity known as dispersion coefficient of porous materials (K_L). At low velocities, it is known that K_L is equal to apparent molecular diffusion coefficient in the porous medium (D_{app}). D_{app} is smaller than the molecular diffusion coefficient (D_o) because of porosity feature of material [95]. D_{app} is measured by experiment.

In PVDF channel, the following assumptions can be considered:

- $D_o = K_L = D_{app}$

- D_{app} is constant

- Fluid density (ρ) is constant

- Fluid flows only in one direction (e.g. x direction alongside the channel length)

- $\bar{u} = \dfrac{\bar{Q}}{A\varphi}$

  where,

  $\bar{Q}$= volumetric flow rate (volume per unit time),

  A=porous medium cross-sectional area (length squared),

  ϕ=porosity,

  and x= distance [95],

- There is no rate of consumption or generation of species i (elimination of r_i).

  Therefore, Equation 3-3 can be simplified to Equation 3-4:

$$\frac{\partial C_i}{\partial t} + \frac{\bar{Q}}{A\varphi}\frac{\partial C_i}{\partial x} = D_{app} \times \frac{\partial^2 C_i}{\partial x^2} \tag{3-4}$$

Diffusion in laminar flow (Fick's first law)

Hydrogen ions (protons) diffuse into the layer of laminar flow of fuel. Fick's first law of diffusion determines the principle governing the diffusion of hydrogen ions shown in Equation 3-5 [96].

$$J = -D\frac{\partial C}{\partial y} \tag{3-5}$$

In Equation 3-5,

J = diffusion flux in [$mol.m^{-2}.s^{-1}$],

D = diffusion coefficient in [$m^2.s^{-1}$],

C = concentration of the species or protons in [$mol.m^{-3}$],

and y = position in [m]. It must be noted that y is perpendicular to x direction (alongside the channel length).

3.1.6 Structure

Variety of channel structures have been utilized for MFC-based studies. Figure 3-4 illustrates I, Y, F, O and T channel structures.

All the channel structures can fulfil the PVDF channel functions, behaviors, principles, states, and context. In this research, for fabrication simplification, I-shaped structure was selected. Additionally, I-shaped channel structure is more compatible with utilizing hydrogen peroxide as fuel and oxidant at the same time.
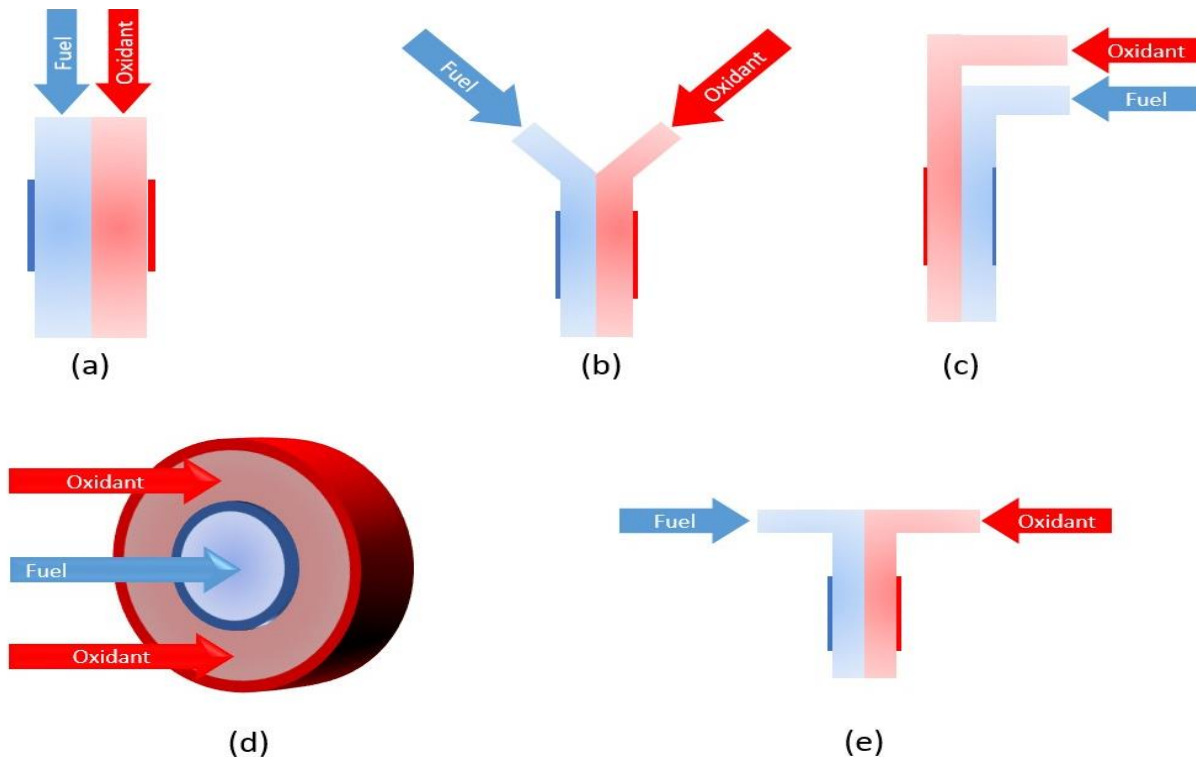
Figure 3-4: An illustration of different channel structures in MFC systems application. Anode and cathode electrodes are shown with thick blue and red colored lines, respectively. (a) I-shaped channel. (b) Y-shaped channel. (c) T-shaped channel. (d) O-shaped channel. (e) T-shaped channel.

3.2 Conceptual Design: Axiomatic Design

In this section, an axiomatic design for PVDF channel system is identified based on ADT introduced in Section 2.13.

3.2.1 Step1: Determination of FRs and Constraints (CRs)

The first step to analyze PVDF channel system in ADT concept is to identify general function requirements (FRs). These FRs are obtained from the systematic design analysis of the system, identified before in Figure 3-3, where system behavior is determined based on FCBPSS architecture. Therefore, based on Figure 3-3, FRs of PVDF channel system are as follows:

- FR_1: the channel system must soak up fuel from inlet and carry it towards outlet.

- FR_1: the system must facilitate hydrogen ions movement.

After FRs determination, based on ADT, system constraints (CRs) are determined as follows:

- CR_1: the substrate must be hydrophilic,

- CR_2: the channel structure must avoid direct physical contact between electrodes.

3.2.2 Step2: Mapping FRs to DPs

Design Parameters (DPs) are determined in physical domain to satisfy the FRs and constraints:

DP_1: nanoscale pore structure that compromises paths to induce capillary action.

DP_2: channel diameter in micro-scale to generate laminar flow (low Reynold's number).

Based on ADT, DPs are supposed to be determined so that they have no conflict with CRs. As it is explained in the follows, DP_2 has a conflict with CR_2:

PVDF channel is assumed to have a rectangular cross-sectional area fully filled by fluid. In this way, the channel diameter (known as Hydraulic diameter) is calculated by the following equation:

$$D_H = \frac{2WT}{W + T} \tag{3-6}$$

Where W and T are the channel width and channel thickness, respectively.

Based on CR_2, to avoid physical contact between electrodes, the channel width should be in macro-scale ($\gg 100 \mu m$). Since channel width is much larger than channel thickness $(W \gg T)$, Equation 3-6 is simplified to:

$$D_H = 2T \tag{3-7}$$

Based on Equation 3-7, to have D_H in micro-scale, channel thickness is supposed to be less in micro-scale. Therefore, a new DP is determined:

• DP_{2*}: channel thickness in micro-scale.

Mapping the FRs to DPs are illustrated as follows:

FR₁: fuel absorption $\xleftarrow{\text{satisfies}}$ **DP₁**: nanoscale pores and paths (promising capillary action)

FR₂: hydrogen ions movement (by diffusion) $\xleftarrow{\text{satisfies}}$ **DP₂***: channel thickness in microscale (promising laminar flow)

3.2.3   Step3: The independence of system functions

The overall relationship between FRs and DPs is shown mathematically as follows:

$$\begin{bmatrix} FR_1 \\ FR_2 \end{bmatrix} = \begin{bmatrix} A_{11} & 0 \\ 0 & A_{22} \end{bmatrix} \begin{bmatrix} DP_1 \\ DP_{2*} \end{bmatrix} \tag{3-8}$$

The diagonal matrix shown in Equation 3-8 verifies that the design is uncoupled that is the DPs satisfy FRs independently.

3.3   Conceptual Design: Conclusion

The FCBPSS-based design approach is demonstrated to be an effective tool to conduct design of the fuel system; in particular, it helps to identify the function and constraint of the PVDF channel system under design and to identify the concepts of the system, and to proceed with the embodiment design and detail design step by step. Additionally, since it is possible that several structures are obtained from behavior, state, principle, function and context of the system, this approach may help the designer to classify the details of the system in order to compare and find the most compatible structure. In this section, by using FCBPSS, the I-shaped structure was determined as the most compatible structure. The design is represented by FR, CR, and DP. Further, ADT was employed to lead to the I-shaped PVDF structure, which meets Axiom 1 in ADT, namely it is a good design.

3.4   Detailed Design: PVDF-Based MFC

The MFC was designed as an I-shaped MFC (based on the discussion in Subsection 3.1.6). The design specification was derived from [35] and [97] with some modifications.

The absorbent pad was considered a circular shape to maintain a quasi-steady flow that was previously described in [98]. Briefly, while the fuel travels through the channel by capillary force, the flow rate starts to drop due to increment in the viscous drag force. A circular geometry in the absorbent pad provides an increment in the surface area while the fuel gets absorbed by the pad. This increment in the surface area increases the pulling capillary force. The cancellation of increment of the two forces (capillary force and drag force) lead to a quasi-steady flow i.e. a constant flow rate of fuel into the channel system.

A rough design of the MFC structure is shown in Figure 3-5.
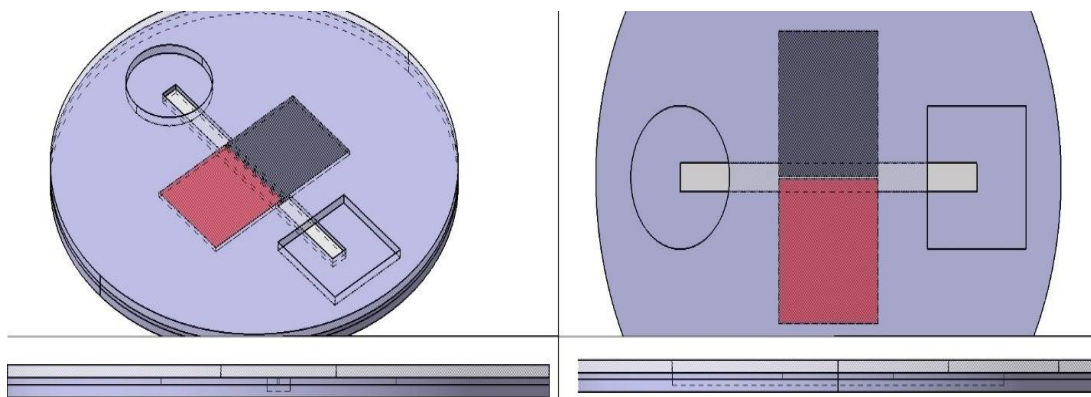
Figure 3-5: A rough design of the MFC structure: a microfluidic channel made by PVDF substrate, two electrodes on the channel path, a circular absorbent pad, and a square shape solution reservoir

The MFC was designed to be fabricated using micro-fabrication techniques (UV-lithography). The design structure consists of four main parts:

- Square shaped reservoir where fuel can be injected to start the electrochemical reaction.

- Circular absorbent pad to maintain the fuel flow with a constant flow rate.

- Microchannel (connecting the reservoir to absorbent pad).

- Electrode coated with respective catalysts located on the opposite sites of the channel path.

The design and fabrication steps are explained in details in Appendix B: MFC Microfabrication Method. Briefly, the MFC consists of 3 main layers fabricated by UV-lithography: channel substrate holder made by SUEX, electrodes holder made by SUEX and a PDMS layer to define the absorbent pad and reservoir geometry and a system cover to avoid contamination and

37

evaporation during experiment. The electrodes and PVDF substrate are assembled between these three layers (for illustration, see Figure B- 1).

The UV-lithography micro-fabrication method for PVDF-based MFC faced several obstacles:

- Assembly and alignment of micro-fabricated three layers are challenging and time consuming

- The MFC is supposed to be tested for several times. However, after assembling and alignment of the layers, changing the channel substrate or electrodes are not doable.

- Cutting the PVDF substrate to form the micro-channel is not doable. Also, electrospinning the PVDF directly on the channel substrate is not doable due to non-conductivity of SUEX.

- PVDF-based MFC induced by capillary induced flow is not tested before and Micro-fabrication method is not a suitable method for prototyping.

Based on the obstacles described above, the microfabrication method was not chosen to fabricate the PVDF-based MFC in this research. Therefore, the MFC was re-designed to be fabricated using the 3D printing method. The MFC was designed in two main pieces: main body and channel holder. The MFC system and two main layers CAD designs are shown in Figure 3-6.
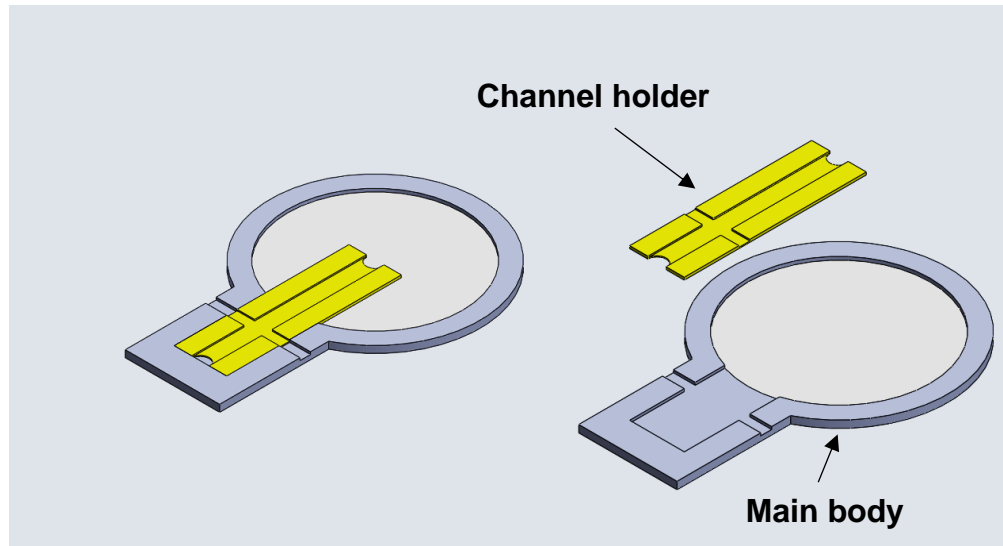
Figure 3-6: PVDF-based MFC CAD design

3.4.1 **Main Body**

The main body was designed as a support for the MFC components: channel, electrodes, and absorbent pad. A circular pothole (depression) with the depth of 200 μm (0.2 mm) and diameter

of 50 mm was considered to support the absorbent pad and two slots with the width of 3 mm were considered to support the electrodes. The final length of the MFC was 88 mm, the diameter of outer ring of the absorbent pad was 60 mm.

The drawing of main body is shown in Figure A- 1.

3.4.2 **Channel Holder**

A holder was designed to support the channel, define the absorbent pad, and support the electrodes. Two semicircular holes were designed for the inlet and outlet of the channel for better physical connection of channel substrate with the absorbent pad and the reservoir.

The drawing of channel holder is shown in Figure A- 2.

4 FABRICATION

In this chapter, the process of fabricating a porous PVDF channel substrate using the electrospinning method (described in Section 2.9) is explained. First, in Section 4.1 (Electrospinning Device), details of how the electrospinning device was fabricated from scratch are described. Second, in Section 4.2 (Electrospinning of PVDF), details of PVDF solution preparation and electrospinning of PVDF nanofibers are described. Finally, Section 4.3 (MFC System) describes the method used to fabricate the PVDF-based MFC.

4.1 Electrospinning Device

Among the seven techniques to fabricate nanofibers reviewed in Subsection 2.8.2, in this research, the electrospinning method was selected to fabricate PVDF nanofibers due to its feasibility to develop the device in the lab environment, flexibility of electrospinning device to fabricate aligned and non-aligned nanofibers, availability of electrospinning parameters settings for PVDF nanofibers in the literature, and availability of device components in our group.

There are variety of reputable companies manufacturing industrial/lab-scale electrospinning devices. However, the electrospinning device used in this research was made from scratch with the reasons to be present subsequently. In the rest of this section (Section 4.1), the design and fabrication of this proprietary electrospinning device is described.

4.1.1 Collector: Rotating Drum

Rotating drum is an essential component to achieve aligned nanofibers. The rotating drum requirements in this research (as it was suggested in [16]) are speed of 1500 rpm and diameter of 10 cm. The other requirements for a lab-scale rotating drum collector are enduring long hours of operation, having no vibration, and be electrically conductive.

Three available options were evaluated to develop the rotating drum:

- Purchasing commercial rotating drum: mounting and alignment of the commercial rotating drums are challenging. Furthermore, the companies selling electrospinning machines do not

offer an affordable price for parts since most rotating drums are being sold with complete setup of electrospinning machine.

- Modification of metallic pipe/rod: one option is to modify a metallic pipe/rod with the diameter of 10 cm. This option requires several sensitive procedures such as: cutting, welding and alignment. Three materials are evaluated: stainless steel, carbon steel and aluminum. Stainless/carbon steel has relatively lower electrical conductivity in comparison with aluminum. Also, stainless/carbon steel is about 3 times denser than aluminum requiring high torque motor. Balancing and alignment of a denser drum is also challenging. On the other hand, aluminum has higher electrical conductivity and less dense; however, aluminum welding is costly and difficult.

- 3D Printing: this technique is a feasible and fast technique for prototyping. However, the polymer materials used in 3D printing are not electrically conductive.

After evaluation of the options explained above, 3D printing technique was selected to develop the rotating drum. Therefore, the required drum and shaft were designed as one piece by CAD (Computer-aided Design). The design drawing is shown in Figure A- 3. The drum prototype was fabricated by JGAurora A5 3D printer machine using polylactic acid (PLA) filament.

A mini-vac pump motor (Model M40, 115 Volt AC, 150 Watts, 60 Hz, manufactured by Simer Pump Company, Minneapolis, USA) was used as the drum motor. The shaft outer diameter of motor is 8 mm.

A lightweight steel plate pillow type mounted bearing (SBPP202-10E, manufactured by FYH) with the 5/8 inches (15.9 mm) inner diameter bearing was used to support the drum.

A coupling of 8 mm to 5/8 inches made by lathe machine and aluminum rod was used to couple drum shaft to the motor. However, after mounting the couple, the drum shaft started to slip inside the aluminum coupling and tightening harder the coupling screw could not help due to deformation of the PLA shaft inside coupling causing angular offset misalignment. To solve the slipping problem, a new coupling of 8 mm to 5/8 inches made by milling machine and plastic rod of 1 inch outside diameter was used to couple drum shaft to the motor.

41

After mounting, alignment and testing, no vibration was observed in the drum. However, after keeping the drum rotating to test its endurance, a sudden failure occurred in the drum shaft. Figure 4-1 illustrates the drum and shaft as one-piece during testing and after shaft failure.

a) showing no vibration after mounting and alignment   b) after one hour of rotating test
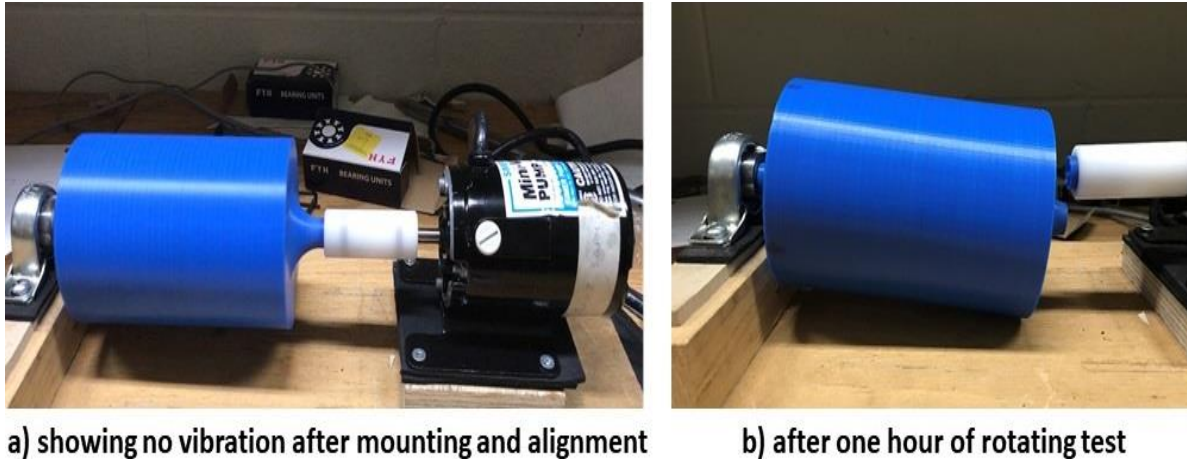
Figure 4-1: 3D printed rotating drum and shaft as one piece: a) showing no vibration after mounting and alignment, and b) after one hour of rotating test.

The shaft failed from the smallest diameter near coupling in a primary testing. To find the origin of the failure, the cross sections of the failed PLA shaft were investigated. Fatigue was observed at the cross sections. The cross sections are shown in Figure 4-2a, where the fracture zone is shown with red circles. Since no vibration was seen when the test started and the drum, the motor and bearing were fully aligned, the drum was isolated from the mounted bearing to investigate the origin of fatigue failure. It was observed that a twisting deformation had occurred at the interface of PLA shaft and the bearing; critically, at the point of bearing screw showing local melting (see Figure 4-2b).

PLA used in 3D printing has a melting point of about 160°C. However, the PLA glass transition point is $T_g = 65$°C. Therefore, it was concluded that the local heat generated inside bearing due to friction ultimately over passed the PLA T_g leading to gradual deformation of shaft. This shaft deformation provided an angular misalignment in the drum. This gradual increasing misalignment, ultimately, provided a dynamic load at the drum shaft on the other side of drum leading to fatigue failure.

a) the cross sections of 3D printed PLA shaft showing fatigue failure

b) shaft deformation inside the bearing
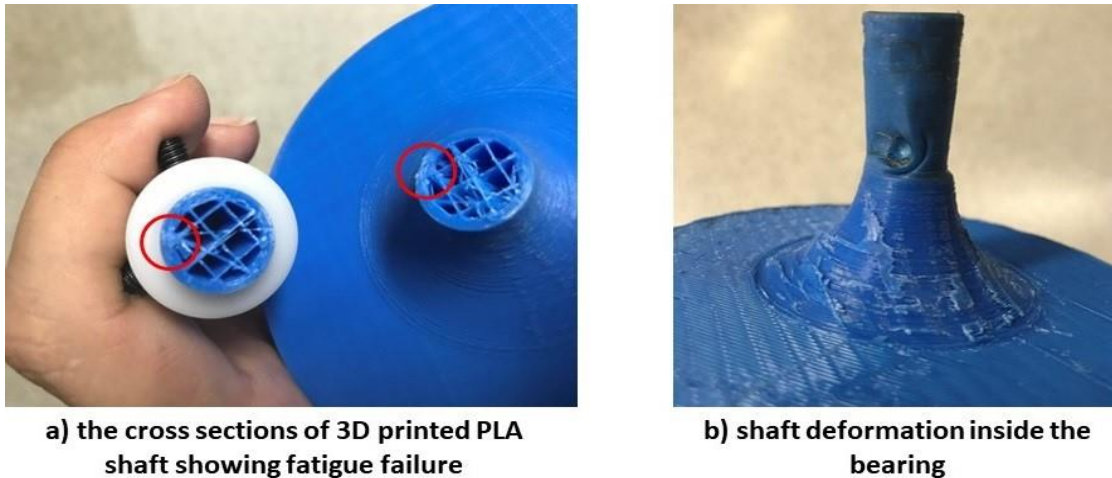
Figure 4-2: Fatigue failure and origin of fatigue: a) the cross sections of failed 3D printer PLA shaft: the red circle shows the fracture zone, and b) shaft deformation inside the bearing due to local high temperature.

Since the PLA $T_g = 65°C$ is small and heat generation in the bearing is inevitable, the drum was re-designed to use an aluminum shaft inside the 3D printed drum. The drum drawing is shown in Figure A- 4. The CAD design was converted from (.stl) to (.gcode) using MakerBot® (Desktop Version 3.10.1.1389). The drum was printed using MakerBot® Replicator™ 2 3D printer machine (see Figure 4-3-a). Based on the 3D printer manual, the nominal maximum height of the 3D printer is 6.1 inches (i.e. 15.49 cm). Therefore, the length of drum was reduced to 14.5 cm to use a support structure to obtain more accurate fabrication and avoid any malfunction.

An aluminum shaft of 3/4 inches outside diameter was used as drum shaft. Both tips were modified by using a lathe machine to have the outer diameters of 5/8 inches for mounting into the bearing and coupling. After mounting the drum and alignment, no vibration was observed (see Figure 4.3b).

In order to fix the drum on the aluminum shaft and avoid slipping, a shaft holder was designed by CAD (the drawing is shown in Figure A- 5). The shaft holder was 3D printed by MakerBot^r Replicator™ 2 3D printer machine using PLA filament. The shaft holder glued to the drum using Adhaero contact cement (All-Purpose Bonding, 30 mL tube) and fixed on the bearing inner ring using the bearing set-screw (see Figure 4-3c).
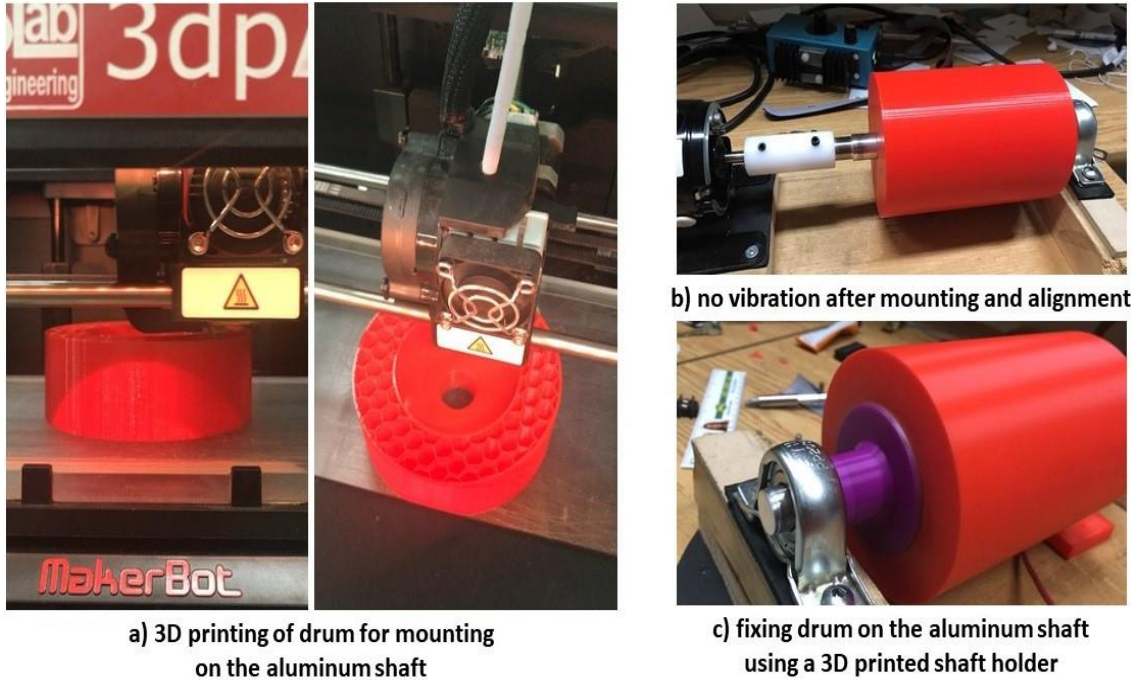
Figure 4-3: Rotating drum setup: a) 3D printing of drum for mounting on the aluminum shaft, b) no vibration after mounting and alignment, and c) fixing drum on the aluminum shaft using a 3D printed shaft holder.

The rotating drum was tested for several hours following by an inspection to check any loose components or malfunction. After the test and inspection, no malfunction or vibration appeared in the rotating drum.

4.1.2 Collector Connection

Drum made by PLA did not have a conductive surface. Fisherbrand^{TM} Aluminum Foil (Standard-Gauge Roll, 18μm thickness) was used as the collector conductive surface by wrapping around the drum. However, keeping the high voltage source connected to the wrapped aluminum foil was a challenge. The most feasible option was using the drum shaft as the connection way. Therefore, three alternatives to connect the voltage generator to the drum shaft were investigated and tested:

Through the Mounted Bearing

The connection between the drum shaft and the bearing outer ring was tested using Circuit-test DMR-1000 and showed a good conductivity. However, by increasing the speed of rotating drum, the conductivity started to reduce significantly. It was concluded that during the rotation, a thin

layer of lubrication oil covers the rolls inside bearing providing an electrical insulation between outer and inner rings of bearing. Therefore, this option was set aside.

Carbon Brush

Using a carbon brush to directly connect the voltage generator electrode to the shaft was investigated. First a carbon brush holder was designed by CAD. The drawing of the brush holder was shown in Figure A- 6. The CAD design was converted from (.stl) to (.gcode) using

MakerBot$^®$ (Desktop Version 3.10.1.1389). The brush holder was printed using MakerBot$^®$ Replicator^{TM} 2 3D printer machine and PLA filament.

A beveled edge carbon brush (25 mm $\times$ 8mm $\times$ 50 mm) was used with a helical compression spring. The brush wire was guided through the spring and the holder bottom hole to be accessible from the outside the holder (see Figure 4-4-a). The brush holder setup after assembling and mounting on the rotating drum was tested by a multimeter and the good conductivity between the brush wire and the drum shaft was confirmed (see Figure 4-4-b).

a) the position of carbon brush, spring and the accessibility of wire in 3D printed brush holder
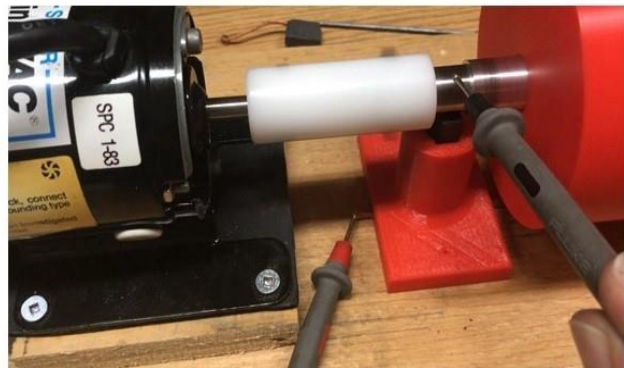
b) mounted carbon brush and testing with multimeter

Figure 4-4: Brush holder setup: a) the position of carbon brush, spring, and the accessibility of wire, and b) mounted carbon brush and testing with multimeter.

Through the Motor shaft

The last option was connecting the voltage generator electrode through the motor shaft. The motor shaft and the drum shaft were not connected electrically due to using non-metallic coupling. However, the connection was obtained by wiring the two set-screws on the coupling (see Figure 4-5).

Figure 4-5: Connection and testing of drum conductivity through the motor shaft.

It must be noted that this option can be only used if negative (ground) electrode of the high voltage source is connected to the drum during the electrospinning. Connecting the positive electrode of the high voltage source to the motor shell may develop serious damage to the motor system/electrospinning machine! The conductivity was tested by a multi-meter through the motor outer shell while the drum was rotating. Test result confirmed a good conductivity.

In a nutshell, the brush holder was the only confirmed and safe connecting alternative of the drum surface to the high voltage source. Furthermore, the motor shaft option is also can be used if and only if the drum is supposed to be connected to the negative (ground) electrode of high voltage source.

4.1.3 Other Setup Components

Motor Speed Control and Measurement

A motor speed control with a manual regulator was used to control the drum speed. To measure the drum speed and set to 1500 RPM, a digital stroboscope (GenRad 1546 STROBOTAC

DIGITAL STROBOSCOPE LOW 100-700 MED 600-4200 HIGH 3600-25000 PER MIN) was used. Figure 4-6 shows the drum speed measurement technique using the digital stroboscope.

Figure 4-6: An illustration of drum speed control using the stroboscope technique.

High Voltage Generator

A standard high voltage power supply for electrospinning (Spellman, NY, USA. CZE100R, 0-30kV. 0-300μA) was used to generate required voltage for electrospinning process.

Syringe Pump

A programmable syringe pump (New Era Pump Systems Inc. NE-1600 Six Channel) was used to control the flowrate and flow volume of PVDF solution.

4.1.4 Safety Considerations

Electrospinning process requires high voltage of 6-20 kV. Therefore, electrical shock hazard is inevitable, and the high voltage may be fatal. In this research, all the electrical components (motor, voltage generator and syringe pump) were grounded. A cuboid transparent chamber made by polycarbonate was used to isolate the collector from the lab environment. Every object at ground potential was placed away from the exposed high voltage points at minimum distance of 1 inch for every 7,500 volts (as it is recommended by Spellman manufacturer). Furthermore, the chamber door was equipped with safety interlocks i.e. the voltage generator was turned off automatically when the chamber door got open. A high voltage danger sign was also installed on the chamber door.

The assembled electrospinning machine is shown in Figure 4-7.

Figure 4-7: An illustration of assembled electrospinning machine.

4.2   **Electrospinning of PVDF**

In this section, the fabrication steps that were taken to achieve electrospun PVDF nanofibers are explained.

4.2.1   **Materials**

The PVDF powder with average molecular weight (M_w) of 534,000 g/mol was purchased from Sigma-Aldrich to prepare the PVDF solution.

Acetone (Certified ACS) with ≥99.5% assay (manufactured by Fisher Chemical BPA184, Product of USA) is used as PVDF powder solvent.

N, N-Dimethylformamide (DMF) with ≥99.8% assay (manufactured by Fisher Chemical, Product of Saudi Arabia) is used as the organic co-solvent of PVDF powder.

4.2.2   **PVDF Solution Preparation**

3.4 g of the PVDF powder was weighted with an analytical balance and poured carefully into a 50 mL glass jar. 7 mL of DMF and 16 mL of acetone were measured by a graduated cylinder and added into the glass jar. The mixture of PVDF powder, acetone and DMF was stirred manually with a spoon. Then, the jar lid was closed and sealed using a paraffin plastic film to avoid the

solution evaporation. The solution was stirred using hotplate and magnetic stirrer for 2 hours at 40℃ to obtain a homogeneous solution. The PVDF solvents ratio and stirring time and temperature were adapted from [16]. The stirring setup on the hot plate and magnetic stirring is shown in Figure 4-8.

Figure 4-8: PVDF solution preparation.

4.2.3 Electrospinning

The PVDF solution was filled into a 12 mL plastic syringe (inner diameter of ~15.5 mm) with a 18-gauge needle syringe. The filled syringe was loaded in the electrospinning syringe pump.

The distance between the collector was 10 cm for all the syringe orientations. The voltage generator was set to 12 kV. The positive electrode was connected to the syringe needle and the negative electrode (ground) was connected to the collector (i.e. the motor shell for the rotating collector and directly to the collector for the static collector).

The electrospinning process was done with two orientations of syringe pump (horizontal and vertical) to observe the effect of gravity on the electrospinning process. Also, two types of collector were used: static collector and rotating collector.

During the first electrospinning tests, needle clogging occurred -mainly due to the sharp shape of the needle tip. To avoid clogging, the needle tip was dulled using a grinder machine. The horizontal and vertical orientations of syringe pump, the static collector setup, and the syringe needle tip after grinding are shown in Figure 4-9.
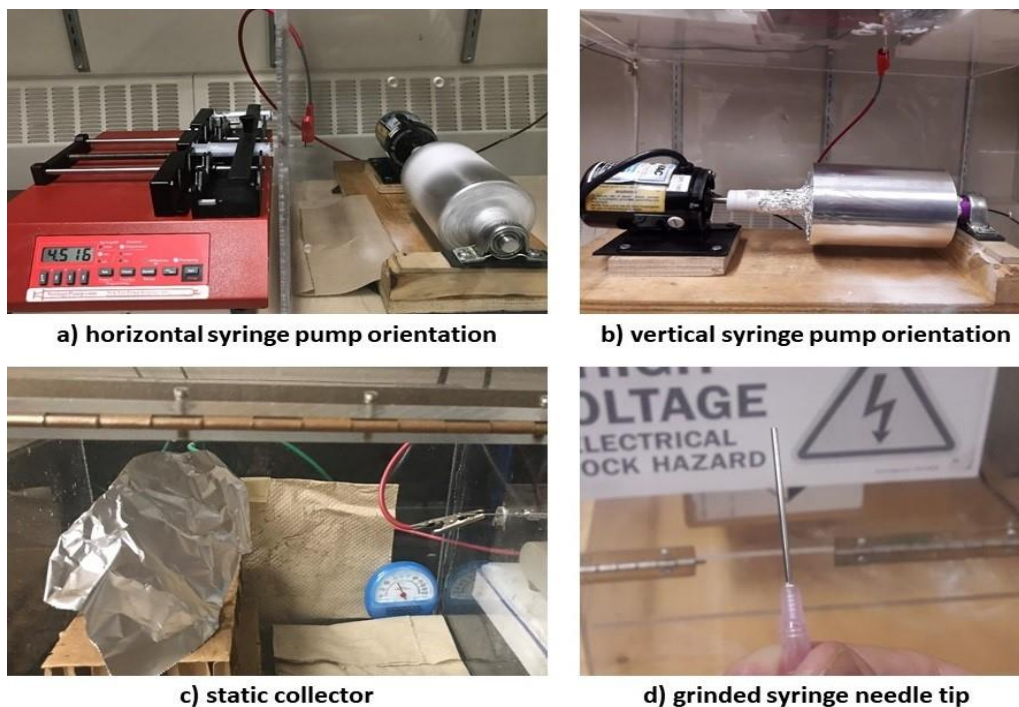
Figure 4-9: Electrospinning: a) horizontal syringe pump orientation, b) vertical syringe pump orientation, c) static collector, and d) grinded syringe needle.

4.3 MFC System

3D printing method was used mainly to fabricate PVDF-based MFC. The MFC was in two main pieces: main body and channel holder.

The main body and the channel holder were printed using MakerBot® Replicator™ 2 3D printer machine and PLA filament.

The main body and the channel holder components after fabrication is shown in Figure 4-10.
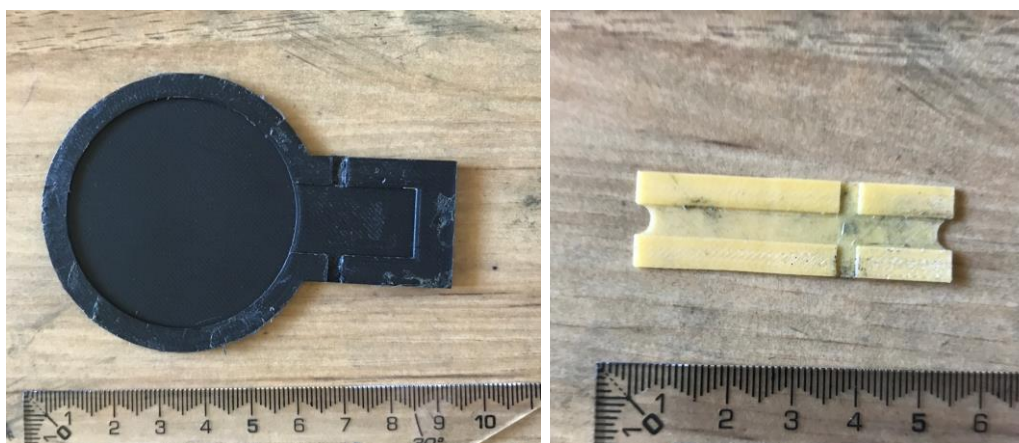
Figure 4-10: PVDF-based MFC components

5   EXPERIMENT

In this chapter, the experimental steps taken to investigate PVDF as a porous material in an MFC system are explained. First, the methods used to inspect the structure and to modify the hydrophilicity behavior of the fabricated porous PVDF are explained in Section 5.1 and Section 5.2 , respectively. Finally, the PVDF-based MFC experimental details are explained in Section 5.3.

5.1   Inspection of Electrospun PVDF Nanofibers

Scanning Electron Microscope (SEM) technique was used to inspect the electrospun PVDF nanofibers. A JEOL (JSM-6010LV series, up to resolution of 4.0 nm at accelerating voltage of 30 kV in low vacuum mode) is used to capture the images. It is common that polymer-based nanofibers are gold coated before capturing SEM images to achieve the highest scanning resolution and avoid damaging the fibers during electron scanning; however, in this research, all the images were captured without gold coating and the resolution was acceptable. Since the fibers were not gold coated, the low vacuum mode setting was used in SEM. The best image resolution was achieved in vacuum pressure of 40 Pa and accelerating voltage of 12 kV.

For loading the specimens into the SEM, to avoid any damage to the nanofibers, each specimen was carefully cut by a scissor and removed by a thumb forceps from the aluminum surface of collector. A double side conductive tape was used to fix each specimen on the specimen holder. Figure 5-1 shows the Joel SEM, the nanofibers after carefully removing from the collector, nanofibers loaded on specimen holder with conductive tape, and specimen holder being loaded into the SEM.

Figure 5-1: SEM technique: a) Joel SEM, b)the nanofibers after carefully removed from the collector, c) nanofibers loaded on specimen holder with conductive tape, and d) specimen holder being loaded into the SEM.

5.2   PVDF Nanofibers Surface Treatment

The PVDF nanofibers achieved by the electrospinning process has a high hydrophobic surface feature. Based on the Lucas-Washburn's equation (Equation 3-1), since the PVDF nanofibers contact angle is greater than 90 degree and the cos θ is in the numerator of the equation, the fuel cannot be travel through the PVDF nanofibers channel by capillary action. Therefore, a surface hydrophilic modification of PVDF (explained in Section 2.10) is required to reduce the contact angle and improve the PVDF nanofibers hydrophilicity. Oxygen/argon plasma treatment method is selected to enhance the hydrophilicity due to its feasibility, accessibility.

5.2.1   Oxygen/Argon Plasma Treatment

A Reactive Ion Etcher (RIE) system was used to perform the oxygen plasma treatment on the electrospun PVDF nanofibers. The model of the RIE system that was used is RIEUSAS-RIE-72109-NP1, 220 V, 1 φ, 60 Hz, 15A (manufactured by TORR International, INC.). Based on [99],

52

for oxygen plasma treatment of 120 s and O_2 flow rate of 120 sccm, a power of greater than 360 W is required to obtain hydrophilic PVDF nanofibers. However, although the present plasma device nominal power is 600 W, due to technical issue, the maximum power that could be used was 50 W. Therefore, the treatment time was increased to compensate the low power that was used.

To investigate the effect of time increment on hydrophilicity, the contact angle for different treatment times was measured and compared. Figure 5-2 shows the apparatus of plasma treatment device as well as the oxygen and argon gas flow rate, power, and other plasma device settings.

a) plasma treatment device   b) plasma treatment device settings
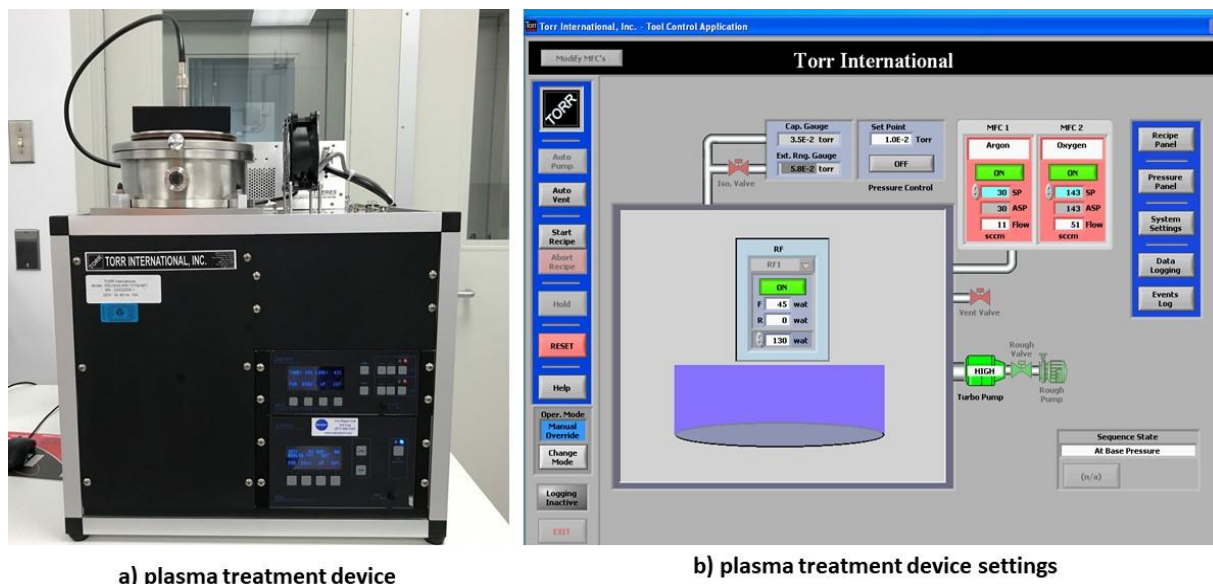
Figure 5-2: Plasma surface treatment: a) device apparatus, and b) plasma treatment device settings.

In addition to investigation of treatment time effects on the electrospun PVDF nanofibers hydrophilicity, plasma treatment was also performed to investigate the possibility of selective treatment.

Figure 5-3 illustrates the plasma machine chamber where Figure 5-3-a shows the selective treatment of PVDF nanofibers: on the top, the electrospun PVDF nanofibers were covered with aluminum foil and only one rectangular shape of the fibers were exposed to the plasma, and at the bottom, the PVDF nanofibers were covered with glass slides. Figure 5-3-b shows the non-selective plasma treatment method.
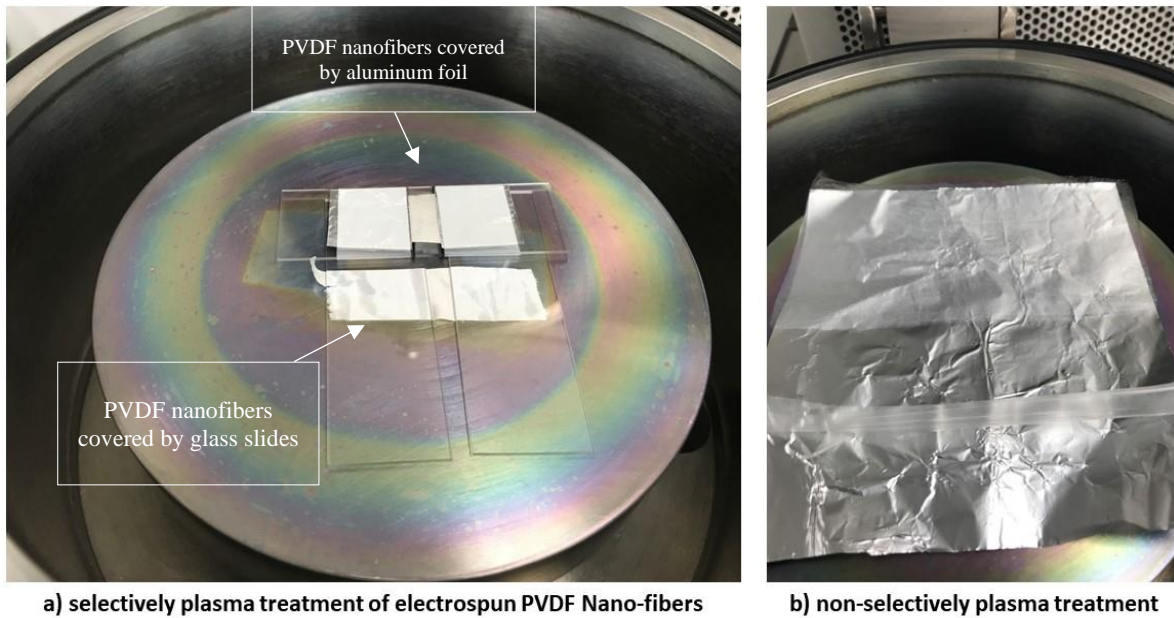
Figure 5-3: Selective and non-selective plasma treatment of electrospun PVDF nanofibers: a) selective plasma treatment with aluminum foil and glass slides, and b) non-selective plasma treatment.

5.2.2 Contact Angle Measurement

To investigate the effects of plasma surface treatment on the hydrophilicity feature, the contact angle of water droplet on the PVDF nanofibers was observed and measured for each treatment that was performed. Water was used to test the channel substrate hydrophilicity feature due to two reasons: 1. capillary action of water is similar to that of hydrogen peroxide that was used in this research as fuel to test the electrochemical behavior of PVDF in an MFC system, 2. water and biological fluids (e.g. blood) share a similar capillary action.

To measure contact angle, a manual microscope (ZEISS SteREO Discovery.V8) was set in horizontal orientation. Two white lights used to bright the PVDF nanofibers surface and water droplet from right and left sides for better clarification of water and PVDF contact boundary. The focusing and magnification of microscope were performed manually, but the microscope was connected to a computer for the digital image recording and contact angle measurement. Figure 5-4 illustrates the manual microscope setting for measuring contact angle of water droplet on the PVDF nanofibers to investigate its hydrophobicity and hydrophilicity features.
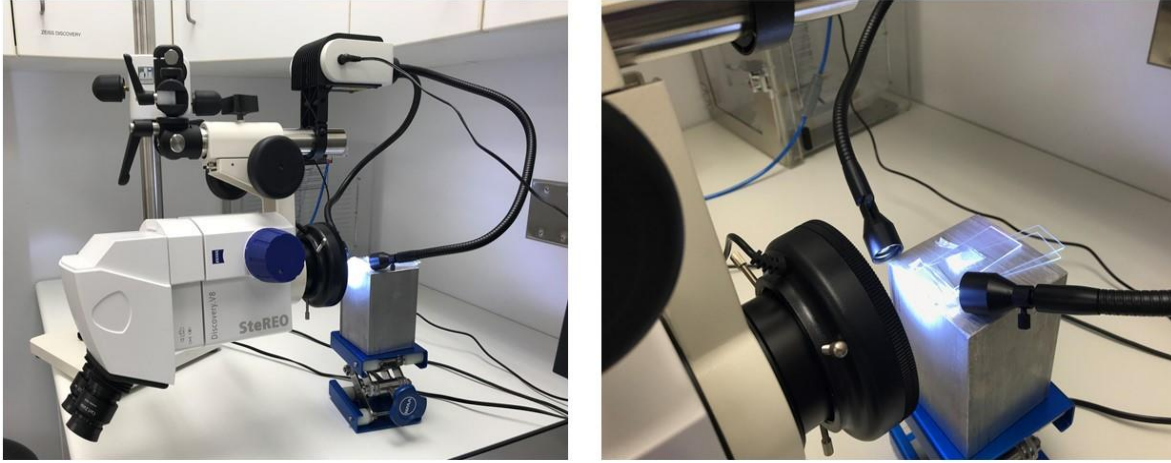
Figure 5-4: Contact angle measurement of water droplet on electrospun PVDF nanofibers to investigate hydrophilicity and hydrophobicity surface features.

5.3 PVDF-Based MFC Experiments

In this section, the fuel preparation, cathode and anode catalysts preparation, coating electrodes with the respective catalysts, and the electrochemical experiments that were done to obtain the power density and current density of PVDF-based MFC are explained.

The electrochemical experiment was conducted in acidic conditions by introducing hydrochloric acid (HCl) to hydrogen peroxide (H_2O_2). The reduction reaction in cathode electrode, the oxidation reaction in anode electrode, and the overall redox reaction are shown in Equation 5-1, Equation 5-2, and Equation 5-3 respectively [100].

$$Cathode(Reduction): H_2O_{2\,(aq)} + 2H^+_{(aq)} + 2e^- \rightarrow 2H_2O_{(l)} \qquad (5-1)$$

$$Anode(Oxidation): H_2O_{2\,(aq)} \rightarrow O_{2\,(g)} + 2H^+_{(aq)} + 2e^- \qquad (5-2)$$

$$Overall: 2H_2O_{2\,(aq)} \rightarrow O_{2\,(g)} + 2H_2O_{(l)} \qquad (5-3)$$
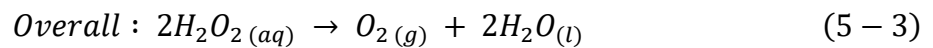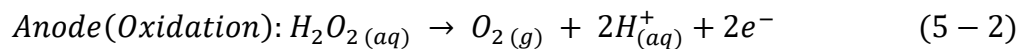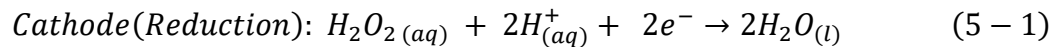
5.3.1 Fuel Preparation

Hydrogen peroxide (30%, MW 34.014 g/mol, density of 1.110 g/cm^3, manufactured by Fisher Chemical, USA) was used as the fuel.

Hydrochloric acid (certified ACS Plus, 36.5 to 38.0%, ~12 M, Fisher Chemical, Canada) was used to introduce acidic condition to the fuel. HCl diluted by deionized water to obtain 0.1 M required for fuel preparation.

To obtain 0.5 M hydrogen peroxide (H_2O_2) in 0.1 M HCl (based on [16]), the following steps were taken:

First, the molarity (M) of H_2O_2 with 30% concentration, molar weight of 34.014 g/mol, and density of 1.110 g/cm^3 was calculated as 9.79 M (mol/L) in Equation D-1.

Second, to obtain 0.5 M hydrogen peroxide from 9.79 M hydrogen peroxide, the solution dilution was calculated based on obtaining 10 mL volume of final diluted solution of 0.5 M hydrogen peroxide in Equation D-2.

Based on Equation D-2, to obtain 10 mL of 0.5 M hydrogen peroxide, 0.5 mL of 9.79 M of hydrogen peroxide was diluted in 9.5 mL of 0.1 M HCl. Therefore, the final solution was 10 mL of 0.5 M hydrogen peroxide in ~0.1 M (0.095 M) HCl. The fuel was prepared at the time of the electrochemical test of PVDF-based MFC.

5.3.2 Cathode Catalyst Preparation: PB on Carbon Support

Prussian Blue (PB) was used as cathode catalyst for decomposition hydrogen peroxide for reduction reaction. The PB was prepared based on [101] and [102]:

First, the required amount of potassium ferricyanide (III) [$K_3Fe(CN)_6$] powder (MW: 329.24, purchased from Sigma-Aldrich) was dissolved in 20 mL of 0.1 M HCl to form 0.5 M $K_3Fe(CN)_6$ (See Figure 5-5).

Figure 5-5: Preparation of 0.5 M K$_3$Fe(CN)$_6$ in 0.1 M HCl.

56

The amount of $K_3Fe(CN)_6$ powder was calculated as 3.29 gr in Equation D-3.

Second, 1.62 gr FeCl$_3$ (see Equation D-4) was added into 20 mL of 0.1 M HCl to form 20 mL of 0.5 M FeCl$_3$ in 0.1 M HCl (See Figure 5-6).

Figure 5-6: : Preparation of 0.5 M FeCl3 in 0.1 M HCl.

Third, 2 grams of Vulcan XC-72R carbon powder (purchased from FuelCellStore) was suspended and agitated in 20 mL of 0.5 M $K_3Fe(CN)_6$ in 0.1 M HCl (prepared in the first step) following by adding drop wise of 20 mL of 0.5 M *FeCl$_3$* in 0.1 M HCl (prepared in the second step). The result solution was stirred for 1 h using magnetic stirrer (see Figure 5-7).

Figure 5-7: Suspension and agitation of carbon powder in 0.5 M K$_3$Fe(CN)$_6$ in 0.1 M HCl and 0.5 M FeCl$_3$ in 0.1 M HCl solutions.

Fourth, the resultant mixture was washed by 0.1 M HCl by filtration method until the HCl dropping from the filter became colorless. The filtration process is shown in Figure 5-8.

The achieved powder was dried in an oven for 2h at 100°C. The PB on carbon support was stored in a sealed bottle at room temperature.

Figure 5-8: PB supported by carbon powder filtration process.

5.3.3 Electrodes Preparation

Cathode Electrode

Toray Carbon Paper (TGP-H-090, 5% wet proofed, thickness 280 μm, purchased from Fuel Cell Earth) was used as the electrode backing material. It was cut manually in the size of 20 mm $\times$ 2 mm to form the electrode.

In order to coat PB on carbon support prepared in Subsection 5.3.2 on the Toray carbon paper, Nafion$^{\circledR}$ D-520 dispersion (5% w/w in water and 1-propanol, purchased from Alfa Aesar) was used to make the cathode catalyst slurry. Nafion$^{\circledR}$ is used to enhance the proton conductivity in cathode electrode [103]. The cathode ink was manually coated on one side of the Toray Carbon paper where was supposed to be contacted with the channel substrate. The cathode electrode after coating was left to dry in room temperature.

Anode Electrode

Carbon cloth electrode (0.3 mg/cm^2 40% pt, purchased by Fuel Cell Earth) is used as the anode electrode. It was cut manually in the size of 20 mm $\times$ 2 mm to form the anode electrode.

5.3.4 Electrochemical Experiments

Whatman cellulose chromatography paper (1 Chr sheet, purchased by Sigma-Aldrich) was cut into the circular shapes with the diameter of 5 cm by CO_2 Epilog Laser Fusion 75-watt machine to form the absorbent pad.

To test PVDF as channel substrate, Durapore PVDF membrane (0.22 µm pore size, diameter of 47 mm, Merck Millipore Ltd, Ireland) was purchased. The circular PVDF membrane was manually cut to form rectangular PVDF channel substrate (4 mm × 45 mm).

The PVDF-based MFC was assembled while the electrodes are placed on the opposite sides of the channel substrate with approximately 1 mm distance from the edges. Therefore, rectangular shape of 3 mm × 2 mm or an area of 0.06 cm^2 was in contact with the channel substrate. The MFC channel and electrodes were covered using an adhesive tape (Scotch® 468MP Adhesive Transfer Tape) to avoid contamination, evaporation of fuel, and keeping the electrodes surfaces in contact with the channel substrate during the experiments. Figure 5-9 shows the MFC after assembling.
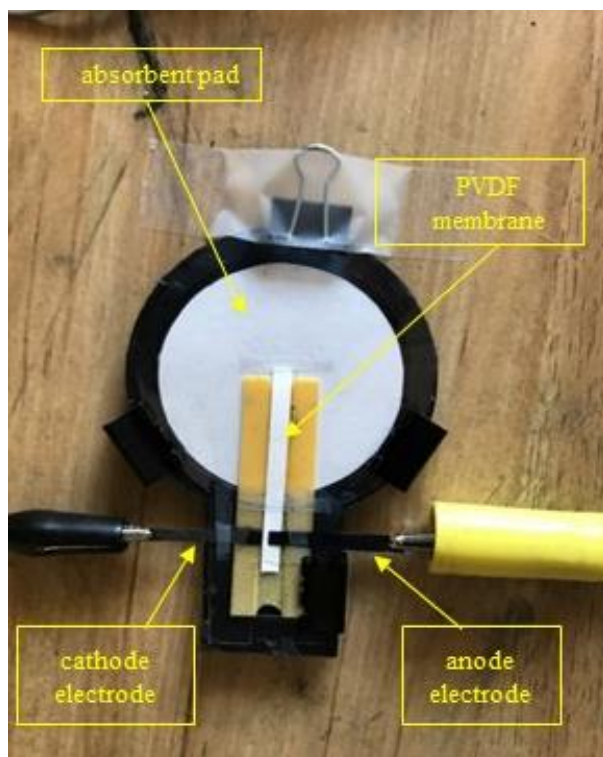
Figure 5-9: PVDF-based MFC after assembling.

The MFC was tested by injecting the fuel solution using a syringe near the channel inlet to begin the electrochemical reaction.

A circuit-test multimeter (DMR-1000) was used to test the fuel cell performance. Before starting the experiment, the current and voltage measurements were set to zero. After injection, the fuel was absorbed by the channel substrate and moved towards the absorbent pad. Once the fuel reached the electrodes, the current started to increase until it reached ~329 μA (maximum current). The voltage also measured ~155 mV using the circuit test, i.e. Open Circuit Potential (OCP) of the cell. Figure 5-10 shows the MFC during the test showing the maximum current and voltage outputs.

a) MFC test showing voltage of: 155 mV   b) MFC test showing current of: 0.329 mA

Figure 5-10: MFC electrochemical test results: a) showing voltage of 155 mV, and b) showing current of 0.329 mA.

To acquire more reliable voltage measurements for different loads in order to obtain the polarization performance (potential-current curve) and the power curve of the PVDF-based MFC, the test was repeated by recording the cell potential in an electronic circuit using a resistor box (Heathkit DR-1 Decade Resistance) and a portable analog circuit design kit (Digilent Analog Discovery). The circuit is shown in Figure 5-11.
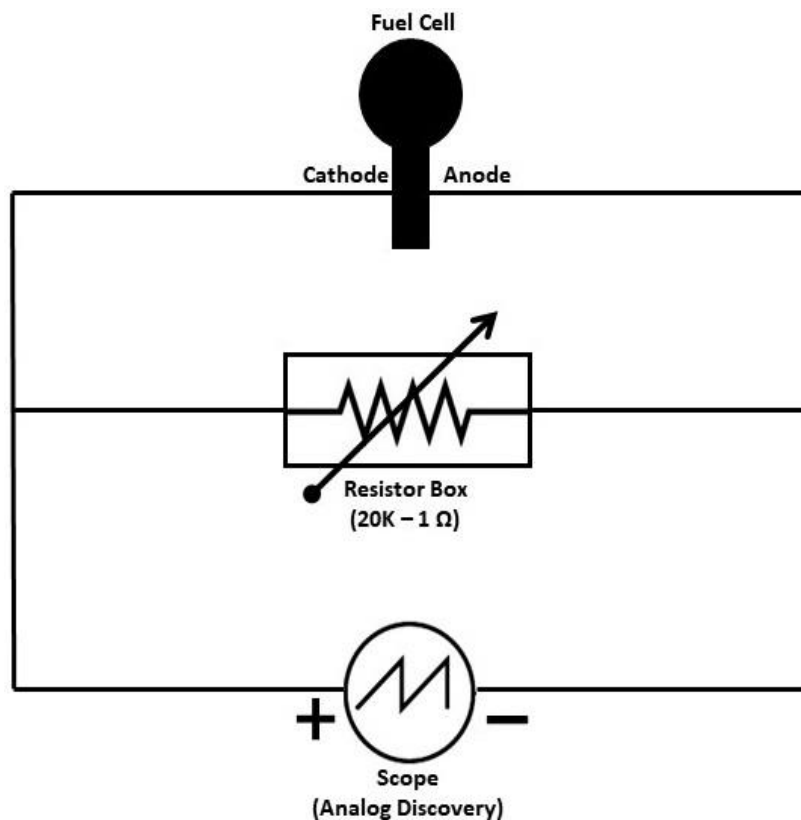
Figure 5-11: The circuit used to test PVDF-based MFC.

The real-time cell potential data were recorded using the scope environment of WaveForms software (V. 3.14, Digilent). Before the injection of the fuel, the resistor box was detached from the circuit (no resistor was connected). The initial voltage before injection of fuel was fluctuating between 2.5 mV and 3.5 mV. Once the fuel reached the electrodes, the voltage, as observed on the digital oscilloscope, dramatically jumped, and became stable after ~10 seconds. At this stabilization point, the voltage was recorded as 164.8 mV which was considered as the cell OCP. Figure 5-12 shows a dynamic profile of the cell potential from the moment fuel reached to the electrodes until it became stabled on ~164.8mV. The highest voltage recorded (the peak of the graph in Figure 5-12) was 226.8 mV.
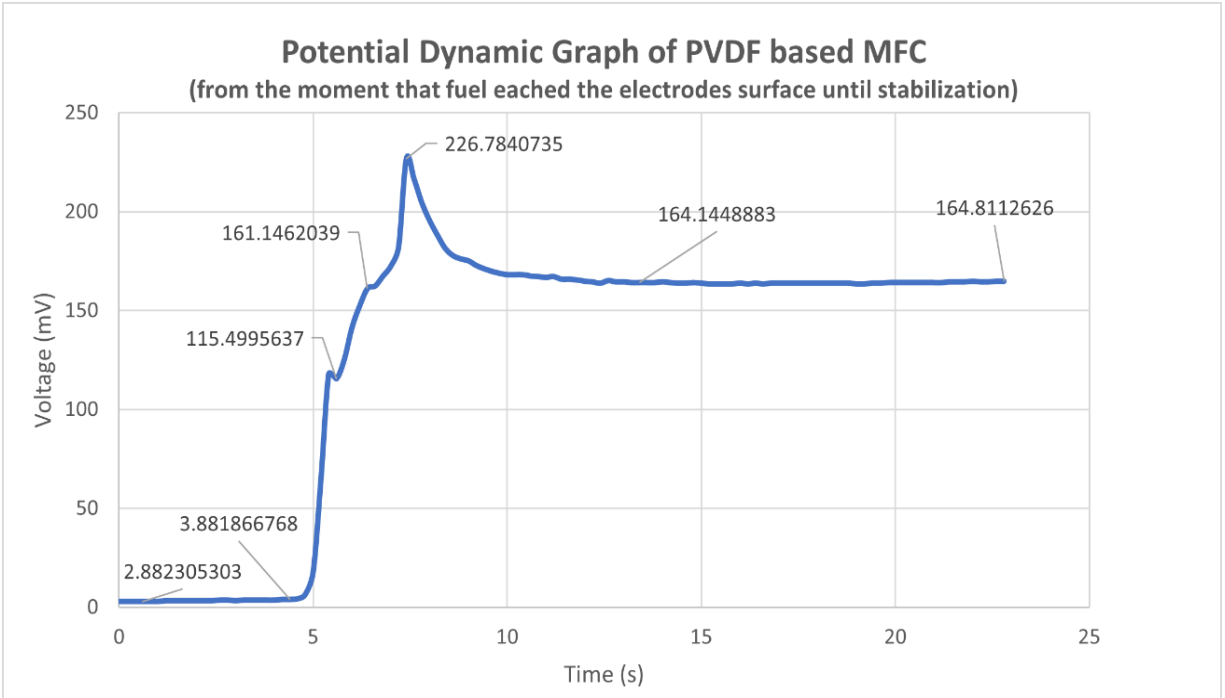
Figure 5-12:Potential dynamic graph of PVDF-based MFC from the moment that fuel reached the electrodes surface until stabilization. The OCP of the cell was recorded 164.8 mV.

After stabilization of the cell potential, the spring box was connected to the circuit. To obtain an accurate potential-current dynamic profile, the cell voltage was recorded for 23 different resistors (20 kΩ, 10 kΩ, 8 kΩ, 6 kΩ, 4 kΩ, 2 kΩ, 1 kΩ, 800 Ω, 600 Ω, 400 Ω, 200 Ω, 100 Ω, 80 Ω, 60 Ω, 40 Ω, 20 Ω, 10 Ω, 8 Ω, 6 Ω, 4 Ω, 2 Ω, 1 Ω, 0 Ω) while a waiting period of 10-20 seconds was applied after each resistor to allow for cell voltage stabilization. For resistors smaller than 10 Ω, the voltage dropped to 3.5 mV. Voltages 2.5 mV - 3.5 mV were initially recorded before fuel injection. Therefore, for resistors smaller than 10 Ω, the recorded voltage values were considered as system error/noise and assumed as zero in calculations. The data were exported from the WaveForms software and imported into Microsoft Excel for further analysis.

The cell current for each point was calculated using Ohm's law i.e. $I = V \times R$.

The electrode area attached to the channel was rectangular with the dimensions of 3 mm × 2 mm (area 0.06 cm^2). Therefore, the current density was calculated by dividing current by the electrode area (see Equation D-5). The power density was calculated using electric power definition i.e. $P = V \times I$ (see Equation D-6).

6   RESULTS AND DISCUSSION

In this chapter, first, the results of the SEM images of the fabricated porous PVDF using different electrospinning setups and parameters are discussed in Section 6.1. Then, the results of the hydrophilicity/hydrophobicity features of electrospun PVDF nanofibers modified/unmodified by the plasma treatment method are discussed in Section 6.2. Finally, the electrochemical experimental results of the PVDF-based MFC are discussed in Section 6.3.

6.1   SEM Inspection of Electrospun PVDF Nanofibers

In this section, the SEM images that were taken are presented and analyzed to evaluate the electrospun PVDF nanofibers diameter, beads, homogeneity and alignment for two types of collectors (static and dynamic/rotating) for two different syringe pump orientations (horizontal and vertical) for different flow-rates of PVDF solution. An open source Java image processing software, ImageJ (V. 1.53a) [104], was used to measure the nanofibers diameters. For each SEM images, 20 fibers diameters were randomly measured, and the average diameter was recorded.

In horizontal orientation, the distance between the needle and collector was set to 15 cm initially; however, the fibers failed to reach the collector (especially in flow rate of 5 μl/min) and they were collected at the bottom surface of the electrospinning chamber. After decreasing the distance to 10 cm, the fibers were successfully collected on the collector. This phenomenon occurred due to the gravitational effects on the Taylor cone. Figure 6-1-a shows successfully fibers collection in the distance of 10 cm and Figure 6-1-b shows how fibers failed to reach the collector in the needle and collector distance of 15cm.

Furthermore, in horizontal orientation, during electrospinning needle clogging occurred frequently with a higher frequency in 5 μl/min flow rate. Figure 6-1-c illustrates the needle clogging in electrospinning process in horizontal orientation. Needle unclogging process was performed by turning off the voltage generator, unclogging the needle, and turning back the voltage generator.
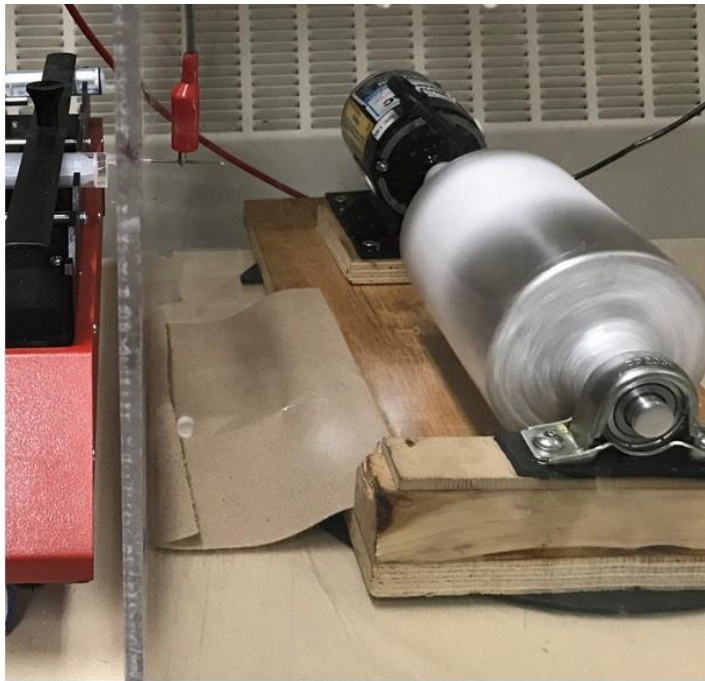
a) needle to collector distance of 10 cm

b) fibers were not collected on the collector in the distance of 15 cm
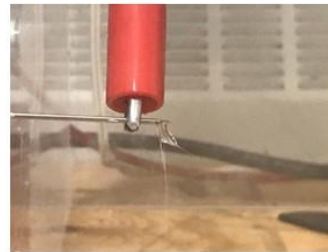
c) needle clogging in horizontal electrospinning

Figure 6-1: Electrospinning in horizontal orientation: a) the needle and collector distance of 10 cm: the fibers were successfully collected on the collector surface, b) the needle and collector distance of 15 cm: the fibers failed to reach the collector due to gravitational effects on Taylor cone, and c) frequently needle clogging during electrospinning in horizontal orientation.

6.1.1 On the Static Collector: Homogeneity, Beads Formation, Alignment, and Fibers Size

Electrospun nanofibers were fabricated with the flow rates of 5 μl/min, 25 μl/min, and 50 μl/min on the static collector in vertical and horizontal orientations of syringe pump.

Figure 6-2 and Figure 6-3 show the SEM images of the six different electrospinning settings with different zoom sizes.
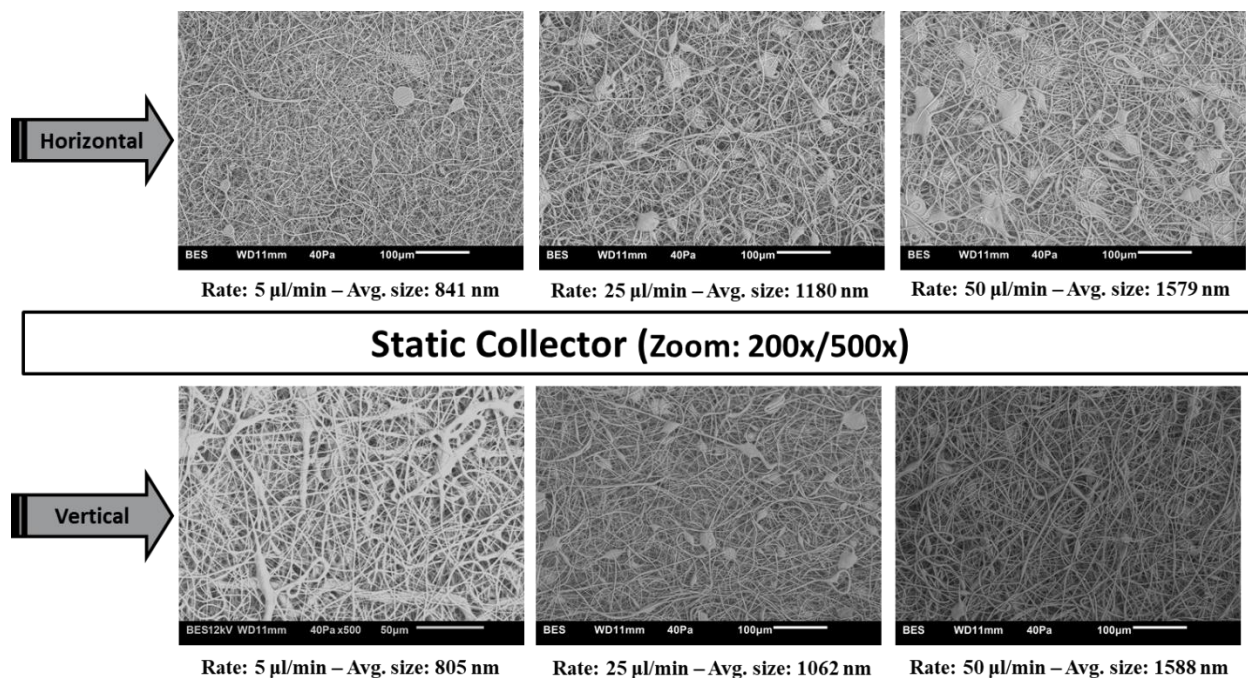
Figure 6-2: SEM images of PVDF nanofibers on the static collector: homogeneity, alignment, and bead formation.
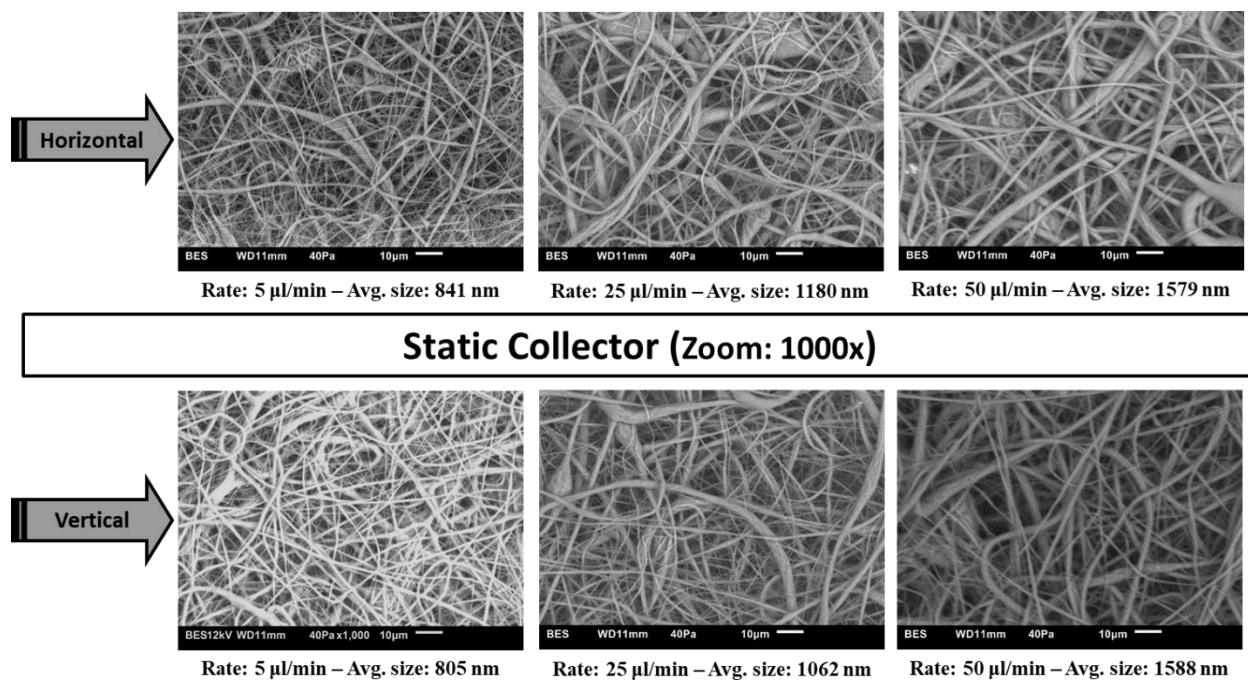
Figure 6-3: SEM images of PVDF nanofibers on the static collector: fibers size.

As it is shown in Figure 6-2 and Figure 6-3, non-aligned PVDF nanofibers were achieved by the static collector. In both horizontal and vertical orientations, the pore sizes and the fiber sizes

were increased by increasing the flow rate. This phenomenon is in full agreement with what was discussed in Effects of Solution Parameters, i.e. increasing flow rate leads to increase the fibers diameter and pore sizes.

In horizontal orientation, the flow rate increment led to formation of beads and achievement of less homogenous fibers. On the other hand, by increasing the flow rate in the vertical orientation, the homogeneity of fibers was increased, and beads formation was decreased significantly.

6.1.2 On the Dynamic Collector: Homogeneity, Beads Formation, Alignment, and Fibers Size

Electrospun nanofibers were fabricated with the flow rates of 5 μl/min, 25 μl/min, and 50 μl/min on the dynamic collector in vertical and horizontal orientations of syringe pump. Figure 6-4 and Figure 6-5 show the SEM images of the six different electrospinning settings with different zoom sizes.
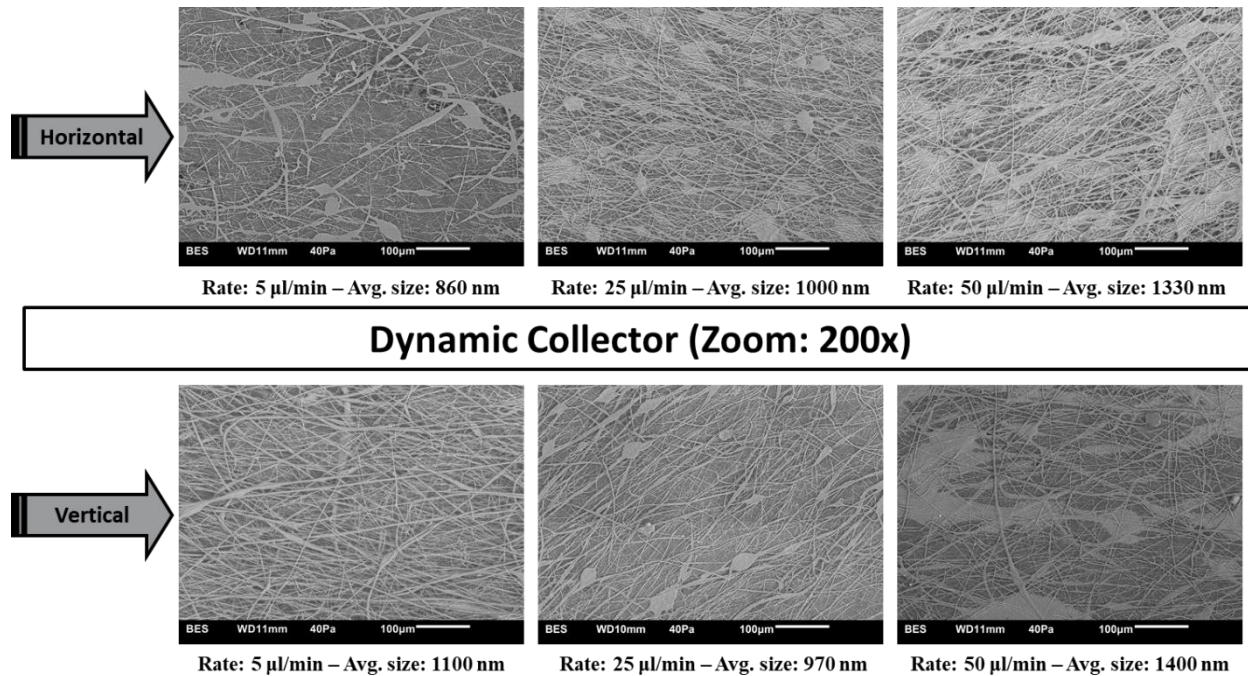
Figure 6-4: SEM images of PVDF nanofibers on the dynamic collector: homogeneity, alignment, and bead formation.
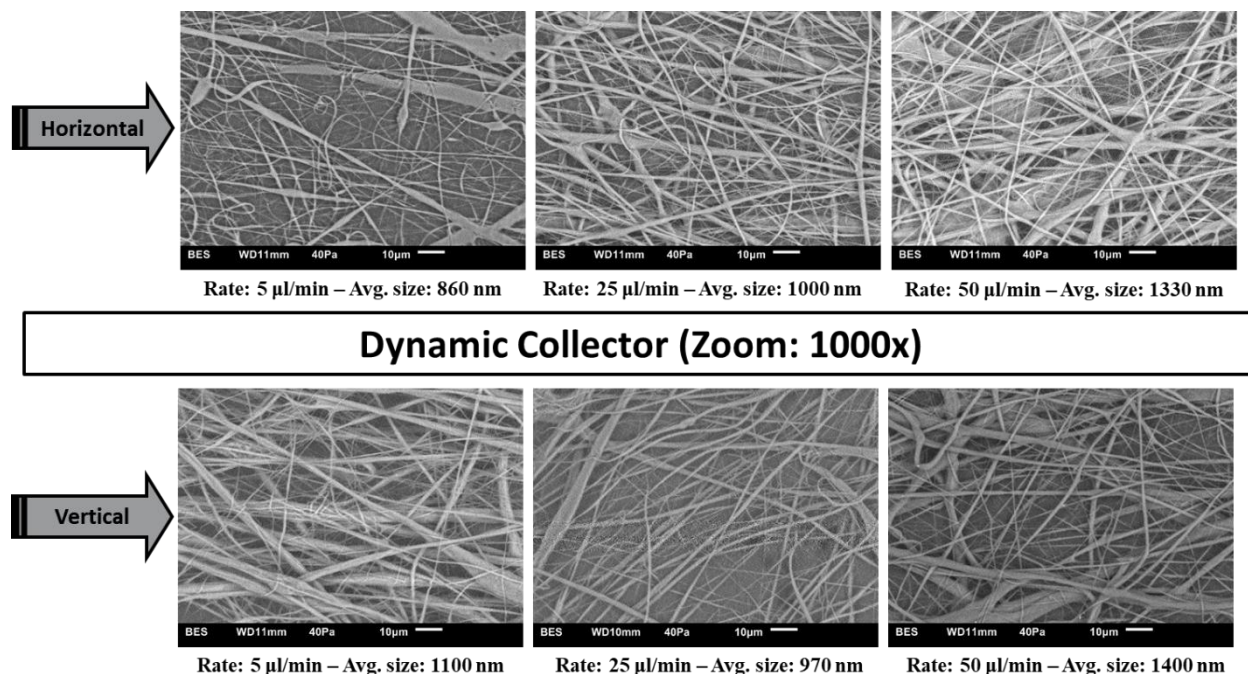
Figure 6-5: SEM images of PVDF nanofibers on the dynamic collector: fibers size.

As it is shown Figure 6-4 and Figure 6-5, the fibers alignment was successfully achieved by the rotating drum collector. In both horizontal and vertical orientations, pore sizes and the fiber sizes increased by increasing the flow rate. This phenomenon is in full agreement with what was discussed in Effects of Solution Parameters, i.e. increasing flow rate leads to increase the fibers diameter and pore sizes. Also, by increasing the flow rate, the bead sizes increased, and homogeneity decreased.

6.2   Hydrophilicity and Hydrophobicity Characterization of Electrospun PVDF Nanofibers

The hydrophilicity and hydrophobicity characterization of electrospun PVDF nanofibers were analyzed using the contact angle method. The angles were approximated by an open source Java image processing software, ImageJ (V. 1.53a) [104] using Drop Shape Analysis- LBADSA (Low-Bond Axisymmetric Drop Shape Analysis) plugin [105].

Figure 6-6 illustrates the actual drop shape on the electrospun PVDF nanofibers and the method of contact angle measurement using ImageJ software. The contact angle was approximated 125°. This agrees with the high hydrophobicity of PVDF reported in the literature.
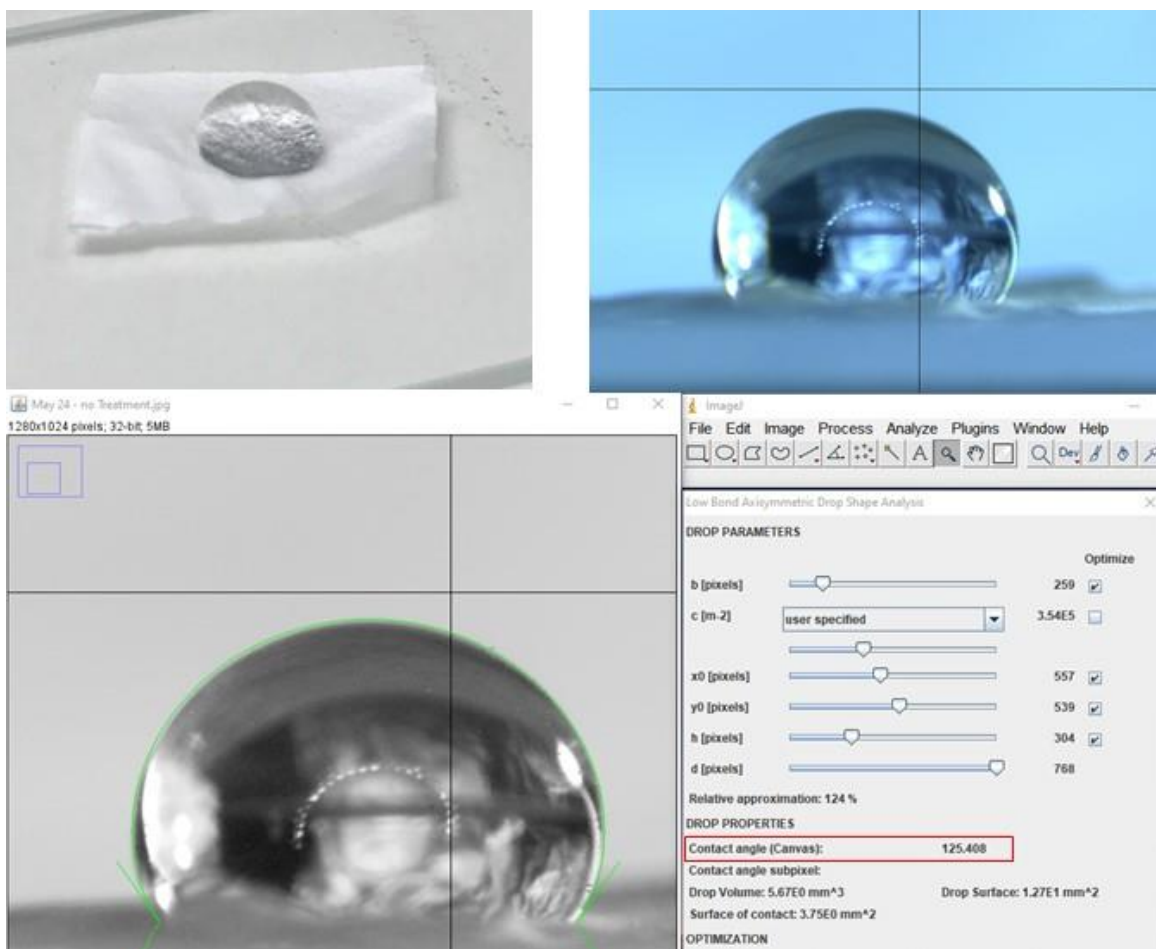
Figure 6-6: Electrospun PVDF nanofibers contact angle measurement showing high hydrophobicity with contact angle of 125°.

6.2.1 Non-selective Plasma Treatment

Oxygen/argon plasma treatment was performed to make the electrospun PVDF nanofibers super-hydrophilic. Based on [99], 2 minutes of plasma treatment at 360 W power is required to obtain super hydrophilic PVDF nanofibers; however, since the available plasma machine could only reach to the maximum power of 50 W, plasma treatment time was increased to compensate the lower used power.

To find the required time to obtain super hydrophilic PVDF nanofibers, plasma treatment was performed for 2 minutes, 12 minutes, 15 minutes, 20 minutes, and 30 minutes.

At 2 minutes of treatment, no change in hydrophobicity of PVDF nanofibers was observed. This phenomenon was expected as a significant lower power was used.

Contact angle at 12 minutes reached to 17°. Figure 6-7 shows the water droplet interaction with PVDF nanofibers after 12 minutes and Figure C- 1 shows the image processing used to approximate the contact angle.

At 15 minutes, 20 minutes and 30 minutes of plasma treatment, the water droplets were absorbed completely into the substrate that the contact angle could not be measured. Therefore, 15 minutes of plasma treatment was confirmed for the required treatment time for obtaining super hydrophilic electrospun PVDF nanofibers.

Treatment time: 12 minutes   Contact angle= 17
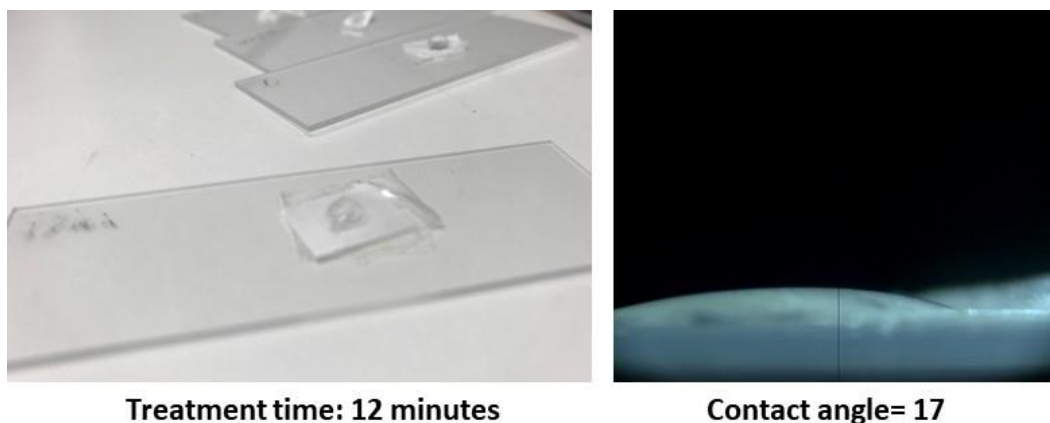
Figure 6-7: Electrospun PVDF nanofibers after 12 minutes of plasma treatment showing contact angle of 17°.

6.2.2   Selective Plasma Treatment

Three surface-selective plasma treatments were performed to evaluate the possibility of selectively enhancing the hydrophilicity of PVDF nanofibers.

Selective Treatment Using PMMA Glass

First, a PMMA glass with thickness of 2 mm with a rectangular slot in the middle was placed on the PVDF nanofibers and treated for 15 minutes (see Figure 6-8-a). It was expected that the hydrophobicity of the area underneath of the PMMA cover does not change and the rectangular area that is exposed to the plasma adsorbs the water droplet i.e. becomes super hydrophilic. After treatment, as expected, the contact angle underneath of the PMMA cover was measured 124°; however, the water droplet was not adsorbed by the rectangular area that was exposed to the plasma. The contact angle of the rectangular shape area was measured 82 °. The contact angle of 82°shows that the rectangular area was successfully treated by plasma; but, not enough to make the fibers super hydrophilic.

Figure 6-8-c and Figure 6-8-d shows the contact angle of the covered and exposed areas respectively. Figure C- 2 and Figure C- 3 show the image processing method used to approximate the contact angles for underneath of the PMMA cover and exposed area respectively.
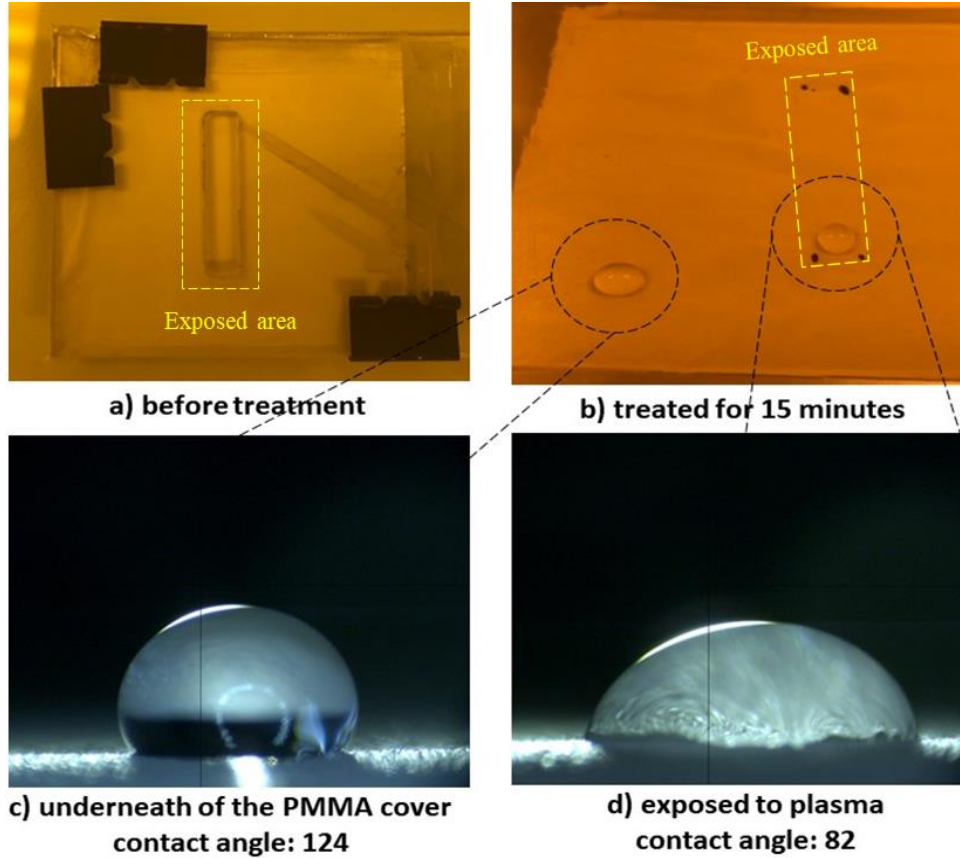
Figure 6-8: Selective plasma treatment using PMMA glass: a) before treatment, b) after 15 minutes of plasma treatment, c) water droplet on the area covered by PMMA showing contact angle of 125°, and d) water droplet on exposed area showing contact angle of 82°.

It was hypothesized that the 2 mm thickness of PMMA was too high that blocked or reduced the energy of the oxygen/argon molecules attacking the surface during the plasma treatment. Therefore, to experiment the effect of the cover thickness on selective plasma treatment, the previous experiment was repeated using two different thinner covers: glass slide and aluminum foil.

Selective Treatment Using Glass Slide

Microscope glass slide (thickness 1mm) was used for selective plasma treatment of the PVDF nanofibers substrate. Figure 6-9-a shows how glass slides were placed in the plasma chamber. Figure 6-9-b shows the substrate after plasma treatment for 15 minutes. A water droplet was

dropped on the substrate surface to investigate hydrophilicity. The exposed area became super hydrophilic successfully; however, after several seconds, the water was started being absorbed smoothly into the rectangular area surroundings that were covered by the glass slides. Figure 6-9-c shows the substrate contact angle test. Despite of water absorption into the unexposed region, the effect of cover thickness in selective plasma treatment was confirmed.

It is believed that two reasons made the areas covered by the glass slides hydrophilic: firstly, the glass slides did not fully envelope the substrate (the same as how PMMA enveloped the substrate in the first selective plasma treatment experiment), secondly, the uneven surface of the substrate and its porous structure allowed accelerated argon/oxygen to penetrate underneath of glass slides. This phenomenon can be clearly observed in Figure 6-9-c that the substrate absorbed the water droplet only around edges of the regions where glass slides were covered. Two small water droplets were dropped on the middle of the covered areas (see Figure 6-9-c) to illustrate that hydrophobicity of the covered areas.

a) before treatment   b) after treated for 15 minutes   c) showing superhydrophilicity in the exposed area
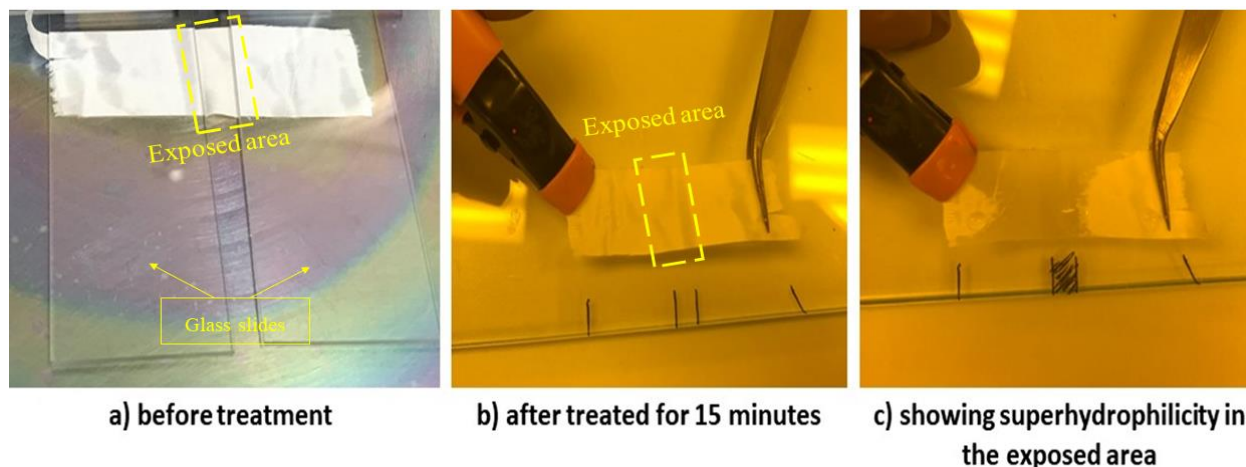
Figure 6-9: Selective plasma treatment using glass slides: a) before treatment, b) after 15 minutes of plasma treatment, and c) contact angle test showing superhydrophilicity on edges of the exposed area.

Selective Treatment Using Aluminum Foil

An aluminum foil (thickness $\sim 18 \mu$m) was also used for selective plasma treatment of the PVDF nanofibers substrate. Figure 6-10-a shows how the substrate was sandwiched and enveloped and only a rectangular area of the substrate was exposed to the plasma. After 15 minutes of treatment, the rectangular exposed area color became yellowish. Figure 6-10-b shows the change of color after the plasma treatment.
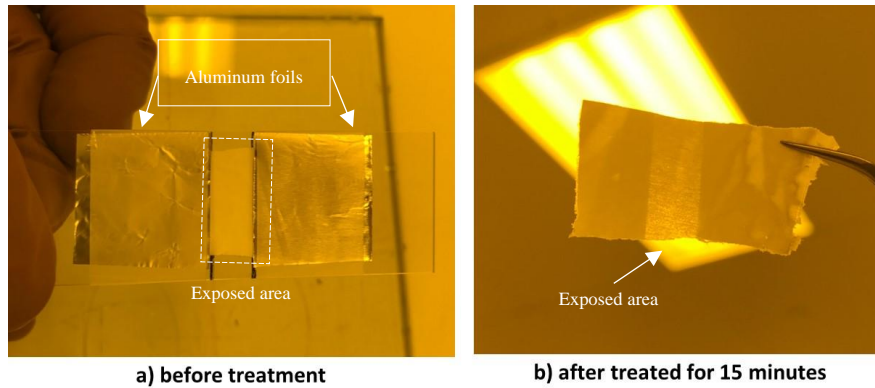
Figure 6-10: Selective plasma treatment using aluminum foil: a) before treatment, and b) after treatment for 15 minutes showing changing color in the exposed area.

To investigate the hydrophilicity effect, a water droplet was dropped on the exposed area. Figure 6-11 illustrates how the water droplet was absorbed into the substrate in a series of 12 images. Surprisingly, the water droplet stayed on the surface for about 1 second before it started to get adsorbed. Also, the absorbing rate was much higher in the areas that were covered by the aluminum foil than the absorbing rate in the yellowish area that was exposed to the plasma.
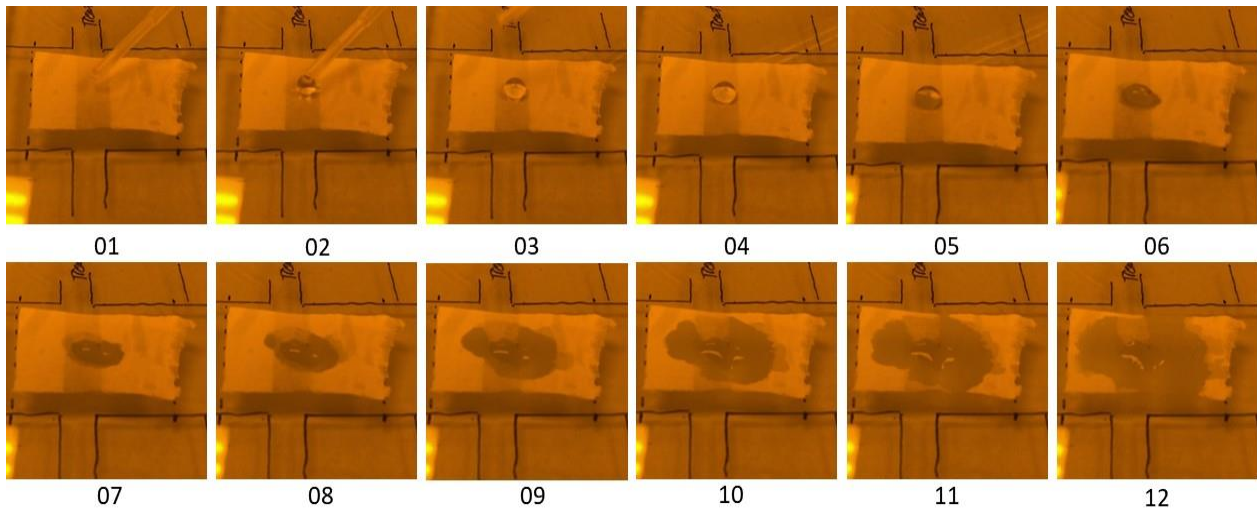
Figure 6-11: Images recorded during dropping a water droplet on the substrate that was selectively treated using aluminum foil.

The following hypotheses are suggested that led to the unexpected results:

- The yellowish color appeared in the exposed area can be a sign of burning/oxidation. Burning of PVDF polymer leads to reaction of hydrogen atoms in the PVDF backbone with oxygen molecules during the plasma treatment forming water vapor that was removed by vacuum system of plasma machine.

- Reducing the hydrogen atoms in the PVDF carbon backbone diminish the hydrophilicity feature of the exposed area.

- The aluminum foil acted as an additional electrode in the plasma chamber that increased the plasma power. The aluminum foil could excite the oxygen and Nitrogen molecules present in the porous structure of PVDF nanofibers underneath of the covered area led to internal nitrogen/oxygen plasma treatment. This internal surface treatment made the covered areas super-hydrophilic; however, because the covered areas were sandwiched and enveloped, due to lack of oxygen molecules, they were not oxidized, and the yellowish color did not appear.

- It is recommended that additional experiments and investigations are required to determine the reasons that led to achieve yellowish color in the exposed area as well as highly plasma treatment of the areas covered by the aluminum foil.

Since investigation of the mentioned hypotheses were beyond the scope of this research, more investigation on selective PVDF plasma treatment was put aside for the future works.

6.3   MFC Electrochemical Results

Figure 6-12 illustrates the polarization performance and power curves of PVDF-based MFC.
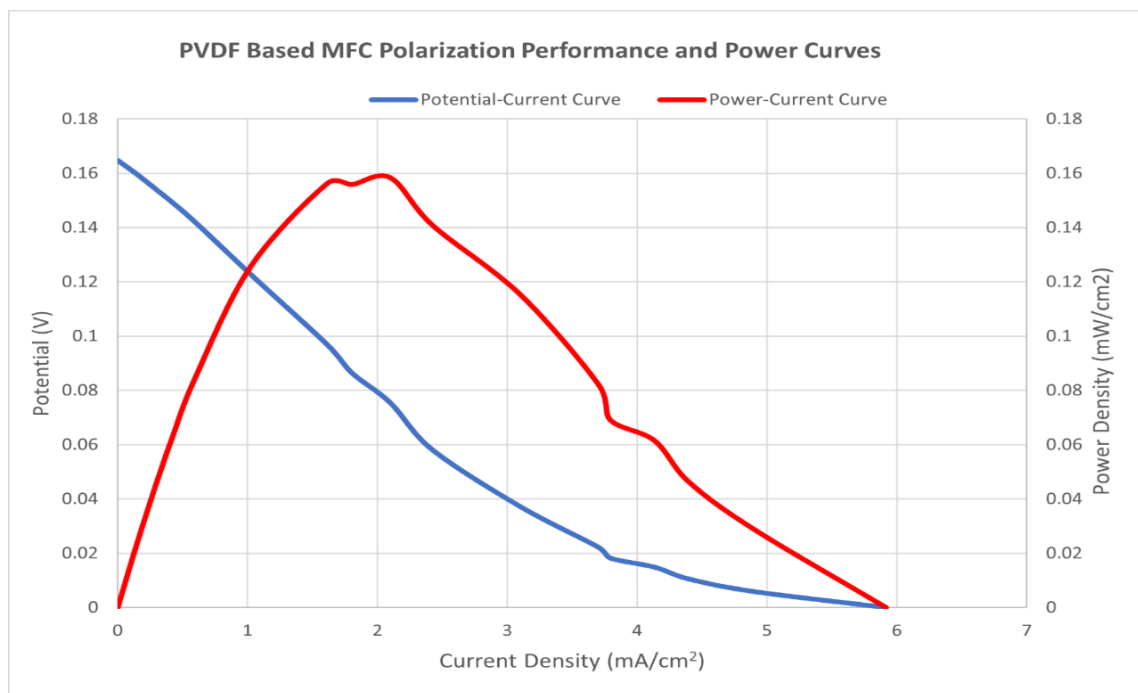
Figure 6-12: Polarization performance and power curves of PVDF-based MFC acquired by using PB/Pt as cathode/anode catalysts and 0.5 M hydrogen peroxide in 0.1 M HCl as the fuel.

PVDF-based MFC using PB/Pt as cathode/anode catalysts and inducing a capillary flow of 0.5 M hydrogen peroxide in 0.1 M HCl as the fuel showed the highest power density of 0.158 mW/cm2 at 0.08 V. The OCP of system was 164.8 mV, and the internal resistance (the slope of ohmic polarization region) is 43.6 Ω/cm2. The maximum current density of 6 mA/cm2 was also obtained.

6.3.1 Comparison of Dynamic State PVDF-Based MFC Electrochemical Performance with Previously Reported Dynamic State Paper-Based Microfluidic Biofuel Cells

The electrochemical performance of PVDF-based MFC was investigated by comparing its polarization and power curves with two recent paper-based microfluidic biofuel cells reported in the literature. In 2017, Maria Jos´e Gonza´lez-Guerrero et al. used Whatman paper as channel in an I-shaped microfluidic biofuel cell with an induced capillary flow of glucose solution (as fuel) and obtained the highest power density of 0.09 mW/cm2 at 0.4 V [35]. In 2018, Prakash Rewatkar and Sanket Goel used Whatman paper as a channel substrate in an Y-shaped microfluidic biofuel with and induced capillary flow of glucose solution (as fuel) and obtained a power density of 0.1 mW/cm^2 at 0.18 V [106]. The power curves and polarization curves of the aforementioned fuel cells are compared with PVDF-based MFC in Figure 6-13 and Figure 6-14, respectively.
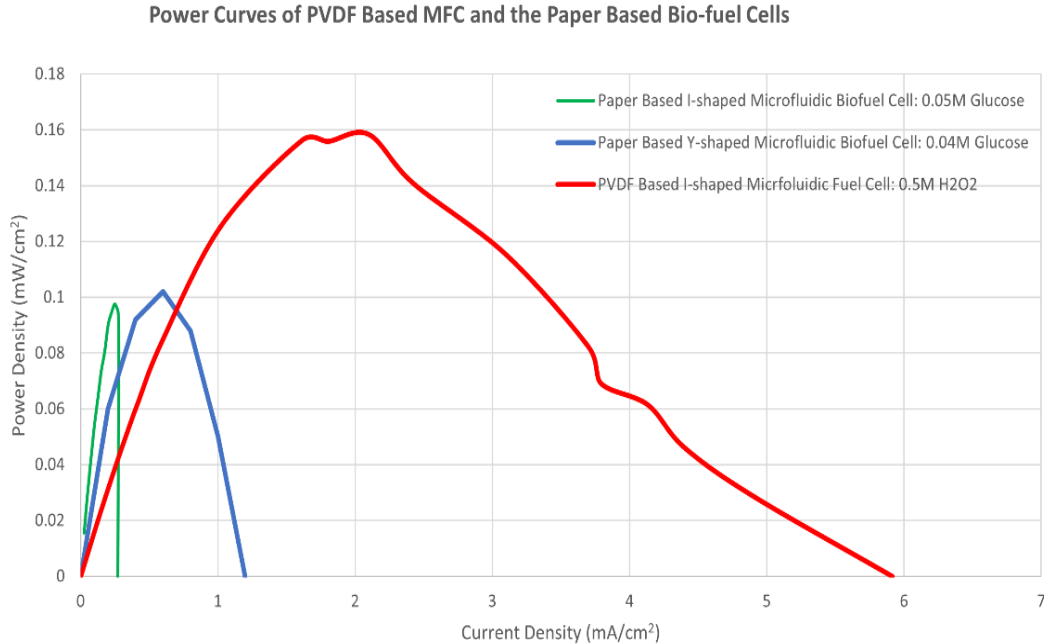
Figure 6-13: Power curves of PVDF-based MFC and the two paper-based microfluidic biofuel cells reported in the literature (the biofuel cells data shown in green and blue plots were obtained from [35] and [106], respectively).

74

Poliraztion Performance of PVDF Based MFC and the Paper Based Bio-fuel Cells
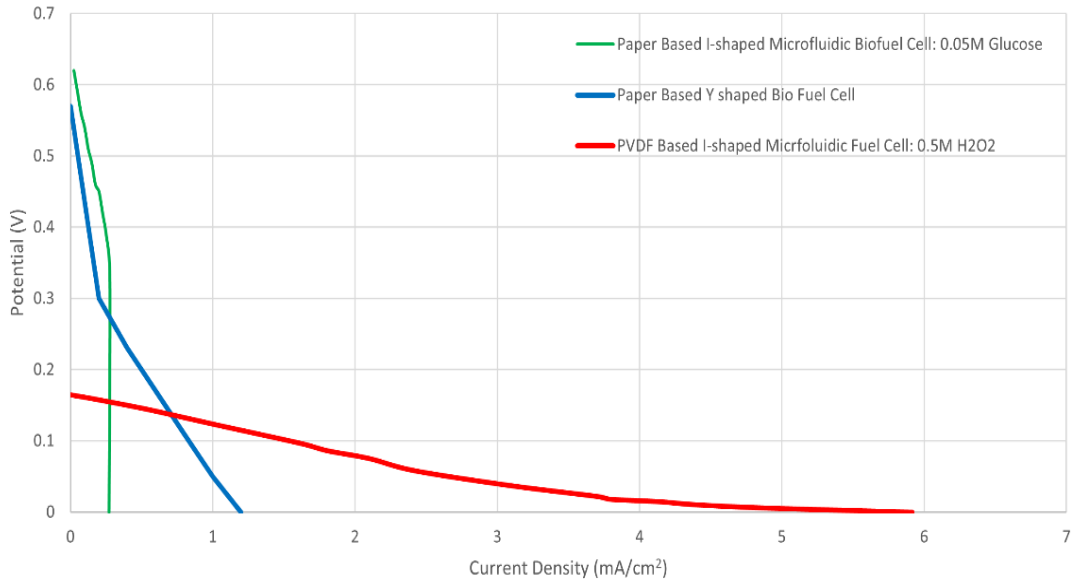
Figure 6-14: Polarization performance of PVDF-based MFC and the two paper-based microfluidic biofuel cells reported in the literature (the biofuel cells data shown in green and blue plots were obtained from [35] *and* [106]*, respectively).*

As illustrated in Figure 6-13, 60% higher power density was obtained by PVDF-based MFC in comparison with the other two biofuel cells reported in [35] and [106].

Based on Figure 6-14, the internal resistances of paper-based I-shaped fuel cell and paper-based Y-shaped fuel cell are 1040 Ω/cm^2 and 1350 Ω/cm^2, respectively. PVDF-based MFC (internal resistance of 43.6 Ω/cm^2) showed a better performance with respect to ohmic loss.

6.3.2 Comparison of Dynamic State PVDF-Based MFC Electrochemical Performance with Previously Reported Static State Single Compartment MFCs

The electrochemical performance of PVDF-based MFC was also investigated by comparing its polarization and power curves with two previously reported static state single compartment fuel cells using the same fuel type and concentration (0.5 M H_2O_2 in 0.1 M HCl).

In 2016, S. M. M. Ehteshami, et al. evaluated a static state single compartment fuel cell using Whatman paper as channel substrate and obtained the highest power density of 0.38 mW/cm^2 at 0.14 V when the cell was operating on 0.5 M hydrogen peroxide, PB as the cathode catalyst, and Ni as the anode catalyst [107].

75

Similarly, in 2017, M. Asadnia, et al. evaluated an static state single compartment fuel cell using PVDF nanofibers as channel substrate and obtained the highest power density of 0.33 mW/cm^2 at the cell potentials of 0.2 V when the cell was operating on 0.5 M hydrogen peroxide, PB as the cathode catalyst, and Ni as the anode catalyst [16]. The cell was previously shown in Figure 2-4.

The power curves and polarization curves of the aforementioned static state single compartment fuel cells are compared with dynamic state PVDF-based MFC in Figure 6-15 and Figure 6-16, respectively.
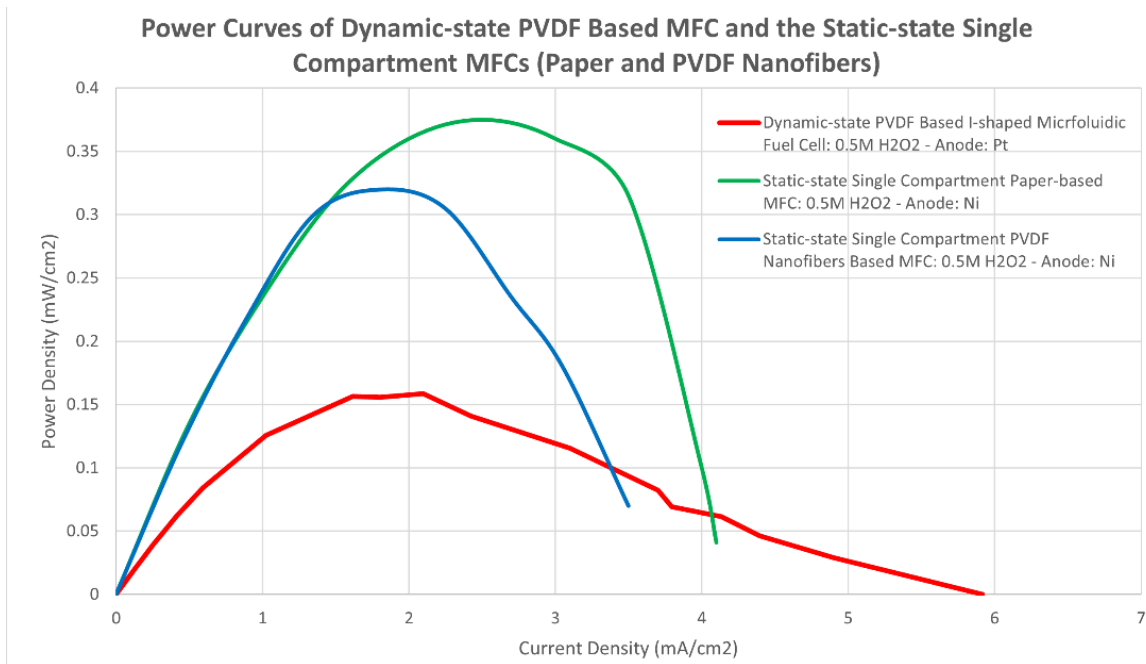
Figure 6-15: Power curves of dynamic state PVDF-based MFC and the static state single compartment MFCs reported in the literature with the same solution, concentration, and cathode catalyst (single compartment MFCs data, shown in blue and green plots were obtained from [16] *and* [107]*, respectively).*
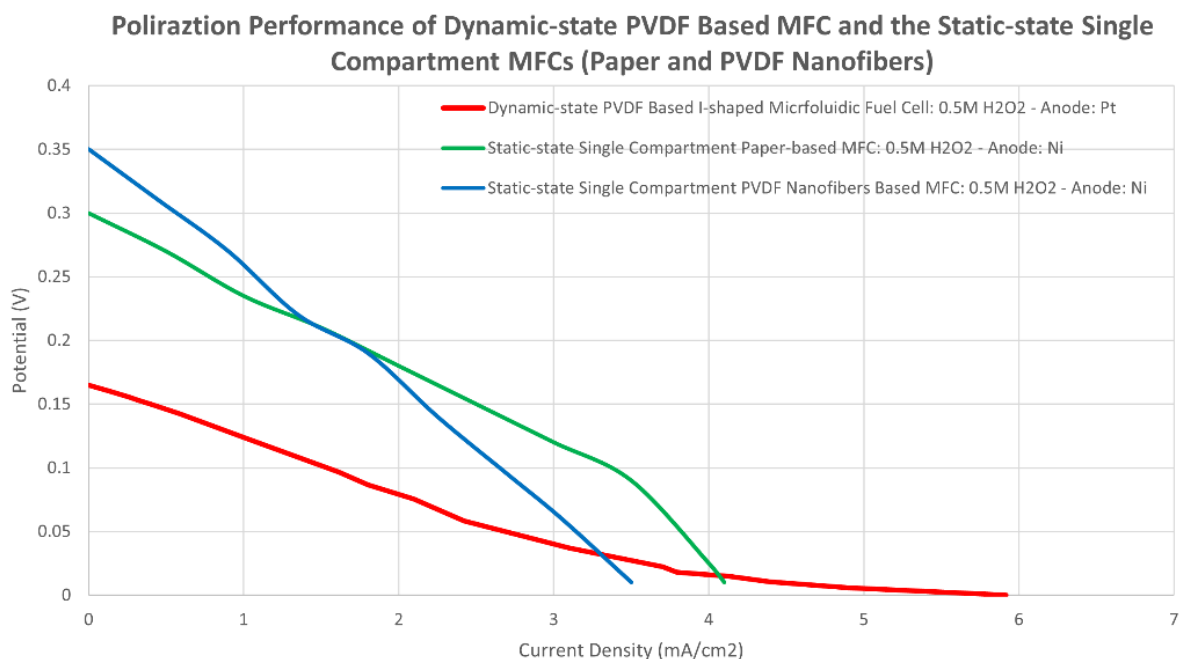
Figure 6-16: Polarization performance of dynamic state PVDF-based MFC and the static state Single Compartment MFCs reported in the literature with the same solution, concentration, and cathode catalyst (single compartment MFCs data, shown in blue and green plots were obtained from [16] *and* [107]*, respectively).*

The dynamic state PVDF-based MFC showed a lower OCP of 0.164 V in comparison with 0.35 V reported by [16] and 0.3 V reported by [107]. A lower OCP was expected as the electrode area was 1.5 times smaller and the distance between the anode and cathode was in microscale (~125 μm in comparison with electrodes distances of 5-10 mm reported by [16] and [107]). The microscale distance between electrodes increases cross-over of fuel leading to a lower OCP.

In terms of ohmic losses, the internal resistances of the static state paper-based fuel cell and PVDF nanofibers-based fuel cell are 65 Ω/cm^2 and 89 Ω/cm^2, respectively. Therefore, PVDF-based MFC (internal resistance of 43.6 Ω/cm^2) showed a better performance in respect to ohmic loss.

In terms of power density, the dynamic state PVDF MFC showed the power density of 0.158 mW/cm^2 at 0.08 V that was 52% lower than what [107] was reported, i.e. 0.33 mW/cm^2 at 0.2 V and 58% lower than what [16] reported, i.e. 0.38 mW/cm^2 at 0.2 V. However, it must be noted that static state single compartment MFCs achieved higher power densities owing to a higher cell potential as compared to the dynamic state PVDF MFC studied here.

In making this comparison, between the dynamic state PVDF MFC studied here and the static state single compartment MFCs reported in [16] and [107], it is also important to note that they are not identical MFCs. Differences in MFC features such as cell potential, fuel efficiency, dynamic/static state behaviour, cell dimensions, etc. also need to be considered.

7 CONCLUSION AND FUTURE WORK

7.1   Overview and Conclusion

Microfluidic fuel cells (MFCs) are novel and highly efficient energy harvester systems that have been vastly studied. Despite showing significant potentials, MFC systems have not yet been commercially used for implantable/wearable devices due to the sophisticated design process, high material costs, and time-consuming manufacturing process. Recently, porous materials such as natural papers and synthetic polymers (in the form of either nanofibers or porous membranes), when used as the MFC substrate, have shown that they can simplify the above-mentioned challenges. More importantly, these porous materials induce an inherent capillary flow in the fuel eliminating the need of a pump. This leads to the increased fuel efficiency and miniaturization of MFCs. However, the search for a porous biomaterial that displays high mechanical strength but remains flexible without degrading in a biological environment is not straightforward.

This thesis proposes PVDF, a non-biodegradable, biocompatible, flexible, and inexpensive material, as a channel substrate that has never been investigated for a dynamic state MFC. To achieve substrate porosity, flexibility, and desired material strength, PVDF nanofibers were fabricated using electrospinning technique. Non-aligned PVDF nanofibers were fabricated using a static collector and aligned PVDF nanofibers were achieved by a rotating drum. Additionally, PVDF nanofibers were fabricated in two different arrangements of the needle tip (horizontal and vertical - relative to the collector) for different flow rates. The results showed that the alignment, fiber size and bead formations of electrospun PVDF nanofibers agreed with the previous studies.

Super hydrophobicity limits PVDF from being used MFCs. One solution was to enhance PVDF hydrophilicity. Therefore, hydrophilic PVDF nanofibers were successfully achieved by oxygen plasma surface treatment. The hydrophilicity of resulting PVDF nanofibers was verified using the contact angle method. Furthermore, to achieve higher precision in the channel structure (compared to cutting-out the substrate channel), selective enhancement of surface hydrophilicity was studied. Surface-selective plasma treatment was performed using three different materials (PMMA sheet,

glass slides, and aluminum foil) to mask the substrate region outside the channel. PMMA sheet successfully prevented the covered area from surface modification. However, it was observed that the PMMA sheet thickness used, 2 mm, was enough to reduce the efficiency of the surface treatment causing lower than expected hydrophilicity in the channel. Subsequently, glass slides with a lower thickness (1mm) were used. In contrast with PMMA sheet, the results showed that the covered area got modified from the treatment possibly because the glass slide did not fully envelope the uneven surface of the substrate allowing accelerated argon/oxygen plasma to penetrate underneath the mask. Finally, aluminum foil, as a thinner (~18µm) and more flexible material was used. The results showed that aluminum foil was not only unsuccessful in blocking the surface modification, but also caused the masked area to have a higher hydrophilicity than the exposed channel. This could be attributed to the yellowish appearance of the exposed area i.e. signs of plasma burning. Since further investigations on surface-selective treatment of PVDF nanofibers were beyond the scope of this research, the channel geometry was decided to be hand-cut from the substrate material. Additionally, due to unanticipated device malfunction (fully described in section 7.2) a commercially available PVDF hydrophilic porous membrane was purchased and tested in the designed MFC.

To investigate the electrochemical performance of PVDF membrane, an MFC system was designed by following advanced engineering design theories (Axiomatic Design Theory and FCBPSS framework). Consequently, 3D printing fabrication technique was used to prototype the designed MFC. Hydrogen peroxide in acidic environment (i.e. 0.5 M hydrogen peroxide in 0.1 M HCl) was used as the fuel while Pd and PB were used as anode and cathode catalysts, respectively. In the electrochemical test, the MFC system as described with an OCP of 0.164 V achieved its highest power density of 0.158 mW/cm^2 at 0.08 V.

To summarize, in this research, PVDF (as a channel substrate) was tested for the first time in a dynamic state MFC. This dynamic state PVDF-based MFC showed a lower power density with respect to the previously reported static state single compartment fuel cells (using the same fuel concentration and cathode catalysts). However, it must be noted that the dynamic state PVDF power density was achieved in an MFC with a lower cell potential of 0.08 V in comparison with cell potentials static state MFCs, 0.14 V and 0.2 V. On the other hand, the dynamic state PVDF-based MFC studied here showed a 60% higher value in power density with respect to recently reported paper-based microfluidic biofuel cells. Notably, this research suggests that PVDF, as a

non-degradable, biocompatible, flexible, and cost-effective material shows tremendous potential as a channel substrate for MFCs designed to harvest energy required by implantable/wearable devices.

7.2 **Contributions**

The overall objective of this research was to develop a dynamic state MFC with PVDF as its channel substrate. The following sub-objectives were specified to achieve this goal.

Objective 1: qualitatively analyzing the PVDF channel system as an MFC sub-system, to find a suitable channel structure that performs the overall system function.

This objective was achieved as explained in Chapter 3 (Design). In the aforementioned chapter, by using FCBPSS, the I-shaped channel structure was determined as the most compatible structure for a PVDF-based MFC. The design was represented by FR, CR, and DP. Further, ADT was employed to lead to the I-shaped PVDF structure, which meets Axiom 1 in ADT, namely it is a good design.

Objective 2: developing a suitable technique to fabricate a porous PVDF substrate.

Electrospinning technique, was selected from a thorough literature review of different nanofiber fabrication methods (subsection 2.8.2). Then, the details of how the electrospinning device was developed were explained in section 4.1 (Electrospinning Device). And finally, the electrospinning process and parameters that were used to fabricate PVDF substrate were explained in section 4.2.

Objective 3: analyzing the porous structure and capillary action of the fabricated PVDF substrate out of the research for Objective 2.

Porous structure of electrospun PVDF nanofibers were analyzed in section 5.1 (inspection of electrospun PVDF nanofibers) by using SEM technique and image processing. Furthermore, the capillary action of the electrospun PVDF nanofibers were investigated by performing a plasma surface treatment to enhance the hydrophilicity (section 5.2) followed by verification using contact angle technique and image processing method in subsections 5.2.1 and 5.2.2 respectively.

Objective 4: testing and characterizing the electrochemical efficiency of a porous PVDF substrate out of the research for Objective 2 in an MFC system.

Firstly, the MFC system fabrication methods were investigated by using two techniques: microfabrication using UV-lithography and 3D-printing (Subsection 3.4). After investigation, 3D-printing method, was selected as a feasible prototyping method to fabricate the I-shaped PVDF-based MFC. Secondly, at this stage of the research, the plasma treatment device (RIEUSAS-RIE-72109-NP1) suffered a malfunction and due to unavailability of any other plasma treatment device, a commercial hydrophilic porous PDVF membrane with average pore size of 0.22 µm (220 nm) was purchased. This material was chosen because it showed the closest resemblance to the PVDF nanofibers achieved out of the research objective 2. PVDF-based dynamic state MFC was tested with the same fuel concentration and cathode catalyst that were used in previous fuel cell studies that used paper-based and PVDF-based fuel cells but in static state.

Therefore, the overall objective of this research was successfully achieved.

7.3   Limitations and Future Works

In the following subsection, the limitations and obstacles of this research are briefly discussed and recommendations for future work are proposed:

7.3.1   Plasma Surface Treatment of PVDF Nanofibers

The required plasma power reported previously in the literature (see [99]) to enhance hydrophilicity of PVDF nanofibers was 360 W for 120 seconds. Although the plasma device used in this research (RIEUSAS-RIE-72109-NP1) had a nominal output power of 600 W, due to technical issues, the maximum power that could be used was 50 W. Therefore, the treatment time was increased to compensate for the low power output. Consequently, an investigation was performed to find the minimum treatment time required to make PVDF nanofibers super hydrophilic. This approach resulted in several issues: a) exposing nanofibers for an extended period of time with low energy oxygen molecules gave the surface a brownish appearance that may be considered an indicator for surface burning, b) this long exposure time may alter the desired chemical properties of PVDF nanofibers.

For the future work, it is highly recommended that a reliable plasma treatment device be used with the previously reported plasma treatment settings. Furthermore, an investigation into the effect of plasma surface treatment on the biocompatibility and biodegradability of PVDF nanofibers is suggested.

7.3.2   **PVDF-Based MFC Microfabrication by Using UV-lithography Technique**

Microfabrication by UV-lithography technique for PVDF nanofibers-based MFC was carefully discussed and illustrated in Appendix B. However, microfabrication was not employed in this research due to reasons discussed below:

- Assembly and alignment of micro-fabricated three layers are challenging and time consuming

- After assembly of the micro-fabricated layers, changing the channel substrate or electrodes are not achievable. Therefore, a new MFC system will need to be fabricated for each test.

- Cutting the PVDF substrate to form the micro-channel is not doable. Also, electrospinning the PVDF directly on the channel substrate is not doable due to non-conductivity of SUEX.

- PVDF-based MFC induced by capillary flow has not been tested before and Micro-fabrication method is not a suitable method for prototyping.

For the future work, since PVDF showed a favorable performance as a channel substrate in MFC system, it is recommended that PVDF-based MFC will be fabricated by microfabrication technique and will be tested as it is known that reducing the MFC size can increase the fuel efficiency. Furthermore, microfabrication technique has a higher design accuracy in comparison with 3D printing method of prototyping and thus may lead to more reliable electrochemical output.

7.3.3   **Effect of Aligned/Non-aligned PVDF Nanofibers in MFC Systems**

To the best of my knowledge, the effect of nanofibers alignment on the capillary action and electrochemical output (current and power densities) have not yet been investigated.

One may suggest conducting a computer simulation to study the effect of nanofibers alignment on the capillary flow action and the resulting MFC electrochemical output. However, the nanofibers consist of billions of pores in nanoscale and simulation of such a complicated system will need to be verified with results from identical MFC experiments.

In this research, one initial research idea was to experimentally test the effect of nanofiber alignment on capillary flow action and electrochemical output. However, due to plasma treatment device malfunction, and unavailability of any other plasma treatment device in the institution, there was no chance to test this research idea.

For the future work, it is recommended that one aligned PVDF nanofibers substrate and one non-aligned PVDF nanofibers with the same electrospinning parameters and the same plasma treatment parameters will be fabricated to test the effect of alignment on capillary flow action. Furthermore, both the aligned/non-aligned substrates may be tested in the same MFC to investigate the effect of PVDF nanofibers alignment on electrochemical output.

REFERENCES

[1] J. Coffel and E. Nuxoll, "BioMEMS for biosensors and closed-loop drug delivery," *Int. J. Pharm.*, vol. 544, no. 2, pp. 335–349, 2018.

[2] R.-F. Xue, K.-W. Cheng, and M. Je, "High-efficiency wireless power transfer for biomedical implants by optimal resonant load transformation," *IEEE Trans. Circuits Syst. I Regul. Pap.*, vol. 60, no. 4, pp. 867–874, 2012.

[3] X. Liu, F. Zhang, S. A. Hackworth, R. J. Sclabassi, and M. Sun, "Wireless power transfer system design for implanted and worn devices," in *2009 IEEE 35th Annual Northeast Bioengineering Conference*, 2009, pp. 1–2.

[4] S. Ozeri and D. Shmilovitz, "Ultrasonic transcutaneous energy transfer for powering implanted devices," *Ultrasonics*, vol. 50, no. 6, pp. 556–566, 2010.

[5] C.-Y. Sue and N.-C. Tsai, "Human powered MEMS-based energy harvest devices," *Appl. Energy*, vol. 93, pp. 390–403, 2012.

[6] M. R. Mhetre and H. K. Abhyankar, "Human exhaled air energy harvesting with specific reference to PVDF film," *Eng. Sci. Technol. an Int. J.*, vol. 20, no. 1, pp. 332–339, 2017.

[7] M. Thielen, L. Sigrist, M. Magno, C. Hierold, and L. Benini, "Human body heat for powering wearable devices: From thermal energy to application," *Energy Convers. Manag.*, vol. 131, pp. 44–54, 2017.

[8] M. A. Halim, H. Cho, and J. Y. Park, "Design and experiment of a human-limb driven, frequency up-converted electromagnetic energy harvester," *Energy Convers. Manag.*, vol. 106, pp. 393–404, 2015.

[9] Y. Lu, F. Cottone, S. Boisseau, F. Marty, D. Galayko, and P. Basset, "A nonlinear MEMS electrostatic kinetic energy harvester for human-powered biomedical devices," *Appl. Phys. Lett.*, vol. 107, no. 25, p. 253902, 2015.

[10] C. Dagdeviren *et al.*, "Conformal piezoelectric energy harvesting and storage from motions of the heart, lung, and diaphragm," *Proc. Natl. Acad. Sci.*, vol. 111, no. 5, pp. 1927–1932, 2014.

[11] M. Falk, C. W. Narváez Villarrubia, S. Babanova, P. Atanassov, and S. Shleev, "Biofuel cells for biomedical applications: colonizing the animal kingdom," *ChemPhysChem*, vol. 14, no. 10, pp. 2045–2058, 2013.

[12] J. wook Lee and E. Kjeang, "A perspective on microfluidic biofuel cells," *Biomicrofluidics*, vol. 4, no. 4, p. 5181, 2010.

[13] E. R. Choban, L. J. Markoski, A. Wieckowski, and P. J. A. Kenis, "Microfluidic fuel cell based on laminar flow," *J. Power Sources*, vol. 128, no. 1, pp. 54–60, 2004.

[14] J. P. Esquivel, F. J. Del Campo, J. L. G. de la Fuente, S. Rojas, and N. Sabate, "Microfluidic fuel cells on paper: meeting the power needs of next generation lateral flow devices," *Energy Environ. Sci.*, vol. 7, no. 5, pp. 1744–1749, 2014.

[15] M. Safdar, J. Jänis, and S. Sanchez, "Microfluidic fuel cells for energy generation," *Lab Chip*, vol. 16, no. 15, pp. 2754–2758, 2016.

[16] M. Asadnia, S. M. M. Ehteshami, S. H. Chan, and M. E. Warkiani, "Development of a fiber-based membraneless hydrogen peroxide fuel cell," *RSC Adv.*, vol. 7, no. 65, pp. 40755–40760, 2017.

[17] K. D. Wise and K. Najafi, "Microfabrication techniques for integrated sensors and microsystems," *Science (80-.).*, vol. 254, no. 5036, pp. 1335–1342, 1991.

[18] A. C. R. Grayson *et al.*, "A BioMEMS review: MEMS technology for physiologically integrated devices," *Proc. IEEE*, vol. 92, no. 1, pp. 6–21, 2004.

[19] S. Bhansali and A. Vasudev, *MEMS for biomedical applications*. Elsevier, 2012.

[20] K. Menon, R. A. Joy, N. Sood, and R. K. Mittal, "The applications of bioMEMS in diagnosis, cell biology, and therapy: a review," *Bionanoscience*, vol. 3, no. 4, pp. 356–366, 2013.

[21] G. M. Whitesides, "The origins and the future of microfluidics," *Nature*, vol. 442, p. 368, Jul. 2006.

[22] H. Song, T. C. Xia, S. M. Wang, and Y. M. Lan, *Engineering fluid mechanics*. Springer, 2018.

[23] T. M. Squires and S. R. Quake, "Microfluidics: Fluid physics at the nanoliter scale," *Rev.*

Mod. Phys., vol. 77, no. 3, p. 977, 2005.

[24] R. O'hayre, S.-W. Cha, F. B. Prinz, and W. Colella, *Fuel cell fundamentals*. John Wiley & Sons, 2016.

[25] O. Z. Sharaf and M. F. Orhan, "An overview of fuel cell technology: Fundamentals and applications," *Renew. Sustain. Energy Rev.*, vol. 32, pp. 810–853, 2014.

[26] S. M. Haile, "Fuel cell materials and components," *Acta Mater.*, vol. 51, no. 19, pp. 5981–6000, 2003.

[27] S. J. Peighambardoust, S. Rowshanzamir, and M. Amjadi, "Review of the proton exchange membranes for fuel cell applications," *Int. J. Hydrogen Energy*, vol. 35, no. 17, pp. 9349–9384, 2010.

[28] D. J. Kim, M. J. Jo, and S. Y. Nam, "A review of polymer–nanocomposite electrolyte membranes for fuel cell application," *J. Ind. Eng. Chem.*, vol. 21, pp. 36–52, 2015.

[29] E. R. Choban, L. J. Markoski, J. Stoltzfus, J. S. Moore, and P. J. A. Kenis, "Microfluidic fuel cells that lack a PEM," in *Power Sources Proceedings*, 2002, vol. 40, pp. 317–320.

[30] E. Kjeang, N. Djilali, and D. Sinton, "Microfluidic fuel cells: A review," *J. Power Sources*, vol. 186, no. 2, pp. 353–369, 2009.

[31] J. Yang, S. Ghobadian, P. J. Goodrich, R. Montazami, and N. Hashemi, "Miniaturized biological and electrochemical fuel cells: challenges and applications," *Phys. Chem. Chem. Phys.*, vol. 15, no. 34, pp. 14147–14161, 2013.

[32] K. Purohit, *Paper microfluidic power sources*. California State University, Fullerton, 2017.

[33] M. Irimia-Vladu, "'Green' electronics: biodegradable and biocompatible materials and devices for sustainable future," *Chem. Soc. Rev.*, vol. 43, no. 2, pp. 588–610, 2014.

[34] J. P. Esquivel, F. del Campo, J. L. Fuente, S. Rojas, and N. Sabaté, "Paper-based microfluidic fuel cells," *17th Int. Conf. Miniaturized Syst. Chem. Life Sci. MicroTAS 2013*, vol. 2, pp. 1251–1253, Jan. 2013.

[35] M. J. González-Guerrero, F. J. del Campo, J. P. Esquivel, D. Leech, and N. Sabaté, "based microfluidic biofuel cell operating under glucose concentrations within physiological range," *Biosens. Bioelectron.*, vol. 90, pp. 475–480, 2017.

[36] R. K. Arun, S. Halder, N. Chanda, and S. Chakraborty, "A paper based self-pumping and self-breathing fuel cell using pencil stroked graphite electrodes," *Lab Chip*, vol. 14, no. 10, pp. 1661–1664, 2014.

[37] X. Yan, A. Xu, L. Zeng, P. Gao, and T. Zhao, "A paper-based microfluidic fuel cell with hydrogen peroxide as fuel and oxidant," *Energy Technol.*, vol. 6, no. 1, pp. 140–143, 2018.

[38] M. Chanda and S. K. Roy, *Industrial polymers, specialty polymers, and their applications*, vol. 74. CRC press, 2008.

[39] "1-Chloro-1,1-difluoroethane | CH3-CClF2 - PubChem." [Online]. Available: https://pubchem.ncbi.nlm.nih.gov/compound/1-Chloro-1_1-difluoroethane. [Accessed: 16-Jun-2020].

[40] S. Houis, E. Engelhardt, F. Wurm, T. G.-M. and H. Textiles, and undefined 2010, "Application of polyvinylidene fluoride (PVDF) as a biomaterial in medical textiles," *Elsevier*.

[41] S. Baskaran, X. He, Q. Chen, and J. Y. Fu, "Experimental studies on the direct flexoelectric effect in α-phase polyvinylidene fluoride films," *Appl. Phys. Lett.*, vol. 98, no. 24, p. 242901, 2011.

[42] D. Mondal *et al.*, "Enhancement of β-phase crystallization and electrical properties of PVDF by impregnating ultra high diluted novel metal derived nanoparticles: Prospect of use as a charge storage device," *J. Mater. Sci. Mater. Electron.*, vol. 29, no. 17, pp. 14535–14545, 2018.

[43] X. Cai, T. Lei, D. Sun, and L. Lin, "A critical analysis of the α, β and γ phases in poly (vinylidene fluoride) using FTIR," *RSC Adv.*, vol. 7, no. 25, pp. 15382–15389, 2017.

[44] M. Li *et al.*, "Revisiting the δ-phase of poly (vinylidene fluoride) for solution-processed ferroelectric thin films," *Nat. Mater.*, vol. 12, no. 5, pp. 433–438, 2013.

[45] A. J. Lovinger, "Annealing of poly (vinylidene fluoride) and formation of a fifth phase," *Macromolecules*, vol. 15, no. 1, pp. 40–44, 1982.

[46] S. Mishra, L. Unnikrishnan, S. K. Nayak, and S. Mohanty, "Advances in piezoelectric polymer composites for energy harvesting applications: A systematic review," *Macromol.*

Mater. Eng., vol. 304, no. 1, p. 1800463, 2019.

[47]   L. Ruan, X. Yao, Y. Chang, L. Zhou, G. Qin, and X. Zhang, "Properties and Applications of the β Phase Poly (vinylidene fluoride)," *Polymers (Basel).*, vol. 10, no. 3, p. 228, 2018.

[48]   Y. Li, C. Liao, and S. C. Tjong, "Electrospun polyvinylidene fluoride-based fibrous scaffolds with piezoelectric characteristics for bone and neural tissue engineering," *Nanomaterials*, vol. 9, no. 7, p. 952, 2019.

[49]   A. J. Lovinger, "Unit cell of the γ phase of poly (vinylidene fluoride)," *Macromolecules*, vol. 14, no. 2, pp. 322–325, 1981.

[50]   R. Gregorio and E. M. Ueno, "Effect of crystalline phase, orientation and temperature on the dielectric properties of poly (vinylidene fluoride)(PVDF)," *J. Mater. Sci.*, vol. 34, no. 18, pp. 4489–4500, 1999.

[51]   Z. Guo, E. Nilsson, M. Rigdahl, and B. Hagström, "Melt spinning of PVDF fibers with enhanced β phase structure," *J. Appl. Polym. Sci.*, vol. 130, no. 4, pp. 2603–2609, 2013.

[52]   Y. Bormashenko, R. Pogreb, O. Stanevsky, and E. Bormashenko, "Vibrational spectrum of PVDF and its interpretation," *Polym. Test.*, vol. 23, no. 7, pp. 791–796, 2004.

[53]   N. Pezeshk, D. Rana, R. M. Narbaitz, and T. Matsuura, "Novel modified PVDF ultrafiltration flat-sheet membranes," *J. Memb. Sci.*, vol. 389, pp. 280–286, 2012.

[54]   J. Ji, F. Liu, N. A. Hashim, M. R. M. Abed, and K. Li, "Poly (vinylidene fluoride)(PVDF) membranes for fluid separation," *React. Funct. Polym.*, vol. 86, pp. 134–153, 2015.

[55]   AllPlastics.com, "PVDF Material Properties Data Sheet." [Online]. Available: https://www.allplastics.com.au/component/docman/doc_download/99-allplastics-pvdf-kynar-datasheet-pdf?Itemid=. [Accessed: 16-Jun-2020].

[56]   "Polyvinylidene Fluoride (PVDF) Plastic: Material Properties & Other Info." [Online]. Available: https://omnexus.specialchem.com/selection-guide/polyvinylidene-fluoride-pvdf-plastic. [Accessed: 16-Jun-2020].

[57]   G. Kang and Y. Cao, "Application and modification of poly (vinylidene fluoride)(PVDF) membranes–a review," *J. Memb. Sci.*, vol. 463, pp. 145–165, 2014.

[58]   A. Toprak and O. Tigli, "MEMS scale PVDF-TrFE-based piezoelectric energy harvesters,"

J. Microelectromechanical Syst., vol. 24, no. 6, pp. 1989–1997, 2015.

[59] G. D. Ram and S. Praveenkumar, "PVDF polymer-based MEMS cantilever for energy harvesting," in *Artificial Intelligence and Evolutionary Computations in Engineering Systems*, Springer, 2016, pp. 917–923.

[60] D. M. Correia *et al.*, "Electrosprayed poly (vinylidene fluoride) microparticles for tissue engineering applications," *Rsc Adv.*, vol. 4, no. 62, pp. 33013–33021, 2014.

[61] A. Ardeshirylajimi, S. M.-H. Ghaderian, M. D. Omrani, and S. L. Moradi, "Biomimetic scaffold containing PVDF nanofibers with sustained TGF-β release in combination with AT-MSCs for bladder tissue engineering," *Gene*, vol. 676, pp. 195–201, 2018.

[62] F. Muysoms, R. Beckers, and I. Kyle-Leinhase, "Prospective cohort study on mesh shrinkage measured with MRI after laparoscopic ventral hernia repair with an intraperitoneal iron oxide-loaded PVDF mesh," *Surg. Endosc.*, vol. 32, no. 6, pp. 2822–2830, 2018.

[63] F. Amini, D. Semnani, S. Karbasi, and S. N. Banitaba, "A novel bilayer drug-loaded wound dressing of PVDF and PHB/Chitosan nanofibers applicable for post-surgical ulcers," *Int. J. Polym. Mater. Polym. Biomater.*, vol. 68, no. 13, pp. 772–777, 2019.

[64] S. Park *et al.*, "PVDF-based piezoelectric microphone for sound detection inside the cochlea: toward totally implantable cochlear implants," *Trends Hear.*, vol. 22, p. 2331216518774450, 2018.

[65] K. A. R. Medeiros, C. R. H. Barbosa, J. R. M. d'Almeida, A. S. Ribeiro, and I. B. de Paula, "Flowmeter based on a piezoelectric PVDF tube," *Measurement*, vol. 138, pp. 368–378, 2019.

[66] T. A. Otitoju, A. L. Ahmad, and B. S. Ooi, "Polyvinylidene fluoride (PVDF) membrane for oil rejection from oily wastewater: A performance review," *J. Water Process Eng.*, vol. 14, pp. 41–59, 2016.

[67] Z.-M. Huang, Y.-Z. Zhang, M. Kotaki, and S. Ramakrishna, "A review on polymer nanofibers by electrospinning and their applications in nanocomposites," *Compos. Sci. Technol.*, vol. 63, no. 15, pp. 2223–2253, 2003.

[68] Y. Liu *et al.*, "UV-crosslinked Solution Blown PVDF Nanofiber Mats for Protective Applications," *Fibers Polym.*, vol. 21, no. 3, pp. 489–497, 2020.

[69] D. Lolla, A. Abutaleb, M. A. Kashfipour, and G. G. Chase, "Polarized Catalytic Polymer Nanofibers," *Materials (Basel).*, vol. 12, no. 18, p. 2859, 2019.

[70] L. Huang, J. T. Arena, and J. R. McCutcheon, "Surface modified PVDF nanofiber supported thin film composite membranes for forward osmosis," *J. Memb. Sci.*, vol. 499, pp. 352–360, 2016.

[71] L.-Y. Wang, W. F. Yong, E. Y. Liya, and T.-S. Chung, "Design of high efficiency PVDF-PEG hollow fibers for air filtration of ultrafine particles," *J. Memb. Sci.*, vol. 535, pp. 342–349, 2017.

[72] M. M. Abolhasani, K. Shirvanimoghaddam, and M. Naebe, "PVDF/graphene composite nanofibers with enhanced piezoelectric performance for development of robust nanogenerators," *Compos. Sci. Technol.*, vol. 138, pp. 49–56, 2017.

[73] A. A. Almetwally, M. El-Sakhawy, M. H. Elshakankery, and M. H. Kasem, "Technology of nano-fibers: Production techniques and properties—Critical review," *J. Text. Assoc*, vol. 78, pp. 5–14, 2017.

[74] F. Anton, "Process and apparatus for preparing artificial threads." Google Patents, 02-Oct-1934.

[75] T. Subbiah, G. S. Bhat, R. W. Tock, S. Parameswaran, and S. S. Ramkumar, "Electrospinning of nanofibers," *J. Appl. Polym. Sci.*, vol. 96, no. 2, pp. 557–569, 2005.

[76] M. S. Islam, B. C. Ang, A. Andriyana, and A. M. Afifi, "A review on fabrication of nanofibers via electrospinning and their applications," *SN Appl. Sci.*, vol. 1, no. 10, p. 1248, 2019.

[77] A. Haider, S. Haider, and I.-K. Kang, "A comprehensive review summarizing the effect of electrospinning parameters and potential applications of nanofibers in biomedical and biotechnology," *Arab. J. Chem.*, vol. 11, no. 8, pp. 1165–1188, 2018.

[78] G. I. Taylor, "Disintegration of water drops in an electric field," *Proc. R. Soc. London. Ser. A. Math. Phys. Sci.*, vol. 280, no. 1382, pp. 383–397, 1964.

[79] K.-Y. Law, "Definitions for hydrophilicity, hydrophobicity, and superhydrophobicity: getting the basics right." ACS Publications, 2014.

[80] M. Zhang, Q. T. Nguyen, and Z. Ping, "Hydrophilic modification of poly (vinylidene fluoride) microporous membrane," *J. Memb. Sci.*, vol. 327, no. 1–2, pp. 78–86, 2009.

[81] F. A. Sheikh, M. A. Zargar, A. H. Tamboli, and H. Kim, "A super hydrophilic modification of poly (vinylidene fluoride)(PVDF) nanofibers: By in situ hydrothermal approach," *Appl. Surf. Sci.*, vol. 385, pp. 417–425, 2016.

[82] J. S. Gero and U. Kannengiesser, "The function-behaviour-structure ontology of design," in *An anthology of theories and models of design*, Springer, 2014, pp. 263–283.

[83] J. S. Gero, "Design prototypes: a knowledge representation schema for design," *AI Mag.*, vol. 11, no. 4, p. 26, 1990.

[84] J. S. Gero and U. Kannengiesser, "Towards a situated function-behaviour-structure framework as the basis of a theory of designing," in *Workshop on Development and Application of Design Theories in AI in Design Research, Artificial Intelligence in Design'00, Worcester, MA, pp. gk*, 2000, pp. 1–5.

[85] Y. Lin and W. J. Zhang, "Towards a novel interface design framework: function–behavior–state paradigm," *Int. J. Hum. Comput. Stud.*, vol. 61, no. 3, pp. 259–297, 2004.

[86] Y. Lin and W. J. Zhang, "A function-behavior-state approach to designing human-machine interface for nuclear power plant operators," *IEEE Trans. Nucl. Sci.*, vol. 52, no. 1, pp. 430–439, 2005.

[87] Y. He, "A novel approach to emergency management of wireless telecommunication system." Citeseer, 2008.

[88] W. J. Zhang and J. W. Wang, "Design theory and methodology for enterprise systems." Taylor & Francis, 2016.

[89] G. Pahl and W. Beitz, *Engineering design: a systematic approach*. Springer Science & Business Media, 2013.

[90] N. P. Suh, "Design and operation of large systems," *J. Manuf. Syst.*, vol. 14, no. 3, pp. 203–213, 1995.

[91]   N. P. Suh, "Axiomatic design theory for systems," *Res. Eng. Des.*, vol. 10, no. 4, pp. 189–209, 1998.

[92]   M. Liu, J. Wu, Y. Gan, D. A. H. Hanaor, and C. Q. Chen, "Tuning capillary penetration in porous media: combining geometrical and evaporation effects," *Int. J. Heat Mass Transf.*, vol. 123, pp. 239–250, 2018.

[93]   R. Lucas, "Ueber das Zeitgesetz des kapillaren Aufstiegs von Flüssigkeiten," *Kolloid-Zeitschrift*, vol. 23, no. 1, pp. 15–22, 1918.

[94]   E. W. Washburn, "The dynamics of capillary flow," *Phys. Rev.*, vol. 17, no. 3, p. 273, 1921.

[95]   S. Kantzas, Apostolos; Bryan Jonathan; Taheri, "Fundamentals of Fluid Flow in Porous Media," *Pore size Distrib.*, p. 336, 2015.

[96]   M. L. Soudijn, "Proton transport in aqueous ionic solutions," *Univ. Amsterdam*, 2012.

[97]   L. del Torno-de Román *et al.*, "Improved performance of a paper-based glucose fuel cell by capillary induced flow," *Electrochim. Acta*, vol. 282, pp. 336–342, 2018.

[98]   J. A. Adkins, E. Noviana, and C. S. Henry, "Development of a quasi-steady flow electrochemical paper-based analytical device," *Anal. Chem.*, vol. 88, no. 21, pp. 10639–10647, 2016.

[99]   D. M. Correia *et al.*, "Influence of oxygen plasma treatment parameters on poly (vinylidene fluoride) electrospun fiber mats wettability," *Prog. Org. Coatings*, vol. 85, pp. 151–158, 2015.

[100] Y. Yamada, S. Yoshida, T. Honda, and S. Fukuzumi, "Protonated iron–phthalocyanine complex used for cathode material of a hydrogen peroxide fuel cell operated under acidic conditions," *Energy Environ. Sci.*, vol. 4, no. 8, pp. 2822–2825, 2011.

[101] G. Selvarani, S. K. Prashant, A. K. Sahu, P. Sridhar, S. Pitchumani, and A. K. Shukla, "A direct borohydride fuel cell employing Prussian Blue as mediated electron-transfer hydrogen peroxide reduction catalyst," *J. Power Sources*, vol. 178, no. 1, pp. 86–91, 2008.

[102] F. Ricci *et al.*, "Prussian Blue and enzyme bulk-modified screen-printed electrodes for hydrogen peroxide and glucose determination with improved storage and operational stability," *Anal. Chim. Acta*, vol. 485, no. 1, pp. 111–120, 2003.

[103] K.-H. Kim *et al.*, "Effect of Nafion® gradient in dual catalyst layer on proton exchange membrane fuel cell performance," *Int. J. Hydrogen Energy*, vol. 33, no. 11, pp. 2783–2789, 2008.

[104] C. A. Schneider, W. S. Rasband, and K. W. Eliceiri, "NIH Image to ImageJ: 25 years of image analysis," *Nat. Methods*, vol. 9, no. 7, pp. 671–675, 2012.

[105] A. F. Stalder, T. Melchior, M. Müller, D. Sage, T. Blu, and M. Unser, "Low-bond axisymmetric drop shape analysis for surface tension and contact angle measurements of sessile drops," *Colloids Surfaces A Physicochem. Eng. Asp.*, vol. 364, no. 1–3, pp. 72–81, 2010.

[106] P. Rewatkar and S. Goel, "based membraneless co-laminar microfluidic glucose biofuel cell with MWCNT-fed bucky paper bioelectrodes," *IEEE Trans. Nanobioscience*, vol. 17, no. 4, pp. 374–379, 2018.

[107] S. M. M. Ehteshami, M. Asadnia, S. N. Tan, and S. H. Chan, "based membraneless hydrogen peroxide fuel cell prepared by micro-fabrication," *J. Power Sources*, vol. 301, pp. 392–395, 2016.

[108] S. K. Sia and G. M. Whitesides, "Microfluidic devices fabricated in poly (dimethylsiloxane) for biological studies," *Electrophoresis*, vol. 24, no. 21, pp. 3563–3576, 2003.

APPENDIX A: CAD DRAWINGS

A.1 MFC
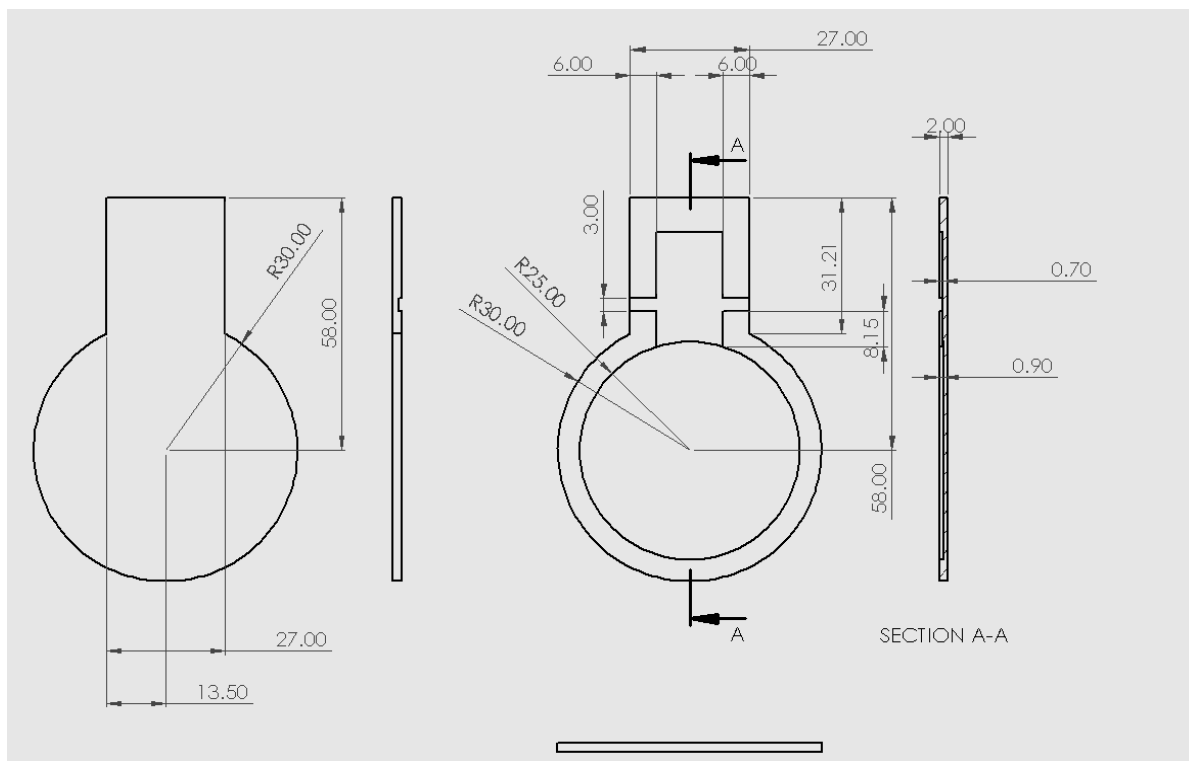
Figure A- 1: PVDF-based MFC: main body drawing (Scale: 1:1, unit: mm).
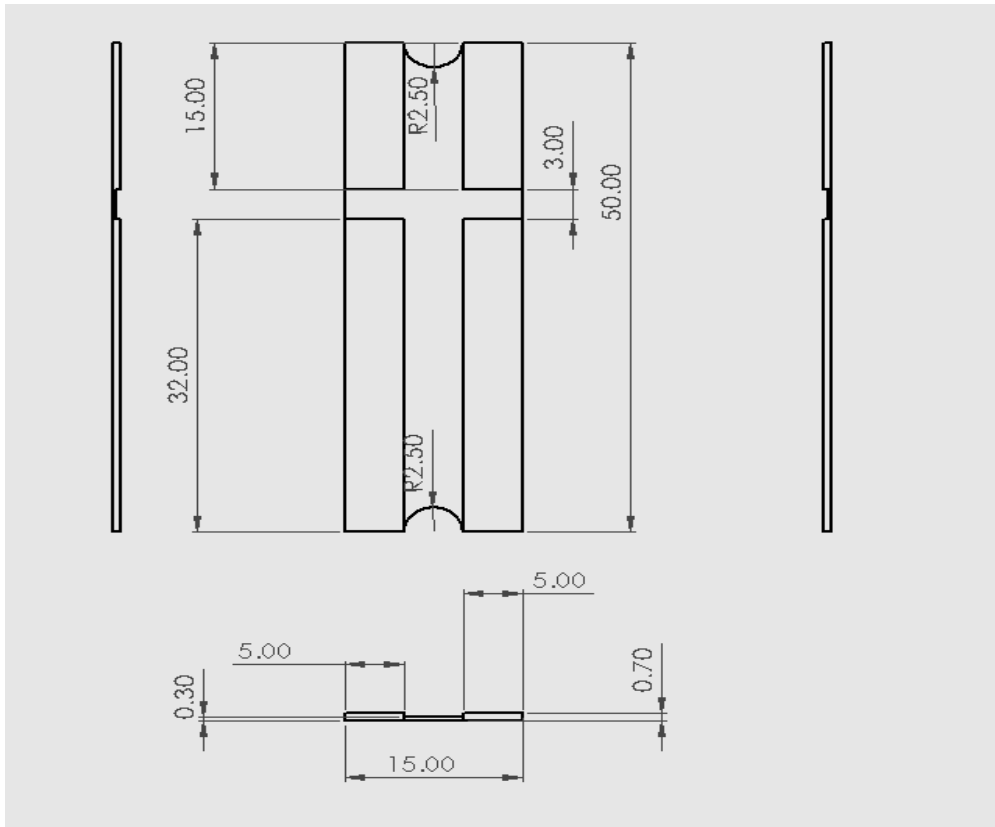
Figure A- 2: PVDF-based MFC: channel holder drawing (Scale: 1:1, unit: mm).

A.2   Rotating Drum
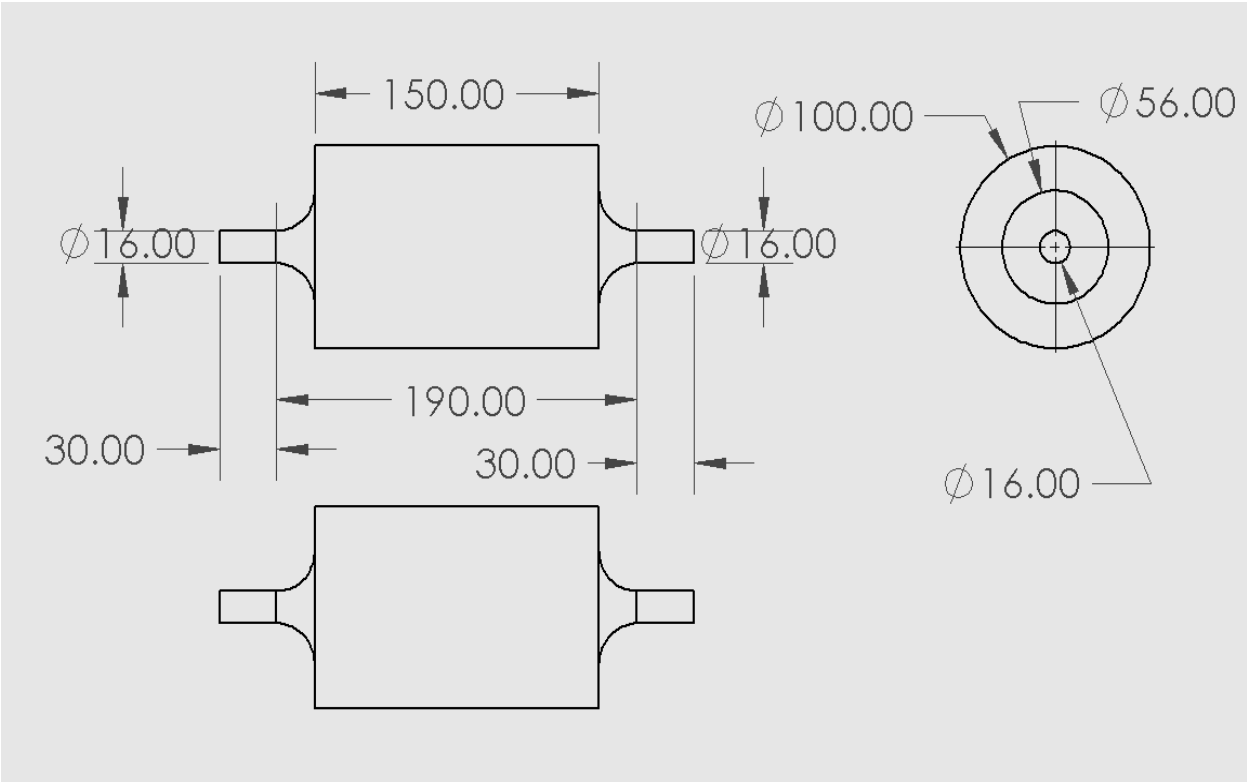
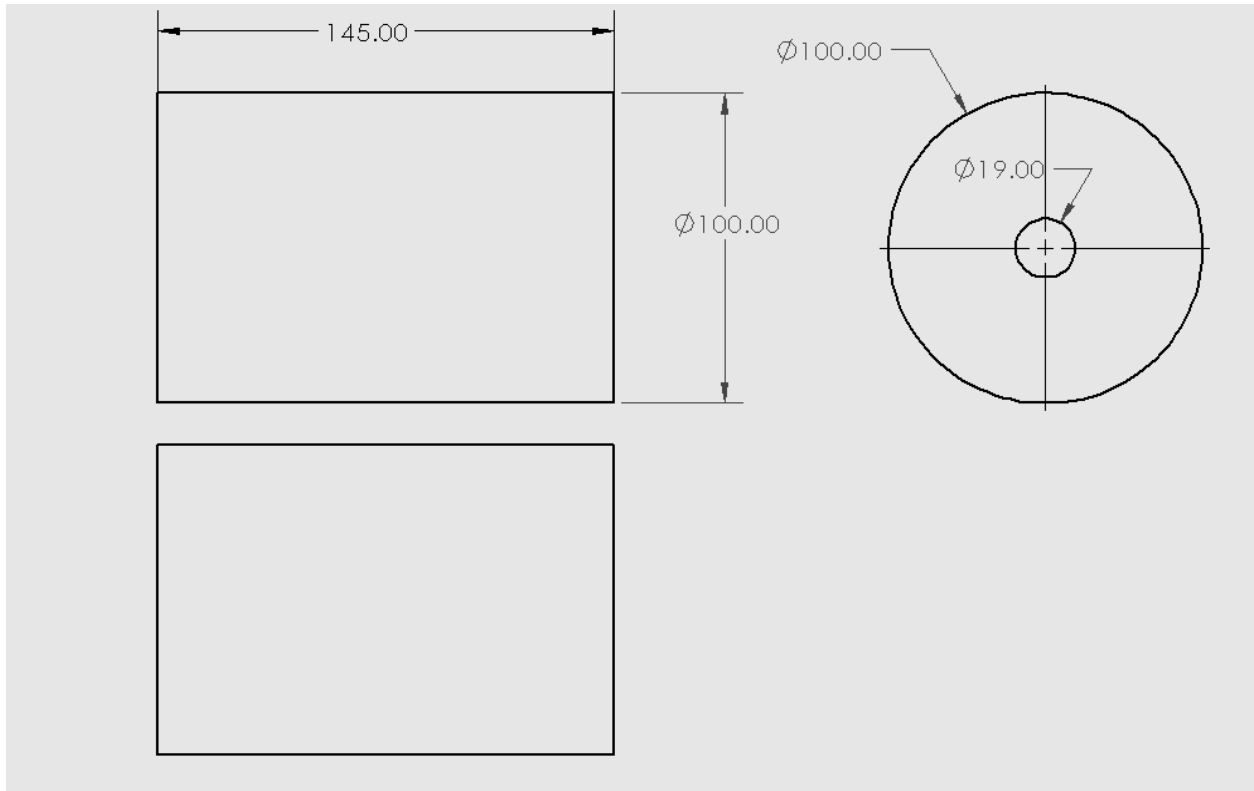*Figure A- 3: Drawing of drum and shaft as one piece (Scale: 1:1, unit: mm).*

Figure A- 4:Drawing of drum to mount on an aluminum shaft (Scale: 1:1, unit: mm).
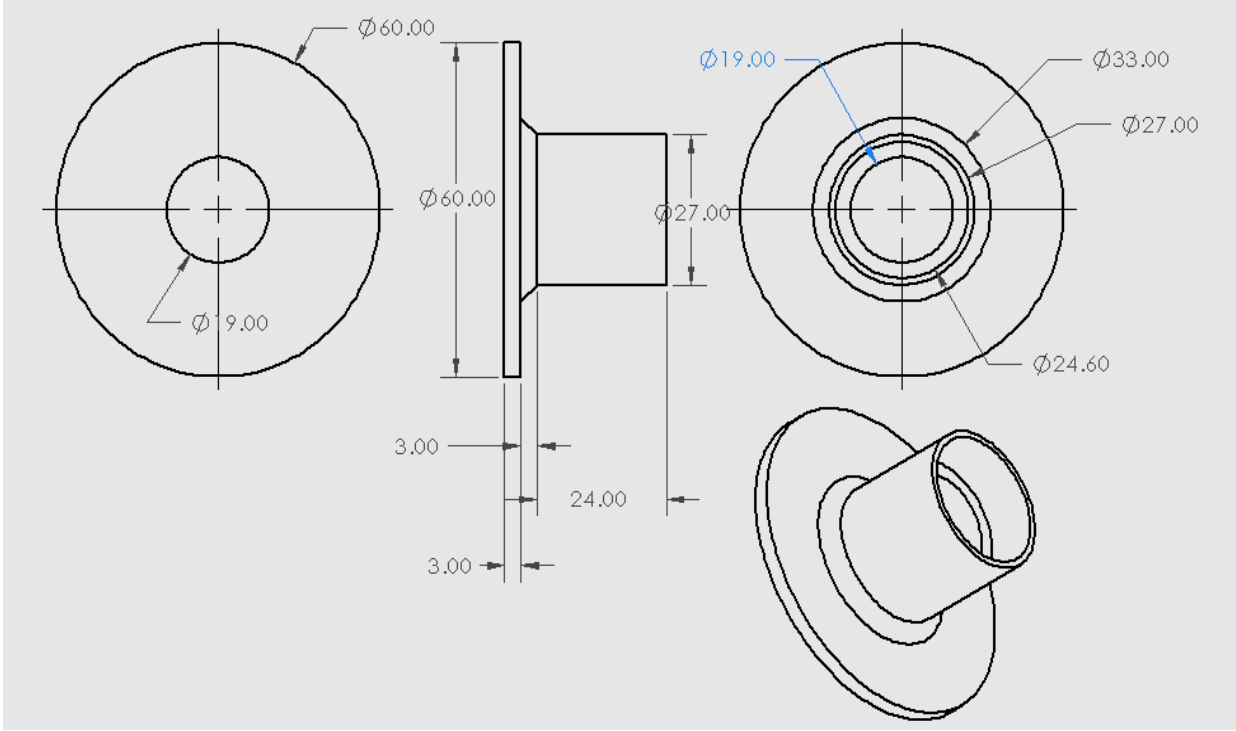
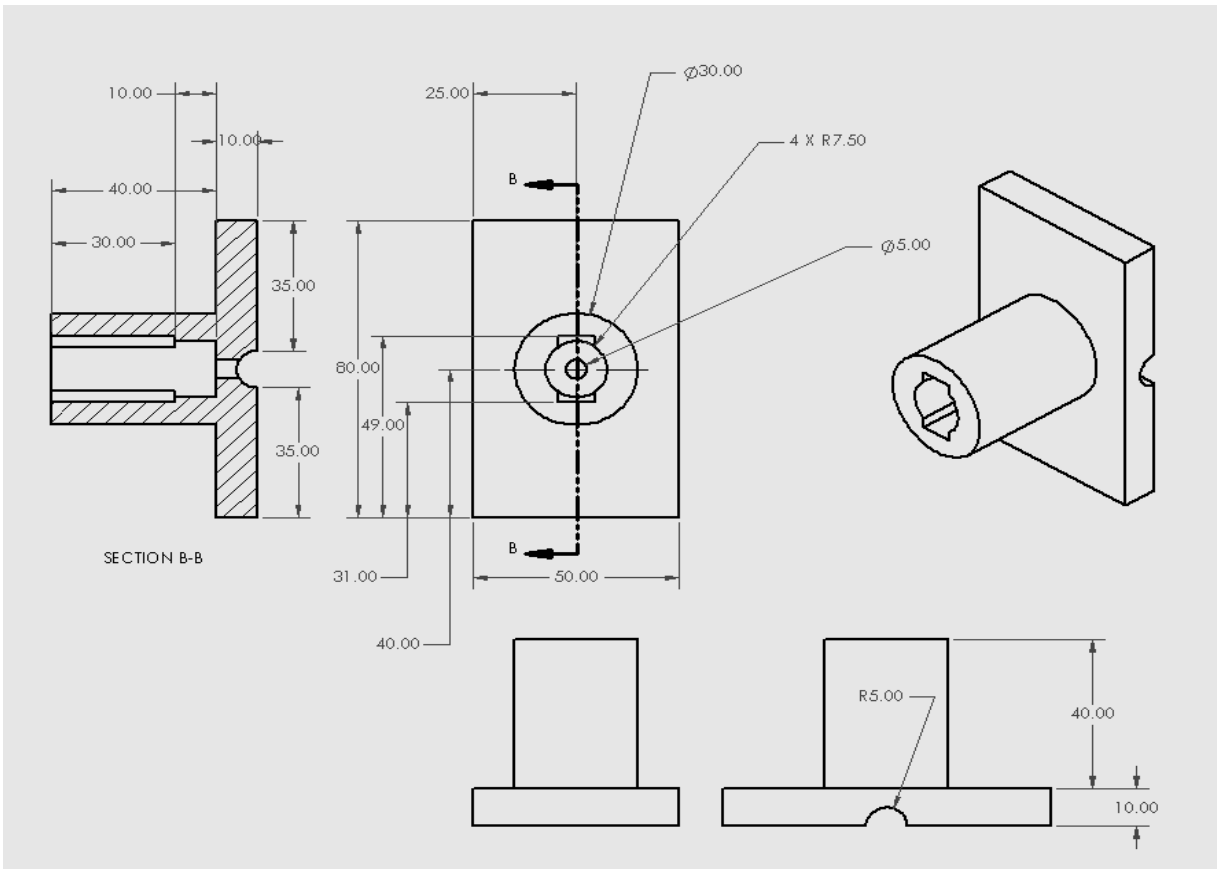*Figure A- 5:Drawing of the shaft holder (Scale: 1:1, unit: mm).*

Figure A- 6: Drawing of the brush holder (Scale: 1:1, unit: mm).

APPENDIX B: MFC MICROFABRICATION METHOD

The structure of the system is considered as six layers, as shown in Figure B.1, during fabrication.
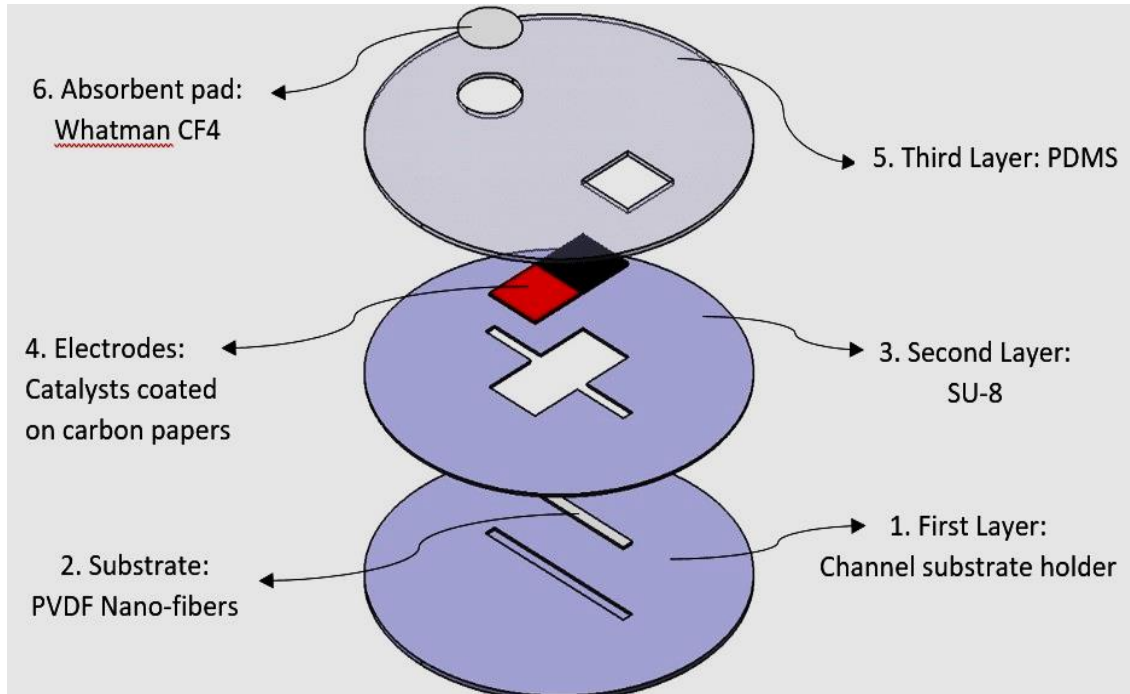
Figure B- 1: From bottom to top: 1. first layer to define microchannel holder, 2. PVDF nanofibers, 3. second layer to define electrode holders, 4. electrodes, 5. third layer to define absorbent and reservoir areas, and 6. absorbent pad.

The fabrication methods in this section are derived from "EE 817 - Microfabrication by X-Ray Lithography" course material offered by Dr. Sven Achenbach at University of Saskatchewan in Fall 2018. In case other sources are used, they are cited within the text.

B.1 First Mask: The Channel Holder

Schematic of the first mask before patterning is demonstrated in Figure B.2.

Photomask fabrication steps are discussed as follows:

Step 1. Patterning by Laser UV-writer

The channel pattern is provided by CAD (see Figure B.3). Two alignment holes are also included to the pattern for a precise and accurate alignment. In the pattern, there are a few densely written areas. To make the process faster, the Vector Scan strategy is selected for the writer.
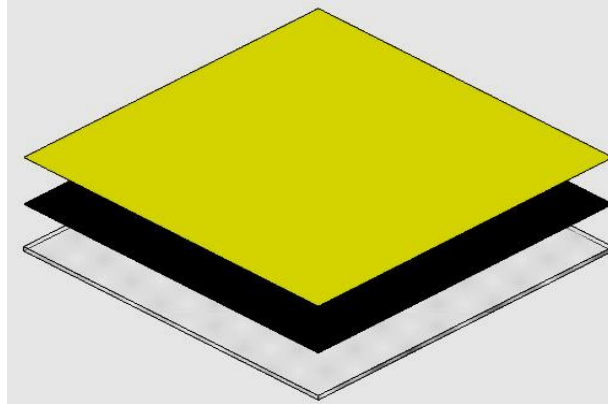
Step 2. Post Exposure Bake (PEB)

Figure B- 2: Schematic of the pre-made first mask before patterning; substrate (transparent layer): Borosilicate Glass, absorber layer (black layer): Chromium, photo resist coating (yellow layer).
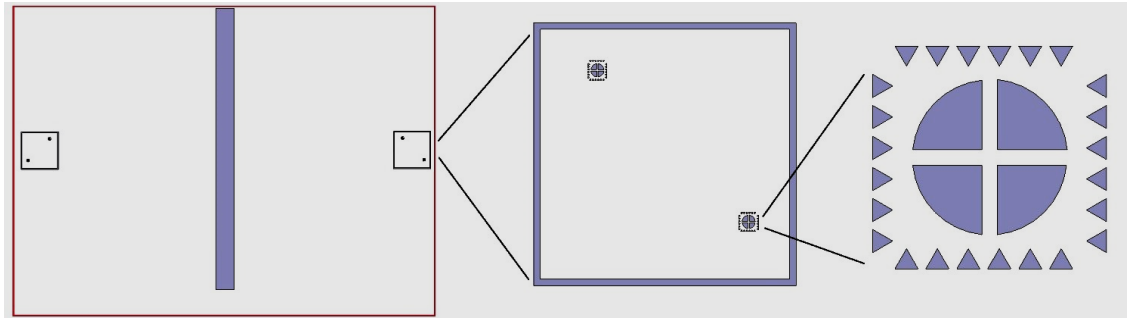

Figure B- 3: Laser UV-writer pattern provided by CAD. The alignment holes are added for further alignments of the masks and layers.

Polymerization of the exposed area is activated by post-bake. In order to avoid stress and cracking, two step contact process with hot plate will be done. Also, rapid cooling of the resist will be avoided. After PEB, the pattern appears on the resist (see Figure B.4)

Step 3. Resist Development

After post-baking, the mask is immersed in the appropriate developer and then the unexposed areas are washed away by rinsing in isopropyl alcohol. Only the area covering the Cr surface is the polymerized resist (See Figure B.5).

Step 4. Inspection and Plasma De-scum

Before taking any further steps, a careful inspection is performed to check for any faults such as: lifted resist, over or under development, contamination and any other damages that can affect

the pattern quality. If everything is acceptable, a light oxygen plasma de-scum etch can be done to clean out any remaining resist on the Cr surface.
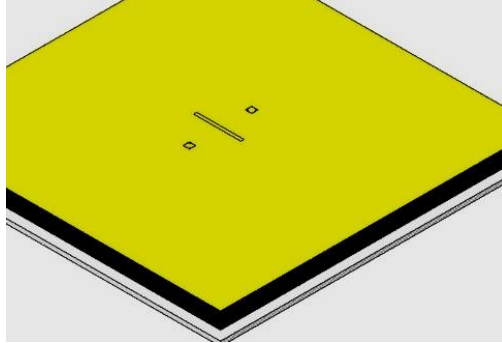
Step 5. Wet Chemical Etch of Cr

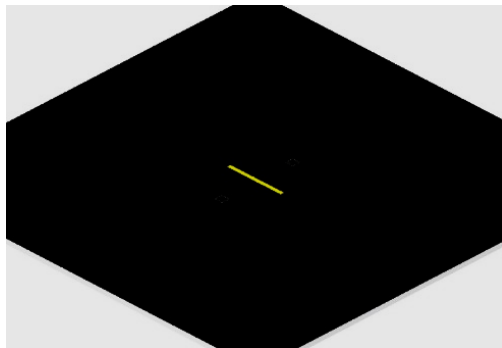*Figure B- 4: Pattern appearance after PEB.*

Figure B- 5: Mask after resist development; the only areas covering the Cr surface are the polymerized resist.

The Cr surface area that is not covered by the developed resist can be etched by Ceric ammonium nitrate-based etchant with the rate of 40 ˚A/sec at room temperature (source: sigmaaldrich.com). The etchant does not affect the resist. Therefore, after etching, the area covered by resist is retained. The mask after wet chemical etching is demonstrated in Figure B.6.

Step 6. Resist Stripping

In order to avoid polymer-polymer contact and high friction during alignment of the mask with the work piece, resist is supposed to be removed. It is done by resist remover PG (Manufactured by MircoChem). It swells and lifts off the cross-linked resist. The resist stripping consists of four steps: first bath to remove the bulky parts of the resist, second bath removes any material remaining on the Cr surface, third bath by Isopropyl alcohol and the last step is rinsing with dilute water and drying. The mask after resist stripping is shown in

Figure B.7

Step 7. Final Inspection

In this step a careful inspection by microscope is done to check for any fault or damage to the pattern quality, Cr absorbers and sidewalls. It is needless to mention that after fabrication; the mask should be preserved in a mask holder to avoid any scratch or contamination.
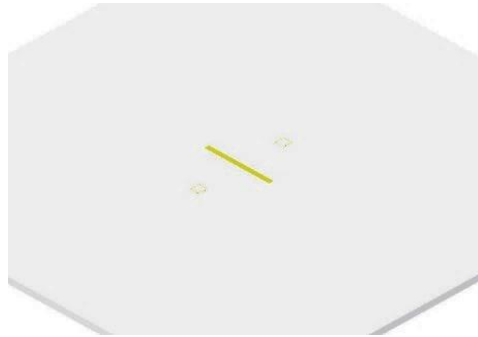
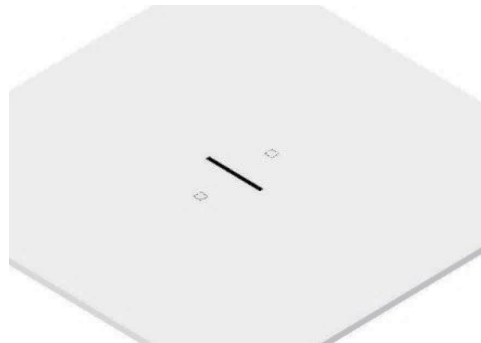*Figure B- 6: Mask after wet chemical etch of Cr surface.*

Figure B- 7: Mask after resist stripping.

B.2 Second Mask: The Electrodes Holder

The fabrication process of the second mask is the same as the First mask. The schematic of the second mask after fabrication is shown in Figure B.8.
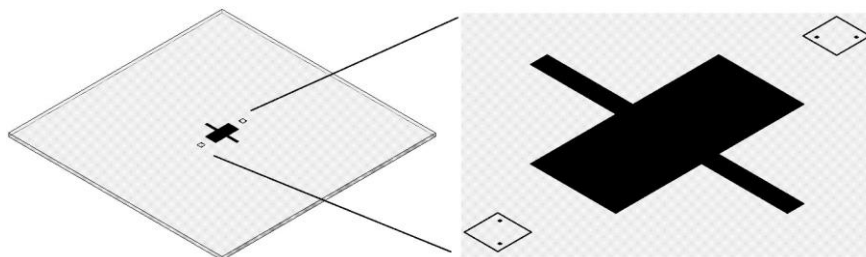
Figure B- 8: The second mask after fabrication.

B.3   Device Fabrication

Fabrication of the device is consisted of six steps:

Fabrication of the channel by the first mask

Fabrication of electrodes holder by the second mask

Fabrication of the third layer by PDMS master mold made by SUEX

Fabrication of the channel substrate

Fabrication of the electrodes

Assembly of the layers

B.4   Fabrication of the Channel by the First Mask

Substrate: Silicon Wafer (Diameter: 100mm, Thickness: 500μm)

Resist: SUEX (Thickness: about 107μm rather than required 100μm because during PEB, about 7.5% of the resist will shrink)

SUEX is considered as the negative tone resist to fabricate the first layer. Maximum sensitivity of SUEX is at $λ= 350...400$nm. Therefore, UV lithography is chosen as the fabrication method.

Resist and substrate adhesion improvement: HMDS

Exposure source: Mercury vapor lamp with $λ=365$nm (i-line)

Exposure approach: Preferably Imaging Projection. In case of limited facility and budget, proximity printing can be selected as well (resolution limitation to 2μm-4μm because of Fresnel Diffraction is acceptable) *Fabrication Steps:*
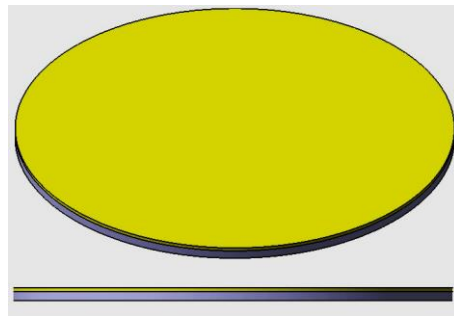
The SUEX laminated substrate is shown in Figure B.9.

Figure B- 9: The SUEX laminated substrate.

Step 1. Pre-bake

Using hot plate: 5 minutes on 65°C and 10 to 20 minutes on 95°C.

Step 2. Exposure

Required exposure energy: 215-240 mJ/cm^2. SUEX is very sensitive (high absorbance) to wavelengths below 350nm leading it to over exposure on top area of the resist and obtaining T-topping after development. To have the best result, a photolithography mask aligner filter (PL360-LP manufactured by OMEGA Optical) can be used to cut off the excessive energy of spectrum (wavelength below λ=365nm). However, this filter increases the exposure time for 40% (see Figure B.10)
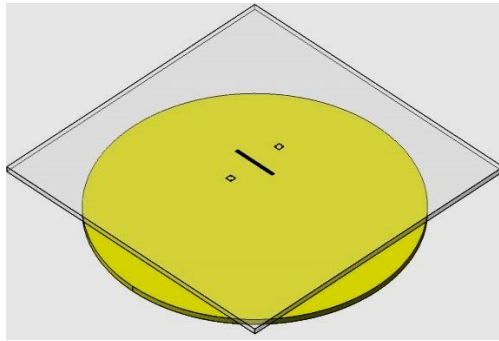

Figure B- 10: Photolithography exposure of first layer using the first mask.

Step 3. PEB

To start the cross-linking process leading to polymerization of the exposed areas. In order to reduce the stress (because of shrinking of SUEX during crosslinking) two-step PEB is recommended and sudden cooling down is avoided. 2-5minutes on 65°C hotplate and 8-10 minutes on 95°C hotplate.

After the PEB step, instead of taking the usual fabrication steps (development of the resist, rinsing and drying), in order to fabricate the second layer on this layer, without development of the resist, the second layer (electrodes holder) can be fabricated on this layer (see Figure B.11).
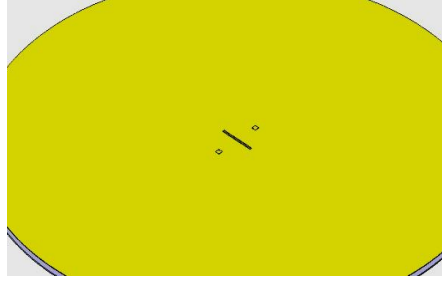
Figure B- 11: Pattern appearance after PEB.

B.5 Fabrication of the Electrode Holders by the Second Mask

The exposure source, exposure approach is the same as the first layer fabrication. SU-8 resist will be used as resist. The resist thickness is about 210μm rather than the required 190μm because during PEB, about 7.5% of the resist will shrink.

Fabrication Steps:

Step 1. Inspection of the surface

If the surface is too rough to spin coat the new SU-8, a surface treatment can be done to achieve a smooth surface.

Step 2. Spin coating of the SU-8 2075

The same process as first layer. The only difference is the second spin speed: 1250rpm

(rather than 2100rpm because of thicker layer requirement)

Step 3. Pre-bake

Using hot plate: 7 minutes on 65°C and 30 to 45 minutes on 95°C.

Step 4. Exposure

The condition of exposure is the same as first layer exposure step. Required exposure energy: 260-350 mJ/cm^2 (rather than 215-240 mJ/cm^2 because of thicker layer). See Figure B.12.
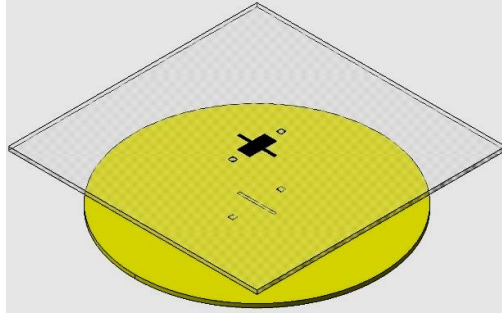
Figure B- 12: Second exposure on the first layer by the second mask.

Step 5. PEB

For 5minutes on 65°C hotplate and 12-15 minutes on 95°C hotplate.

Step 6. Development

Immersion into the SU-8 developer for 15-17 minutes.

Step 7. Rinse and Dry

Rinsing with fresh developer and then isopropyl alcohol. If white film is produced during washing with the alcohol (indication of underdevelopment), repeating the development step is required. The schematic of the system is shown Figure B.13.
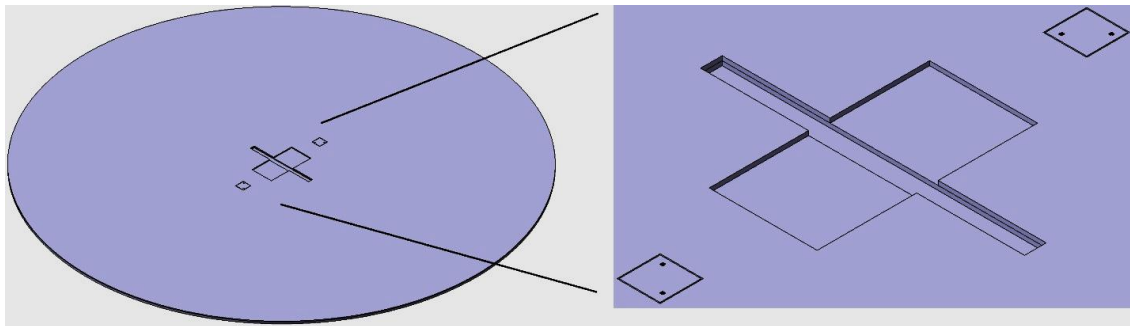

Figure B- 13: Schematic of the system after development and rinsing of the resist.

B.6 Fabrication of the Third Layer by PDMS Master Mold Made by SUEX

The last layer is made of PDMS and its thickness is 482μm. The schematic of the desired layer is shown in Figure B.14.
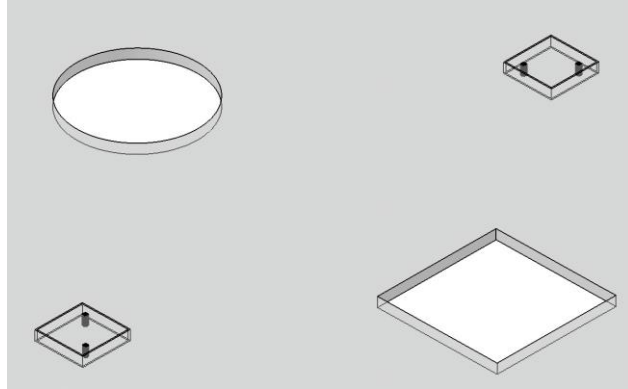
Figure B- 14: Schematic of the third layer.

For fabrication of this layer, several alternatives can be considered: Cr Photomask, Electron Beam Writer/Laser UV writer, Laser Micromachining, and PDMS master molding [108]

Since the dimensions of the circular and square shapes in the schematic is not in micron scale (5mm), and also achieving a very high quality and accurate pattern transfer (better than 8μm [108]) is not necessary, in order to reduce the time and cost of the fabrication, the first three approaches (Photomask, Electron Beam Writer/laser UV writer and Laser Micromachining) approaches are not considered. Therefore, the molding approach can be used to fabricate this layer. The pattern is designed by the CAD and can be printed by photo plotter with the quality of 20 000 dots per inch (resolution about 8μm). This transparency can be used as a photomask in UV lithography by SUEX as resist in order to make the master mold for PDMS.

Step 1. Using SUEX laminated resist (500μm)

Step 2. Alignment and UV exposure of the transparency made by photo plotter.

Step 3. Resist development

Step 4. Treatment of the mold surface to prevent bonding SUEX to PDMS during the molding procedure.

Step 5. Preparing the PDMS pre-polymer mixture and pouring into the mold (1000μm).

Step 6. Curing PDMS at 70°C for 1 hour and peeling it off from the mold.

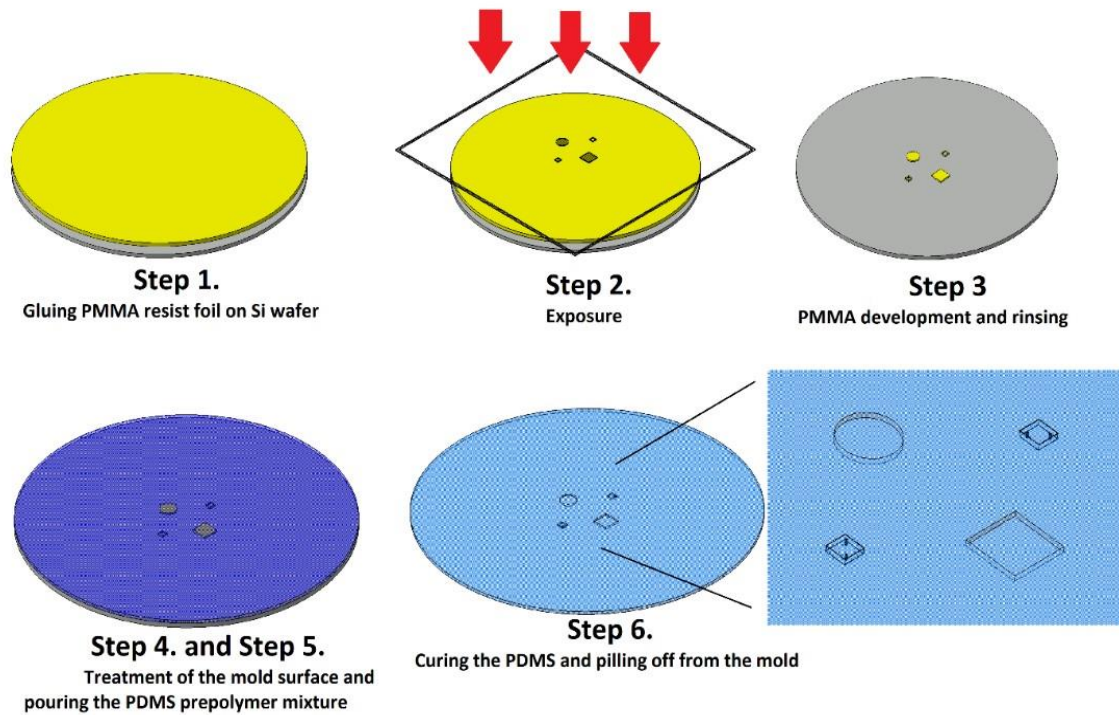The summary of the method is shown in Figure B.15.

Figure B- 15: PDMS layer fabrication steps using the molding method.

B.7 Fabrication of the Channel Substrate

The fabrication method is derived by the literature [16];

Step 1. Preparation of PVDF solution

Dissolving of PVDF powder in a mixture of Dimethylformamide (DMF) and Acetone and then heating the solution to achieve a homogenous solution

Step 2. Electrospinning

Transfer of 10 mL of solution into a syringe. 12 kV of Direct Current is applied to the syringe needle positioned 15 cm away from a rotating spindle covered by Aluminum foil. The PVDF nanofibers are deposited on the spindle.

Step 3. Surface Treatment of the fibers

The fibers have a super hydrophobic behavior (contact angle of 162°). In order to make the surface hydrophilic to be used as channel substrate, an oxygen plasma treatment will used to make the surface super hydrophilic (contact angle 10°).

Step 4. Cutting the fibers

For cutting the fibers as per the desired dimensions (1mm × 15mm), a laser micromachining – ablation machine can be used to mechanically cut the fibers.

Step 5. Investigation and installment

After careful investigation of the fibers by a microscope, fibers can be installed on the channel. For fixing the fibers onto the channel, a compatible glue (as bonding between fibers to SU-8) can be used. The device after PVDF fibers installment is shown in Figure B.16.
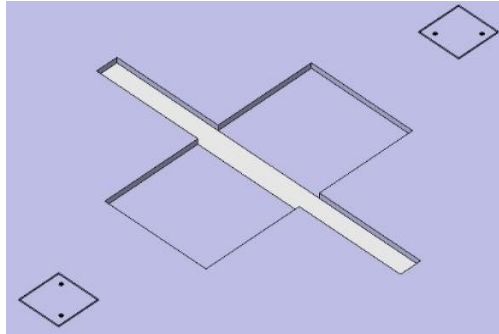
Figure B- 16: PVDF fibers installment on the channel.

B.8   Fabrication of the Electrodes

The carbon papers can be cut by CO2 laser cutter [97]. After applying the desired catalysts (by spraying, printing or other methods related to the type of catalysts), the electrodes can be installed on their respective locations by gluing. The devices after electrodes installment is shown in Figure B.17.
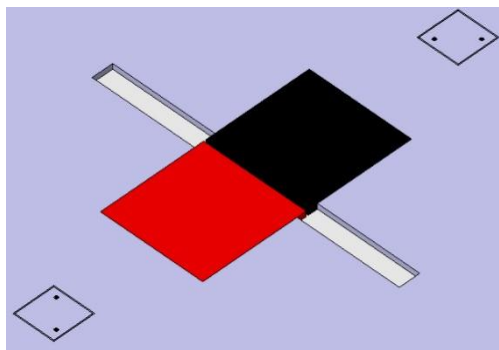
Figure B- 17: Electrodes installment on the layer.

B.9   Assembly of the Layers

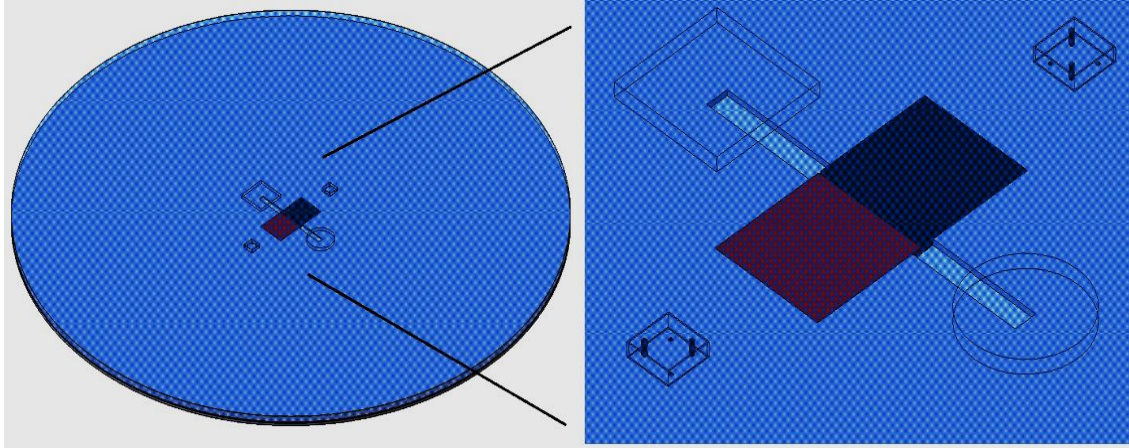The schematic of the system after alignment of the PDMS layer on the device is shown in Figure B.18.

Figure B- 18: Final schematic of the MFC system.

APPENDIX C: IMAGE PROCESSING USING IMAGEJ SOFTWARE
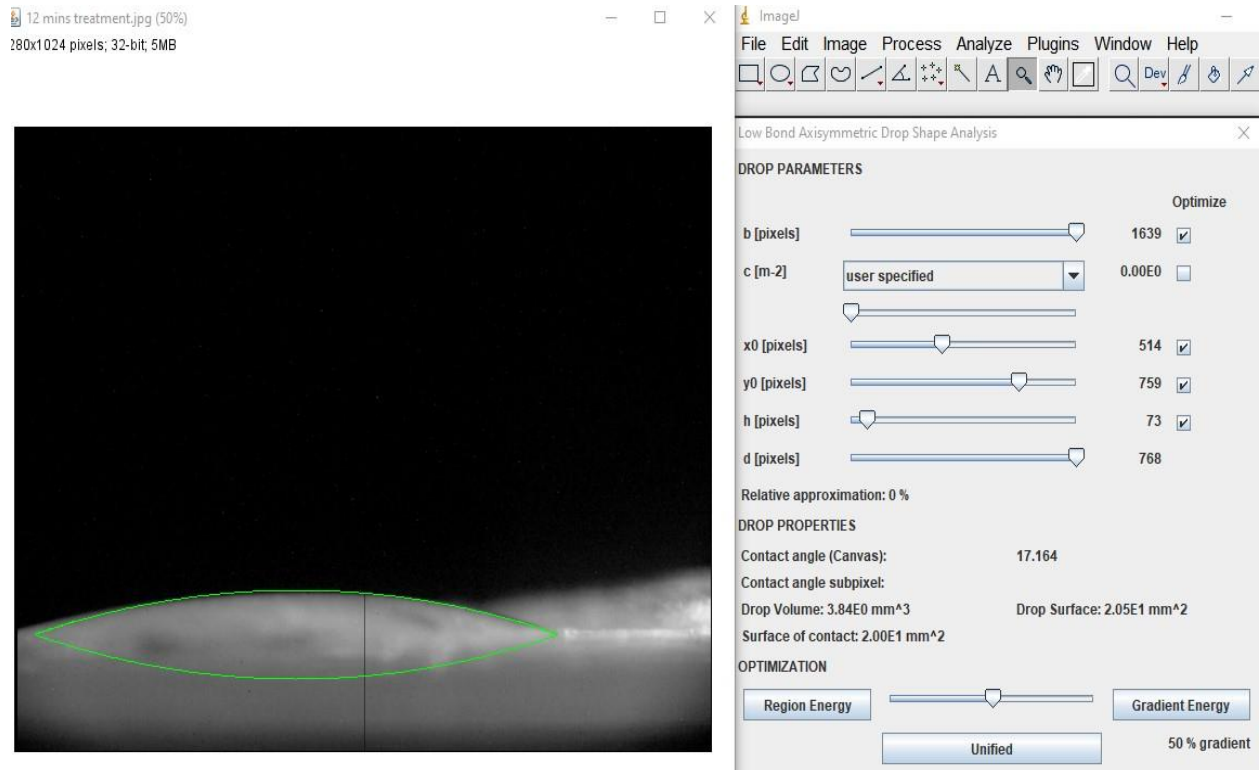
C.1   Contact Angle Approximation

Figure C- 1: Contact angle approximation after 12 minutes of plasma treatment.
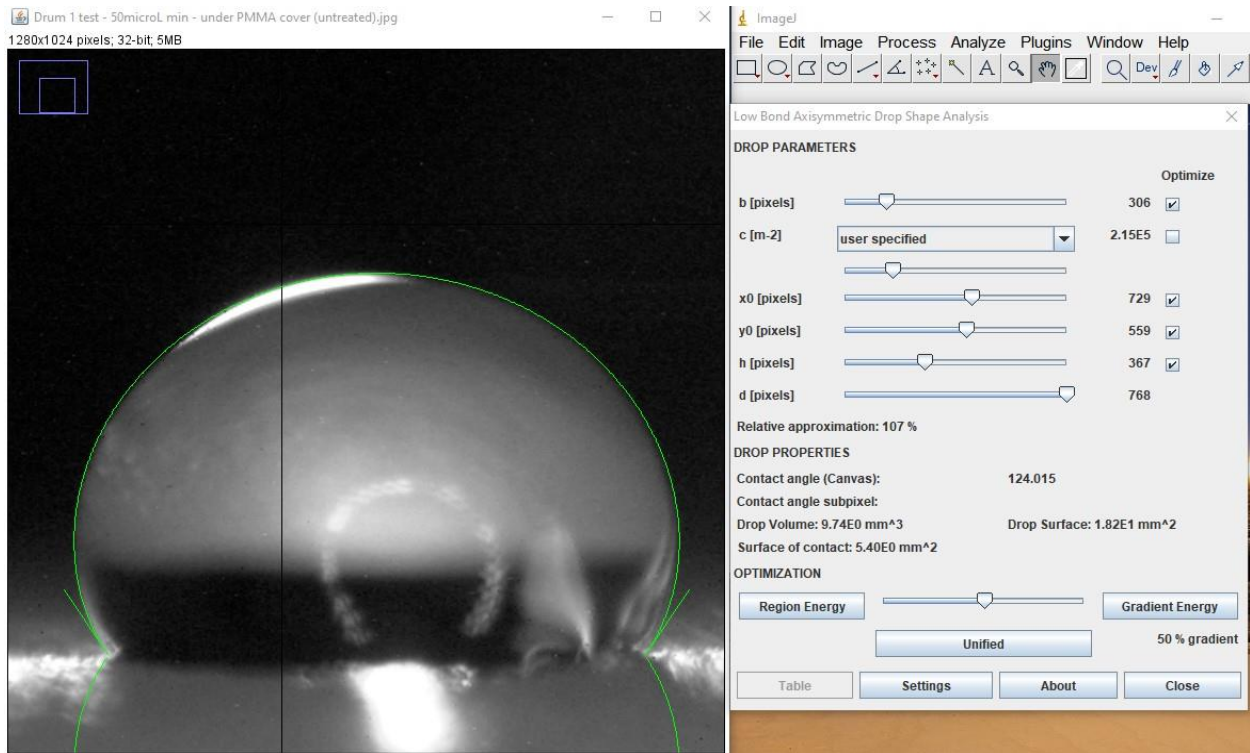
Figure C- 2: Contact angle approximation for underneath of the PMMA cover after.
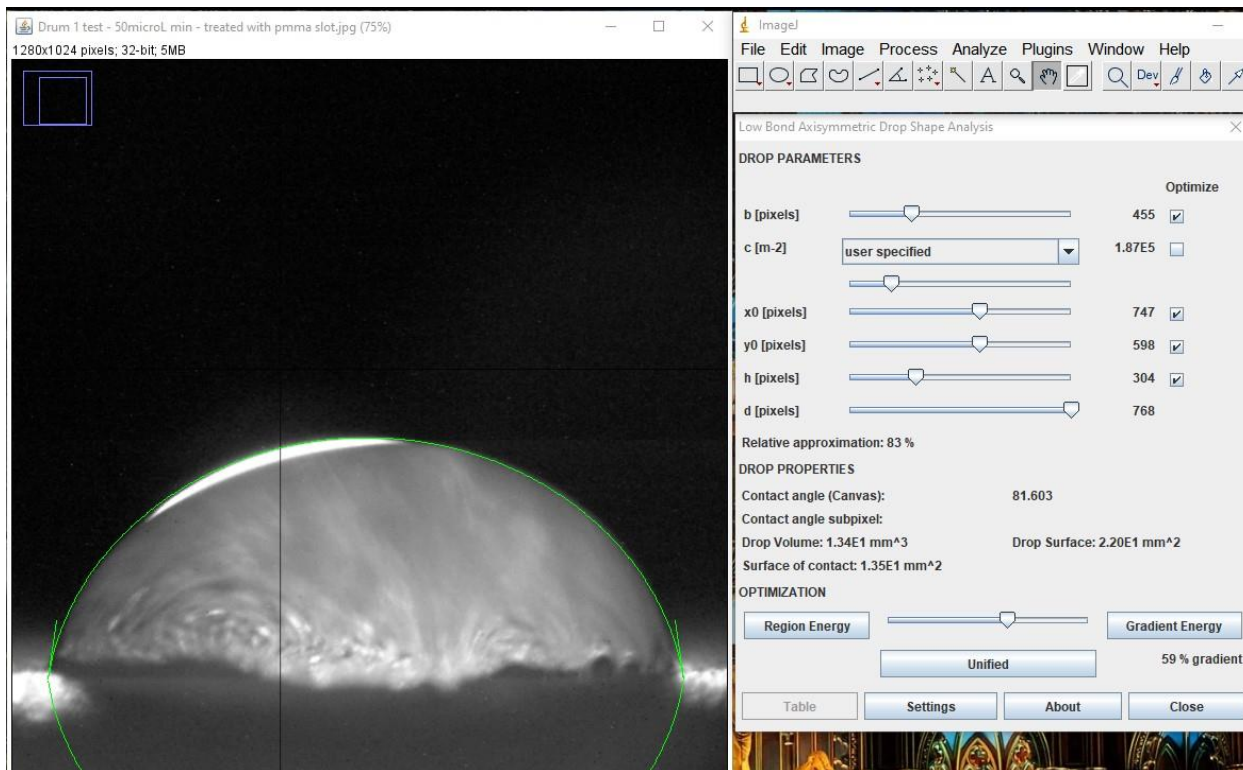
Figure C- 3: Contact angle approximation for the exposed area of the PMMA cover after 15 minutes of plasma treatment.

APPENDIX D: EQUATIONS AND CALCULATIONS

$$\frac{30}{100} \times \frac{1.110\ g}{1\ cm^3} \times \frac{1\ cm^3}{1\ mL} \times \frac{1\ mol}{34.014\ g} \times \frac{1000\ mL}{1\ L} = 9.79\ M\left(\frac{mol}{L}\right) \qquad (D-1)$$

$$C_{1\frac{mol}{L}} \times V_{1\,mL} = C_{2\frac{mol}{L}} \times V_{2\,mL} \rightarrow 9.79_{\frac{mol}{L}} \times V_{1\,mL} = 0.5_{\frac{mol}{L}} \times 10_{mL} \xrightarrow{yields} V = 0.51\ mL\,(D-2)$$

$$0.5\frac{mol}{L} = \frac{1\ mol}{329.26\ g} \times \frac{1000\ mL}{1\ L} \times \frac{X\ gr}{20\ mL} \rightarrow X = 3.29gr \qquad (D-3)$$

$$0.5\frac{mol}{L} = \frac{1\ mol}{162.2\ g} \times \frac{1000\ mL}{1\ L} \times \frac{X\ gr}{20\ mL} \rightarrow X = 1.62\ gr\ FeCl_3 \qquad (D-4)$$

$$Current\ Density\left(\frac{A}{cm^2}\right) = \frac{I(A)}{Area\ of\ Electrode(cm^2)} \qquad (D-5)$$

$$P_{(W)} = I_{(A)}V_{(V)} \rightarrow Power\ Density\left(\frac{W}{cm^2}\right) = Current\ Density\left(\frac{A}{cm^2}\right) \times V_{(V)} \qquad (D-6)$$

APPENDIX E: PERMISSION TO REPRODUCE CONTENT LICENSES

SPRINGER NATURE LICENSE

TERMS AND CONDITIONS

Oct 30, 2020

This Agreement between University of Saskatchewan -- Farzad Dehghan ("You") and Springer Nature ("Springer Nature") consists of your license details and the terms and conditions provided by Springer Nature and Copyright Clearance Center.

License Number	4938601239553
License date	Oct 30, 2020
Licensed Content Publisher	Springer Nature
Licensed Content Publication	Springer eBook
Licensed Content Title	Fundamentals
Licensed Content Author	Gerhard Pahl, Wolfgang Beitz
Licensed Content Date	Jan 1, 1996
Type of Use	Thesis/Dissertation
Requestor type	academic/university or research institute
Format	print and electronic
Portion	figures/tables/illustrations
Number of figures/tables/illustrations	2
Will you be translating?	no
Circulation/distribution	1 - 29
Author of this Springer Nature content	no
Title	PVDF as a biocompatible substrate for microfluidic fuel cells
Institution name	University of Saskatchewan
Expected presentation date	Oct 2020
Portions	Figure 2.3. and Figure 2.8.
Requestor Location	57 Campus Drive University of Saskatchewan Saskatoon, SK S7N 5A9 Canada Attn: University of Saskatchewan
Total	**0.00 CAD**

Design theory and methodology for enterprise systems

Taylor & Francis
Taylor & Francis Group

Author: W.J. Zhang, , J.W. Wang
Publication: Enterprise Information Systems
Publisher: Taylor & Francis
Date: Mar 23, 2016

Rights managed by Taylor & Francis

Thesis/Dissertation Reuse Request

Taylor & Francis is pleased to offer reuses of its content for a thesis or dissertation free of charge contingent on resubmission of permission request if work is published.

BACK   CLOSE